Quark and Gluon Propagation in Two-Colour Quantum Chromodynamics at Finite Density

Tamer S. Boz
M.Sc.

Thesis presented for the degree of

Doctor of Philosophy

to the

National University of Ireland Maynooth
Department of Theoretical Physics

July 2018

Head of Department

Dr. Jon-Ivar Skullerud

Research Advisor

Dr. Jon-Ivar Skullerud

Contents

Abstract

Two-colour quantum chromodynamics has been studied on the lattice at finite chemical potential. The phase diagram of the theory with respect to varying temperatures and densities is presented. Deconfinement and normal to superfluid phase transitions are investigated. Chromoelectric and chromomagnetic components of the gluon propagator have been calculated and their response to varying temperatures and chemical potentials are studied. The form factors of the normal and anomalous quark propagator are presented and their behaviour with respect to changing chemical potential is discussed in the light of corresponding physical expectations.

Acknowledgments

I dedicate this work to my mother Şükran Boz and to my father Mehmet Boz, who moved our home from İzmir to Ankara just to provide me better conditions during my physics education 17 years ago. I would like to express my sincere gratitude to them for all their support for my education.

Bu çalışmayı, 17 yıl önce, sırf fizik öğrenimim boyunca bana daha iyi koşullar sağlamak için evimizi İzmir'den Ankara'ya taşıyan annem Şükran Boz ve babam Mehmet Boz'a ithaf ediyorum. Öğrenim hayatım boyunca bana verdikleri tüm destek için onlara en içten teşekkürlerimi sunarım.

I would also like to thank to my supervisor Dr. Jon-Ivar Skullerud for all his support during my Ph.D. study.

Chapter 1

Introduction

1.1 Quantum Chromodynamics (QCD)

Atoms are building blocks of the matter we see in everyday life. They have nuclei which are in turn composed of protons and neutrons that are collectively called *nucleons*.

In the early 20th century it was believed that the nucleons were fundamental particles. In the 1960's, it was understood, both through theoretical studies and experiments (called *deep-inelastic scattering* [1]) that the nuclei were themselves made up of particles called *quarks*. They interact through one of the four fundamental forces in the nature that is called *strong force*. The theory that describes the strong force and the particles affected by the strong force is called Quantum Chromodynamics (QCD), the term to be justified below.

While it is possible to isolate a proton or a neutron from the nucleus of an atom, it is not possible to isolate a quark; they are trapped inside the nucleons, but they can move freely inside them. This phenomenon is called *confinement* of quarks, to be discussed in more detail in the following chapters.

At extremely high densities, the matter becomes so densely packaged that it becomes impossible to distinguish which quark belongs to which nucleon. This means that the quarks can freely move inside the whole object. This gives rise to *quark matter*, whose degrees of freedom are quarks, rather than nucleons [2].

Such high densities exist in the cores of compact stars. These are the most dense objects in the Universe after black holes, which form as a result of the gravitational collapse of their cores onto themselves. As they are rich in neutrons, they are sometimes also referred to as the neutron stars. Their density is a few times higher than that of nuclear matter [3]. We therefore expect the extreme-dense theoretical phenomena, some of which will be mentioned in the following, to occur inside them [4].

Temperature is another external parameter whose increase may lead to a new state of matter in which the degrees of freedom are not nucleons but rather quarks and gluons. This new state is the quark-gluon plasma and it emerges as a result of *deconfinement*. It has been probed in extremely high energetic heavy-ion collision experiments at RHIC or LHC [5].

Before focusing on such densities, let us first briefly review QCD and Lattice QCD at zero density.

In the zero-density vacuum, and if there is no interaction among the fermions in the system, the fermionic part of the Lagrangian density that governs the theory is:

$$\mathcal{L} = \sum_{i=1}^{N_f} \left[m_i \bar{\psi}_i (x) \psi_i (x) + \bar{\psi}_i (x) (\gamma^\mu \partial_\mu) \psi_i (x) \right], \tag{1.1}$$

which is a sum over all *quark flavours* in the system. There are six quark flavours in the nature. The interaction among quarks is implemented by minimal coupling as in Quantum Electrodynamics (QED):

$$\mathcal{L} = \sum_{i=1}^{N_f} \left[m_i \bar{\psi}_i (x) \psi_i (x) + \bar{\psi}_i (x) \gamma^\mu (\partial_\mu - A_\mu (x)) \psi_i (x) \right] + \frac{1}{4g^2} \mathrm{tr} \left[F_{\mu\nu} F^{\mu\nu} \right], \tag{1.2}$$

where A_μ denotes the gauge field, whose quanta are the *gluons* and $F_{\mu\nu}$ is the gluon field strength tensor analogous to the one in QED.

As it stands, this Lagrangian density looks like a generalization of the fermionic part of the Lagrangian of QED to N_f fermions. But there is a fundamental difference. In QED, the gauge field A_μ commutes with itself, whereas it does not in QCD. They are matrix-valued objects and are elements of the $su(3)$ algebra. This gives rise to interactions between not only fermions but also gluons, making the theory much more involved. They all interact through the QCD analogue of the electric charge, the *colour charge* (hence is the term chromodynamics). There are three types of colours in nature.

Just as electrons interact via exchange of virtual photons in QED, quarks interact via exchange of gluons in QCD. This necessitates eight different gluon types carrying interaction between quarks and antiquarks as well as among themselves. All colour-charged objects are *confined* inside composite particles called *hadrons* and to this date no isolated, colour-charged object has been observed. This phenomenon is known as *colour confinement*, whose reason is still unknown. The interaction between hadrons are due to residual strong forces analogous to the Van der Waals force in electrodynamics. There are two types of hadrons: *mesons*, which consist of one quark and an antiquark and *baryons* which consist of three quarks or three antiquarks.

It is interesting to consider a thought experiment in which we pull apart the two quarks inside a meson. The interaction field between them lies inside a *flux tube* which resembles a string that "glues" the two particles (hence is the name gluon). As we increase the distance between the quarks, the flux tube becomes more energetic. The string breaks when the energy it stores is enough to create a new pair of a quark and an antiquark, thus resulting in two mesons. If, instead of increasing the distance between the two quarks, we decrease the distance, the interaction strength becomes weaker and drops down to zero at zero distance. This phenomenon is known as *asymptotic freedom* and can be realised at extremely high-energetic collision experiments.

1.2 Lattice QCD (LQCD)

In line with asymptotic freedom, the coupling constant in QCD is small only in the extremely high-momentum region. Therefore the perturbative methods of QED are not applicable at low momenta and one should seek non-perturbative approaches. Lattice QCD (LQCD) has proven to be an effective non-perturbative method to study QCD at low momenta. In this method the space-time is discretized, forming a four-dimensional grid of points:

$$\Lambda = \{n = (n_1, n_2, n_3, n_4) | n_\mu = 0, 1, ..., N_{\mu-1}\}\,. \tag{1.3}$$

This sets a natural regularization to the ultra-violet divergences. The fermion field, ψ, lies on the lattice points, which are called the *sites* of the lattice and the gluons live on the *links,* U_μ, connecting these points. Unlike the continuum theory, these links turn out to be elements of the $SU(3)$ group rather than the $su(3)$ algebra, in order to have gauge invariance in the theory.

One should write the lattice version of the QCD continuum action, which is the integral of the Lagrangian density in eq. (1.2) over the whole space-time. The first discretized action that works on the lattice was proposed by Wilson:

$$S\left[\psi, \bar{\psi}, U\right] = S_G\left[U\right] + S_F\left[\psi, \bar{\psi}, U\right] \tag{1.4}$$

where

$$S_G\left[U\right] = \frac{\beta}{N} \sum_{n\in\Lambda} \sum_{\mu<\nu} \mathrm{Re}\left\{\mathrm{tr}\left[1 - U_{\mu\nu}\left(n\right)\right]\right\} \tag{1.5}$$

is the pure gluonic part. In eq. (1.5),

$$\beta = \frac{2N_c}{g^2}, \tag{1.6}$$

where, g is the bare coupling constant and N_c is the number of colours.

In eq. (1.5), $U_{\mu\nu}$ is a product of links which is called a *plaquette* and is defined as:

$$U_{\mu\nu}(n) = U_\mu(n) U_\nu(n+\hat{\mu}) U_{-\mu}(n+\hat{\mu}+\hat{\nu}) U_{-\nu}(n+\hat{\nu}). \tag{1.7}$$

In eq. (1.7), $\hat{\mu}$ denotes the unit vector in the direction of μ.

The fermionic part in eq. (1.4) is given by:

$$S_F\left[\psi, \bar{\psi}, U\right] = \sum_{f=1}^{N_f} a^4 \sum_{n,m\in\Lambda} \bar{\psi}^{(f)}\left(n\right) M^{(f)}\left(n|m\right) \psi^{(f)}\left(m\right) \tag{1.8}$$

and includes the interactions with the gauge field through the *fermion matrix* or *Dirac operator,* $M^{(f)}\left(n|m\right)$, whose inverse is the *quark propagator* on the lattice, for the non-interacting case. It is given by:

$$M^{(f)}\left(n|m\right) = \left(m^{(f)} + \frac{4}{a}\right)\delta_{nm} - \left(m^{(f)} + \frac{4}{a}\right)\kappa \sum_{\mu=\pm1}^{\pm4} \left(\mathbf{1} - \gamma_\mu\right) U_\mu\left(n\right) \delta_{n+\hat{\mu},m}. \tag{1.9}$$

In eq. (1.8) and eq. (1.9), a denotes the *lattice spacing,* which is the distance between two adjacent lattice sites. In eq. (1.9), a gamma matrix with a negative index is defined to be minus the matrix with the positive index, i.e., $\gamma_{-\mu} = -\gamma_\mu$, and $\kappa = \frac{1}{2(am^{(f)}+4)}$ is called the *hopping parameter.* If the hopping parameter is small (which is the case for large mass), M^{-1}, i.e. the quark propagator, can be expanded in powers of κ.

In this work we have used the Wilson action (with $N_f = 2$) but it should be noted that there are other actions that work on the lattice, i.e., the discretization is not unique and all actions have

their own advantages/disadvantages. For example the Wilson action violates chiral symmetry which becomes important if one wants to simulate with light quarks. In that case one may use *staggered fermions* instead. In this action, the four components of the Dirac spinor are placed on different sites of the lattice. In [6] staggered fermions are used to investigate two-colour QCD.

In order to employ the lattice as a tool for calculations, the most suitable approach to quantum field theory is the *Feynman path integral* formalism. There is a direct analogy between the expectation value of a product of operators in this formalism and an expectation value in statistical mechanics, so all the technology of statistical mechanics can be taken over. In this formalism one uses the Euclidean metric, and the expectation value of an observable is given by:

$$\langle O \rangle = \frac{1}{Z} \int \mathcal{D}U \mathcal{D}\psi \mathcal{D}\bar{\psi} \mathrm{e}^{-S_E[\psi,\bar{\psi},U]} O, \tag{1.10}$$

where Z is the partition function:

$$Z = \int \mathcal{D}U \mathcal{D}\psi \mathcal{D}\bar{\psi} \mathrm{e}^{-S_E[\psi,\bar{\psi},U]}. \tag{1.11}$$

Such integrals can be computed numerically on the lattice by using *Monte Carlo* algorithms. To obtain physical results, one should take the limit as the lattice spacing goes to zero (continuum limit) and the limit as the lattice size goes to infinity (thermodynamic limit). In practice this is done by doing the computation with several different lattice spacings and sizes, and then making the appropriate extrapolations to these limits. One should keep track of the finite volume and lattice spacing effects on the numerical results.

The integrals in eq. (1.10) and eq. (1.11) can be rewritten to give:

$$\langle O \rangle = \frac{1}{Z} \int \mathcal{D}U \, \mathrm{det}M \, \mathrm{e}^{-S_G[U]} O \tag{1.12}$$

and

$$Z = \int \mathcal{D}U \, \mathrm{det}M \, \mathrm{e}^{-S_G[U]}, \tag{1.13}$$

where $\mathrm{det}M$, the *fermion determinant*, is the determinant of the matrix given in eq. (1.9). Note that no direct dependence is left on the fermion fields, ψ and $\bar{\psi}$, which are independent quantities in the Euclidean treatment. The information coming from these fields are absorbed into the fermion determinant.

In a Monte Carlo simulation, the term $\mathrm{det}M \, \mathrm{e}^{-S_G[U]}$ in the integral in eq. (1.12) serves as a probability weight and the integral is approximated as a sum of terms weighted accordingly. For this, the fermion determinant is required to be real. This is satsfied as a result of the γ_5-hermiticity of the fermion matrix of the real QCD:

$$M^\dagger = \gamma_5 M \gamma_5, \tag{1.14}$$

which, in turn implies that the eigenvalues are either real or occur in conjugate pairs. It should be noted that the γ_5-hermiticity of the fermion matrix is valid for zero *chemical potential*, μ,

and the situation for non-zero chemical potential will be explained in the following section.

For an introductive and pedagogic source on LQCD the reader is referred to [7].

1.3 Two-Colour LQCD at Finite Density

1.3.1 Overview

As long as the theory is at zero density, i.e., in the absence of chemical potential, μ, the Monte Carlo technique works well and the phase diagram of QCD towards high temperatures has been effectively studied [8].

However, when the chemical potential is introduced, it turns out that the fermion determinant is not real for the group $SU(3)$, which is the relevant group of physical QCD. Therefore the term $\det M\, \mathrm{e}^{-S_G[U]}$ in the integral in eq. (1.12) can no longer be interpreted as a probability weight and the Monte Carlo technique fails. This is referred to as the *sign problem* and, to this date, no direct solution has been found to it. QCD at finite densities has rather been tackled indirectly, using *QCD-like* approaches. One such approach, which we follow in this work, is QCD with two colours, for which the relevant group is $SU\,(2)$ colour group.

In two colour QCD the fermion determinant turns out to be real as will be shown in Sec. 2.3. It is also positive for an even number of quark flavours and the interpretation of the term $\det M\, \mathrm{e}^{-S_G[U]}$ in the integral in eq. (1.12) as a probability weight is restored. The Monte Carlo technique is then available at finite density at the cost of now having an unphysical theory.

In this work we studied two-colour QCD at non-zero chemical potential on the lattice with two Wilson fermions. In this theory quarks and antiquarks live in equivalent representations of the colour group. Baryons of the theory are diquarks (to be explained in Sec. 2.2), and at zero chemical potential there is an exact symmetry between the diquarks and mesons. At zero chemical potential, the pseudo-Goldstone multiplet consists of the pion isotriplet plus a scalar isoscalar diquark and antidiquark.

The history of two-colour LQCD studies with non-zero chemical potential using Wilson fermions dates back to a 1984 paper by A. Nakamura [9] and it has been mainly studied by the Maynooth-Swansea collaboration since then [10, 11, 12, 13, 14, 15, 16, 17, 18, 19]. Another method that has been used to study two-colour LQCD at finite chemical potential is the staggered fermion formulation which was mentioned in Sec. 1.2 [20, 21, 22, 23, 24, 25, 26, 27]. Simon Hands and collaborators have also used staggered quarks *in the adjoint representation* to study two-colour QCD at finite chemical potential [28, 29, 30, 31]. This is another QCD-like approach in which quarks are assumed to live in the adjoint, rather than the fundamental, representation of the colour group. In this work we use the quarks in the fundamental representation of the $SU(2)$ colour group, like in real QCD with the $SU(3)$ colour group.

1.3.2 Classification According to Antiunitary Symmetry

There is an important classification of the Dirac operators that comes from the Random Matrix Theory [32] and we will classify some of the QCD-like theories according to the Dyson index, β, which is the number of independent degrees of freedom of the Dirac operator. Three important classes correspond to $\beta = 1$, $\beta = 4$ and $\beta = 2$. We will first consider the continuum case.

In the continuum, for two colour QCD with quarks in the fundamental representation, the Dirac operator has the following antiunitary symmetry:

$$[M, \tau_2 C \gamma_5 K] = 0. \tag{1.15}$$

In eq.(1.15), C is the charge conjugation matrix, τ_2 is the second Pauli matrix that acts in the colour space and K is the complex conjugation operator. There exists at least one basis in which the Dirac operator is real, since $(\tau_2 C K)^2 = 1$. This corresponds to $\beta = 1$.

An important feature of this antiunitary symmetry is that it is preserved even at non-zero chemical potential. The reality of the Dirac determinant, which allows one to make simulations in two-colour QCD as mentioned in the previous subsection, is a result of this fact. If, further, even number of quark flavours used, this guarantees a non-negative fermion determinant, as mentioned in the previous section.

For QCD with adjoint quarks, the antiunitary symmetry reads:

$$[M, C \gamma_5 K] = 0. \tag{1.16}$$

In this case we have $(CK)^2 = -1$ and this enables one to find a pseudoreal representation for the Dirac operator, rather than a real representation. The Dyson index is $\beta = 4$.

No antiunitary symmetry exists for real QCD Dirac operator, which is a complex matrix. This corresponds to Dyson index $\beta = 2$. Real QCD with three fundamental quarks is in this class.

In the previous section we mentioned that two-colour QCD can be studied on the lattice both by using Wilson quarks in the fundamental representation and by using the staggered fermion approach. The Dirac operator of Wilson quarks, like the Dirac operator in the continuum, is in the class with $\beta = 1$ while the one for the fundamental staggered quarks belongs to the class with $\beta = 4$.

1.3.3 Introduction of Temperature and the Chemical Potential

We have already mentioned that there is an analogy between the expectation value of an observable expressed in Feynman path integral formalism and that in statistical mechanics. Let us now write the Euclidean action in eq.s (1.10) and (1.11) as

$$S_E[\phi] = \int_0^\beta dt \int d^3x \mathcal{L}_E(\phi, \partial_\mu \phi), \tag{1.17}$$

where we have limited the time extent to a finite value, β, instead of infinity. On comparison with the expectation value in statistical mechanics, one sees that β in eq. (1.17) corresponds to inverse temperature. On the lattice we have

$$T = \frac{1}{\beta} = \frac{1}{aN_\tau}, \tag{1.18}$$

i.e., the temporal extent of the lattice is interpreted as the temperature and the limit $aN_\tau \to \infty$ corresponds to zero temperature. With this interpretation of the temporal lattice extent, one still needs $a \to 0$ for the continuum limit but needs $N_s/N_\tau \to \infty$, while keeping N_τ fixed for the thermodynamic limit at finite temperature.

Pursuing the analogy between Euclidean field theory and statistical mechanics, we introduce the chemical potential to the continuum action by adding the term $\mu\bar{\psi}\gamma_4\psi$. The corresponding Wilson fermion matrix on the lattice, for the non-interacting case, is given by:

$$M(\mu) = \delta_{xy} - \kappa \sum_{\nu} \left[(\mathbf{1} - \gamma_\nu)\, \mathrm{e}^{\mu\delta_{\nu 0}} \delta_{y,x+\hat{\nu}} + (\mathbf{1} + \gamma_\nu)\, \mathrm{e}^{-\mu\delta_{\nu 0}} \delta_{y,x-\hat{\nu}} \right]. \tag{1.19}$$

1.4 Other Lattice and Non-lattice Approaches to QCD at Finite Density

There are methods that have been used to study finite-density QCD which do not involve the lattice. In fact, some progress that has been achieved in QCD is due to the mutual benefits of non-lattice methods and LQCD can derive from each other. For example, the two-colour QCD spectrum, given in Sec. 1.3 is predicted by Chiral Perturbation Theory [33] and it is investigated using two-colour LQCD in this work and elsewhere. Conversely, in [34] the authors study two-colour QCD using (Polyakov-loop-extended) Nambu-Jona-Lasinio (NJL) model and compare their results with the information coming from LQCD. Another example of the interplay between the lattice and non-lattice methods is mentioned at the end of the next paragraph. Such methods do not employ the lattice tool as a means of calculation while they use other approximations. Of particular importance are Dyson-Schwinger Equations (DSE) and Chiral Perturbation Theory (χPT).

Dyson-Schwinger equations of QCD are the equations of motion of the theory. They are usually solved iteratively in the interaction picture. This is basically a series with an infinite number of terms. Therefore one needs to "truncate" this series. In [35] dense QCD was studied using DSE approach. LQCD helps to test some assumptions made that feed the dense region studies of DSE [36].

χPT is the study of QCD near the chiral limit. This is the limit where quarks have zero mass, as a result of which the chiral symmetry is restored. The effective degrees of freedom turn out to be pseudo-Goldstone bosons. It has been effectively studied by Kogut and collaborators [33].

Functional Renormalization Group (FRG) is a functional approach, related to DSE, that has been used to study QCD non-perturbatively. The idea is to find the effective action of the theory making use of renormalization group equations. In [37] it has been used to study two-colour QCD.

Another QCD-like, non-lattice approach is the large-N_c theory. In this theory the number of colours in QCD is treated as a variable parameter and, in particular, the consequences and the resulting phases are investigated as the number of colours tend to infinity [38].

Some of the approaches to QCD can be studied both on the lattice and without the lattice. One of them is the *isospin chemical potential method*. In this method there is an imbalance between the chemical potential for the up-quarks and that of the down-quarks:

$$\mu_u = \mu + \mu_I, \qquad \mu_d = \mu - \mu_I, \tag{1.20}$$

where μ_I is the isospin chemical potential. The advantage is that the theory does not have the sign problem. In [39] it has been studied analytically and in [40, 41] it has been studied on the lattice.

QCD at finite density has also been studied using *imaginary chemical potential*, which is yet another method to avoid the sign problem [42]. Analytic continuation is used to relate the phase diagram in the imaginary chemical potential region to that in the real chemical potential region.

Some other methods to mention are *reweighting method* [43], *density of states method* [44], and *complex Langevin* [45], which are all lattice methods.

1.5 Hybrid Monte Carlo (HMC) Simulations

1.5.1 Importance Sampling and Monte Carlo Simulations

The fundamental idea of a numerical simulation is to approximate integrals like eq. (1.12) by finite sums, whose calculation requires computer work. In a *Monte Carlo simulation*, points at which the observable in question is evaluated are randomly sampled and the integral is approximated as a sum over these values. However such finite sums would contain an enormous number of terms even for lattices of moderate sizes. Fortunately, due to the probability weight in eq. (1.12), most of these terms have negligible contribution to the integral so that one can approximate using a much smaller number of terms that are wisely chosen. Choosing the terms with significant contributions to the integral is called *importance sampling*. The integral is then approximated as the average calculated over N such *configurations*:

$$\langle O \rangle = \frac{1}{N} \sum_{j=1}^{N} O[U_j], \tag{1.21}$$

where U_j follow the distribution $\det M \, \mathrm{e}^{-S_G[U]}$ of eq. (1.12). In a Markov chain Monte Carlo simulation, we produce such configurations as a *Markov chain*. In a Markov chain the probability of going from one point in the configuration space to another depends only on these two points but not on the history of the sequence. The problem now is to construct a Markov chain of configurations. It turns out that the following *master equation* has to be satisfied:

$$P\left(U, t_{n+1}\right) - P\left(U, t_n\right) =$$

$$\sum_{U} \left[P\left(U, t_n\right) T\left(U \to U^{'}\right) - P\left(U^{'}, t_n\right) T\left(U^{'} \to U\right) \right]. \tag{1.22}$$

In eq. (1.22) $P\left(U, t_n\right)$ denotes the probability of being in the configuration U at time t_n and $T\left(U \to U^{'}\right)$ denotes the probability for a transition from configuration U to configuration $U^{'}$. For systems in equilibrium, the left hand side of eq. (1.22) vanishes and the most commonly used solution to the remaining equation is the *detailed balance condition*

$$P\left(U\right) T\left(U \to U^{'}\right) = P\left(U^{'}\right) T\left(U^{'} \to U\right), \tag{1.23}$$

which is sufficient but not necessary.

1.5.2 Metropolis Algorithm

Here we briefly discuss the most basic of all Monte Carlo algorithms, the Metropolis algorithm. It consists of two steps. In the first step one chooses a new configuration $U^{'}$ randomly in order to update a configuration U. In step two this new configuration is accepted with probability $\min\left(1, \frac{P\left(U^{'}\right)T\left(U^{'}\to U\right)}{P(U)T\left(U\to U^{'}\right)}\right)$. It is easy to see that this satisfies the detailed balance condition and in our theory this is equivalent to $\min\left(1, \mathrm{e}^{-\beta\Delta S}\right)$, where ΔS is the change in the action when U is replaced by $U^{'}$. Thus, a proposed new configuration is always accepted if there is a decrease in the action. Note that in this step *some* of those configurations corresponding to an *increase* in the action are also accepted. This corresponds to reproducing the quantum mechanical paths since otherwise only the classical path, which minimizes the action, would be produced. We repeat these steps for all gauge links on the lattice, which is called a *sweep*.

1.5.3 Hybrid Monte Carlo

Simulation methods like Metropolis algorithm consist of *local* moves of the Markov chain. This results in high autocorrelation as well as large relaxation times for the purposes of QCD. In order to avoid these disadvantages, one needs a simulation method that allows for *global* moves of the Markov chain. The most popular such method nowadays is the Hybrid Monte Carlo (HMC) algorithm [46].

HMC method extends the Hamiltonian by introducing conjugate momenta of the fields. For example, for a scalar field ϕ, the partition function becomes

$$Z = \int \mathcal{D}\pi\mathcal{D}\phi \mathrm{e}^{-H(\pi,\phi)}. \tag{1.24}$$

where

$$H = \frac{1}{2}\sum_x \pi_x^2 + S\left(\phi\right). \tag{1.25}$$

At first sight, this extension may seem redundant but it allows to make updates of the fields in a way that will be outlined in the following. From eq. (1.24) and eq. (1.25) we see that the momentum part is independent of ϕ and follows a gaussian distribution. This is suitable for a heatbath update, so we choose a new momentum randomly according to the distribution $\exp(-\pi_x^2/2)$. Next we update the field ϕ by solving Hamilton's equations of motion:

$$\frac{d\phi}{d\tau} = \frac{\partial H}{\partial \pi}, \qquad \frac{d\pi}{d\tau} = -\frac{\partial H}{\partial \phi}. \tag{1.26}$$

In eq. (1.26) we have introduced a fictitious time, τ. Note that the Hamilton's equations are not the equations of motion of the physical theory we want to study, but are equations of motion of the theory that corresponds to the "artificial" Hamiltonian of eq. (1.25). This step is called "molecular dynamics" update because it resembles that model, taking the fields from the pair (π, ϕ) to the pair $\left(\pi^{'}, \phi^{'}\right)$. It is basically solving these Hamilton's equations which makes the updates global. They are not solved exactly but are solved numerically.

We now have a new proposed pair of fields $\left(\pi^{'}, \phi^{'}\right)$. The final step is to employ the Metropolis algorithm for the acceptance. That is, we first calculate the change ΔH in the Hamil-

tonian by moving from (π, ϕ) to $\left(\pi', \phi'\right)$ and accept the new fields with the probability $\min[1, \exp(-\Delta H)]$. The time between two successive Metropolis acceptance/rejection is referred to as the *trajectory length*. We repeat this procedure a number of N times depending on our needs, and in the end we simply discard the auxiliary momenta that have been introduced. For a pedagogic source on HMC see [47].

1.6 Simulation Parameters and Outline of the Thesis

To extract physical information from lattice simulations, one needs controlled continuum limits. For a controlled continuum limit, one needs at least 3 lattice spacings. Our group so far has studied two-colour QCD on lattices with lattice spacings 0.223 fm (corresponding to $\beta = 1.7$) [19], 0.178 fm (corresponding to $\beta = 1.9$) [11] and in this work we extend our results on a yet finer lattice with a spacing of 0.1380^{+52}_{-72} fm and $\beta = 2.1$. In order to find the latter value, we set the scale using Regge trajectory. More will be said on the details of scale setting in Sec. 2.1. Table 1.1 gives the parameters our group has been using, together with the parameters we used in this work.

Table 1.1: Parameters that have been used in lattice studies by our group

β	κ	a(fm)	m_π/m_ρ	m_π(MeV)	Lattice Dimension
1.7	0.178	0.223	~ 0.8	688 ± 11	$8^3 \times 16$
1.9	0.168	0.178 ± 0.006	~ 0.8	717 ± 25	$16^3 \times 8$ $16^3 \times 12$ $12^3 \times 16$ $12^3 \times 24$ $16^3 \times 24$
2.1	0.1577	$0.1380^{+0.0052}_{-0.0072}$	~ 0.8	638 ± 33	$16^3 \times 12$ $16^3 \times 16$ $16^3 \times 20$ $16^3 \times 32$

Looking at Table 1.1, one notices that at all lattice spacings, the ratio m_π/m_ρ has been roughly preserved, which is needed in order to preserve the quark masses the same in all works. To preserve the ratio m_π/m_ρ, the parameter κ is adjusted accordingly.

Throughout this work, we present results corresponding to the last two rows of Table 1.1. The lattices with $\beta = 1.9$ and $a = 0.178 \pm 0.006$ fm will be referred to as the "coarser", and those with $\beta = 2.1$ and $a = 0.1380^{+0.0052}_{-0.0072}$ fm will be referred to as the "finer" lattice.

In Chapter 2, we give our results and discuss the phase transitions in two-colour QCD, studied with the parameters given above. Quantities like the static quark potential, diquark condensate and the quark number density are also discussed here.

Chapter 3 is devoted to the gluons in two-colour QCD. We compute the electric and the magnetic parts of the gluon propagator and discuss a functional form to fit these.

In Chapter 4 we investigate the quark propagator at finite density in two-colour QCD with two Wilson fermions. The numerical results for the form factors associated with the propagator are given and their physical interpretations are discussed.

In Appendix A we derive an expression that is given in Sec. 4.4 and in Appendix B we give a reproduction of the reference [48] which forms the basis of our discussion of the quark propagator at finite density.

We should note that the results on the *coarser* lattice in this work have been taken from the paper [11]. The author of this thesis was also involved in that work, producing the gluon data and making some of the plots of the gluon chapter. However, some plots from that work which are presented in the thesis does not belong to the author. These are Figures 2.2, 2.4, 2.10, 2.11, 3.1 and 3.10.

Some preliminary results of this work was previously presented by the author in [49].

Chapter 2

Phase Transitions in Two-Colour QCD

2.1 Static Quark Potential and Setting the Scale

Setting the scale in a LQCD work means to determine the size of the lattice spacing, a.

Expressed in terms of a, the observables calculated using LQCD are dimensionless. Scale setting is done by relating the experimental/numerical values of these observables to the values obtained from the lattice and solving for the lattice spacing. Examples of such observables are hadronic observables like the nucleon mass and the meson decay constants. One uses the experimental results for these observables to set the scale. A disadvantage with the nucleon mass is that the simulations themselves depend on the quark masses. Another type of observables that are used for scale setting is the pure gauge observables like the *glueballs* which are pure gluonic states that are colour-neutral. Their disadvantage is that there are no experimental values available for them while any numerical calculation is very expensive.

In this work we used the string tension, σ, obtained from the Regge trajectory to set the scale, which is around $\sigma = (450\,\mathrm{MeV})^2$. The idea is to make use of the experimental spectrum of hadronic masses plotted with respect to their angular momenta. This gives a linear curve, whose slope can be related to the string tension as

$$a^2\sigma = \text{Numerical Value}. \tag{2.1}$$

One can argue if it makes sense to use this experimental information coming from real QCD in a QCD-like theory like ours. The answer is that we *assume* the same value to hold in the two-colour theory. In this method of scale setting one should avoid working at high temperatures which may cause string breaking. In our work, the lattice with the largest temporal extent, corresponding to the lowest temperature, was $16^3 \times 32$ and we used this lattice to set the scale.

We first calculated the Wilson loops using a computer code. Using the gauge configurations for $16^3 \times 32$ at zero chemical potential, the code gave as an output, Wilson loop values of all possible spatial, R, and temporal, τ, sizes that can be formed on the lattice. The Wilson loop, $W(R,\tau)$, is related to the static quark potential, $V(R)$, via the relation:

$$W(R,\tau) \propto \mathrm{e}^{-V(R)\tau}, \tag{2.2}$$

and the next step is to fit, using another code, the Wilson loop data to an effective potential defined as:

$$aV_{\mathrm{eff}}(R,\tau) \equiv -\ln \frac{W(R,\tau+a)}{W(R,\tau)}. \tag{2.3}$$

This expression for the effective potential reaches to a plateau for sufficiently large τ. In other words, ground state dominance is achieved for large τ. In this calculation we took into account the first and the second half of the spatial lattice extension separately, in order to reduce the finite volume effect.

We fit the static quark potential to the Cornell potential given by:

$$V(R) = C + \sigma R + \frac{\alpha}{R}, \tag{2.4}$$

where C and α are constants. The string tension, σ, is then extracted from the static potential with respect to R. Since the effective potential does not reach a plateau for early values of τ, we ignore their contribution to improve the result. The minimum τ value taken into account is named as T_{min} and in Table 2.1, we list the fit parameters and the corresponding lattice spacing values found for various T_{min} values.

Table 2.1: Fit parameters and the corresponding lattice spacing values found for various T_{min}

T_{min}	σ	α	C	χ^2/N_{dof}	a
2	$0.1283^{+0.0009}_{-0.0009}$	$0.2179^{+0.0020}_{-0.0021}$	$0.5224^{+0.0029}_{-0.0029}$	2.45	$0.1706^{+0.0006}_{-0.0006}$
3	$0.0987^{+0.0015}_{-0.0015}$	$0.2578^{+0.0036}_{-0.0032}$	$0.5902^{+0.0050}_{-0.0051}$	1.25	$0.1496^{+0.0012}_{-0.0012}$
4	$0.0840^{+0.0065}_{-0.0086}$	$0.2779^{+0.0146}_{-0.0206}$	$0.6245^{+0.0286}_{-0.0200}$	0.249	$0.1380^{+0.0052}_{-0.0072}$

In Fig. 2.1, we give a plot for the static quark potential versus spatial separation of the Wilson loop on the finer $16^3 \times 32$ lattice for $\mu = 0$. The curves exhibit, within errors, the linear dependence of the static quark potential with respect to R. We should, however, note that a disadvantage of our method is that the error bars are quite big in the linear region as seen in the figure. Our best fit led to the value of $a = 0.1380^{+52}_{-72}$ fm for the lattice spacing, with $\chi^2/N_{dof} = 0.249$, and the minimum τ value taken into account was $T_{min} = 4$.

2.2 Phase Structure of QCD and Two-Colour QCD

Before we investigate the phase transitions in two-colour QCD, an overview of the phase structure is in order.

Let us first consider real QCD with three colours. It has a rich phase structure as the control parameters temperature and baryon chemical potential change. The extreme dense and cold region is believed to exist in the cores of neutron stars. Little is known about this region, which is one of the motivations to study the extreme dense medium of QCD. The extreme hot and zero-density region is believed to have existed in the early universe and is realised by heavy ion collision experiments.

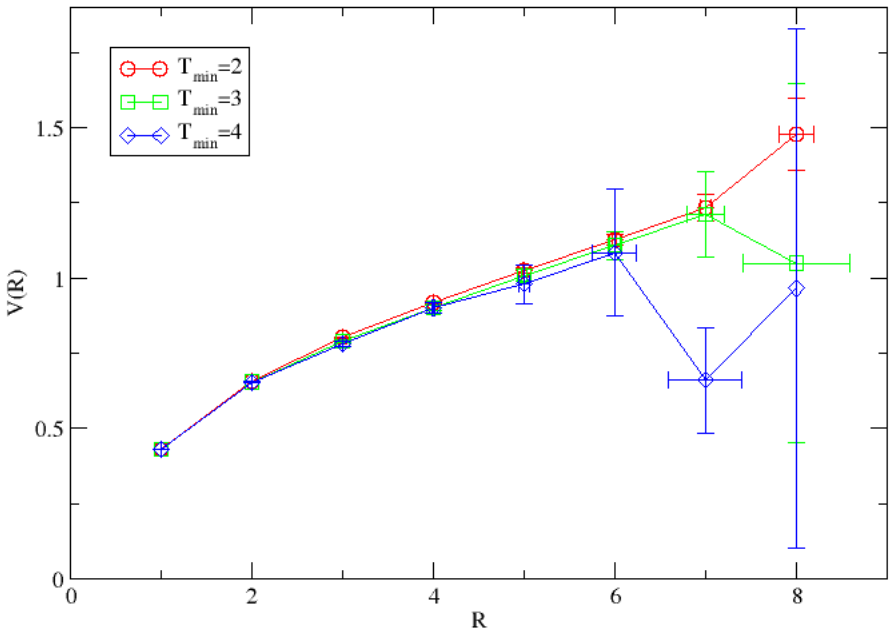

Figure 2.1: Static quark potential versus spatial separation of the Wilson loop on the finer $16^3 \times 32$ lattice for $\mu = 0$.

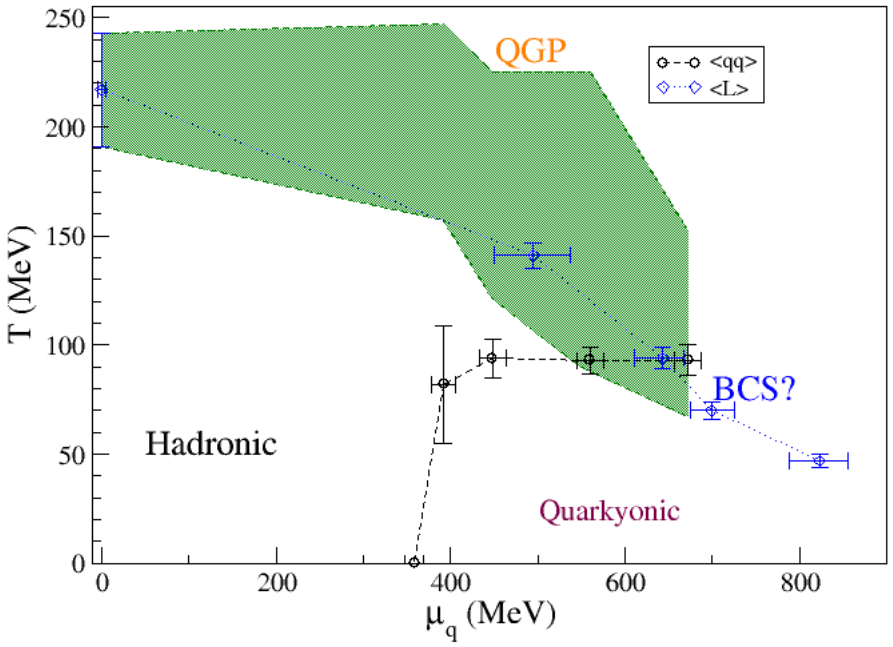

Figure 2.2: Tentative Phase Diagram of Two-Colour QCD (courtesy Dr. Jon-Ivar Skullerud). The black circles indicate the phase transition from normal to superfluid phase. The green region is the crossover between the hadronic & quarkyonic phase and the quark-gluon plasma. The blue diamonds are the Polyakov loop values at which deconfinement occurs.

Mesons and baryons exist in the cold and low-density region. Above a critical temperature, there is a transition to a phase called the quark-gluon plasma. In this phase, the degrees of freedom are no longer composite hadrons but are quarks and gluons.

Below this critical temperature, there is another phase transition as the chemical potential increases. This is a kind of quark matter. The nuclei are so densely packed that quarks are free to move, due to asymptotic freedom, and it is no longer clear which quark belongs to which nucleon. The degrees of freedom are therefore quarks.

If the density increases further at low temperature, there occurs a pairing mechanism of quarks which gives rise to a colour superconductor phase. This is analogous to the BCS pairing of electrons in condensed matter physics.

We now return to two-colour QCD and consider a tentative phase diagram of two-colour QCD shown in Fig. 2.2, taken from [11].

In the low μ and low T region there is a hadronic phase, where the degrees of freedom are hadrons of the theory and quarks and gluons are confined. As the chemical potential increases at low temperature and below the blue diamonds, there is a transition to quarkyonic region. In this phase the bulk observables depend on quark, rather than hadronic, degrees of freedom whereas the quarks are still confined.

The black circles that separate this region from the hadronic phase denote the pseudocritical points for *normal to superfluid phase transition*, which will be discussed in Sec. 2.3. They

correspond to the *diquark condensate* values which is the order parameter of this transition. In two-colour QCD, this transition coincides with the *onset transition*, which means a transition from zero baryon number density to a non-zero baryon number density. Once the chemical potential reaches the value for the onset transition, it is seen that normal to superfluid phase transition hardly depends on the chemical potential.

Another order parameter shown is denoted by the blue diamonds, which are the Polyakov loop values at μ_d, i.e., the chemical potential value at which the *deconfinement phase transition* occurs. This will be discussed in Sec. 2.5.

The green region denotes a crossover between hadronic & quarkyonic phases and the quark-gluon plasma. The latter is the phase in which the degrees of freedom are deconfined quarks and gluons. A crossover between these phases means that in this region the phases are indistinguishable from each other and there is no order parameter that is zero in one phase and non-zero in the other.

At moderate temperatures and beyond the blue curve, there is a possible BCS phase which will be discussed in Sec. 2.3. This is the phase in which quarks are paired by a mechanism similar to the BCS pairing in condensed matter physics, which gives rise to a superfluid phase that is analogous to the superconducting phase in real QCD. This is a superfluid, rather than a superconducting, phase since, unlike in real QCD, the paired quarks are gauge invariant objects. At lower chemical potential it is also suspected that there is a Bose-Einstein condensed phase of quarks and a crossover between the BEC and the BCS region.

2.3 Diquark Condensate and Normal to Superfluid Phase Transition

In $SU(2)$ the quarks and antiquarks are in equivalent representations. This gives rise to a symmetry that is known as the Pauli-Gürsey symmetry:

$$KM(\mu)K^{-1} = M(\mu)^*, \tag{2.5}$$

where $M(\mu)$ is the fermion matrix introduced in Subsec. 1.3.1, and

$$K = C\gamma_5\tau_2. \tag{2.6}$$

In eq. (2.6) C is the charge conjugation matrix and τ_2 is the second Pauli matrix that acts in the colour space. It is this symmetry that ensures the reality of the fermion determinant even at finite chemical potential. To show this, we make use of eq. (2.5). We have

$$[\det M(\mu)]^* = \det[M^*(\mu)]$$

$$= \det\left[KM(\mu)K^{-1}\right]$$

$$= \det\left[KK^{-1}M(\mu)\right]$$

$$= \det\left[M\left(\mu\right)\right]. \tag{2.7}$$

Therefore we conclude

$$\det\left[M\left(\mu\right)\right] = \det\left[M\left(\mu\right)\right]^{*} \in \mathbb{R}. \tag{2.8}$$

It will be instructive to have a look at the continuum theory and with $m = \mu = 0$ first. The fermionic part of the Lagrangian density for this case is given by $\mathcal{L} = \bar{\psi}\gamma_\nu M_\nu \psi$, which can be rewritten as:

$$\mathcal{L} = \bar{\psi}\gamma_\nu M_\nu \psi = i \begin{pmatrix} \psi_L^* \\ \psi_R^* \end{pmatrix}^T \begin{pmatrix} \sigma_\nu M_\nu & 0 \\ 0 & -\sigma_\nu^\dagger M_\nu \end{pmatrix} \begin{pmatrix} \psi_L \\ \psi_R \end{pmatrix}. \tag{2.9}$$

To verify this, let us first consider the right hand side. We have:

$$i \begin{pmatrix} \psi_L^* \\ \psi_R^* \end{pmatrix}^T \begin{pmatrix} \sigma_\nu M_\nu & 0 \\ 0 & -\sigma_\nu^\dagger M_\nu \end{pmatrix} \begin{pmatrix} \psi_L \\ \psi_R \end{pmatrix} = i\psi_L^\dagger \sigma_\nu M_\nu \psi_L - i\psi_R^\dagger \sigma_\nu^\dagger M_\nu \psi_R$$

$$= i\psi_L^\dagger \sigma_0 M_0 \psi_L + i\psi_L^\dagger \sigma_j M_j \psi_L - i\psi_R^\dagger \sigma_0^\dagger M_0 \psi_R - i\psi_R^\dagger \sigma_j^\dagger M_j \psi_R$$

$$= \psi_L^\dagger M_0 \psi_L + \psi_R^\dagger M_0 \psi_R + i\psi_L^\dagger \sigma_j M_j \psi_L - i\psi_R^\dagger \sigma_j M_j \psi_R. \tag{2.10}$$

We will now rewrite the left hand side of eq. (2.9) and show that it is equal to eq. (2.10).

$$\bar{\psi}\gamma_\nu M_\nu \psi = \bar{\psi}_L \gamma_\nu M_\nu \psi_L + \bar{\psi}_R \gamma_\nu M_\nu \psi_R$$

$$= \psi_L^\dagger \gamma_0 \gamma_\nu M_\nu \psi_L + \psi_R^\dagger \gamma_0 \gamma_\nu M_\nu \psi_R$$

$$= \psi_L^\dagger \gamma_0^2 M_0 \psi_L + \psi_R^\dagger \gamma_0^2 M_0 \psi_R + \psi_L^\dagger \gamma_0 \gamma_j M_j \psi_L + \psi_R^\dagger \gamma_0 \gamma_j M_j \psi_R$$

$$= \psi_L^\dagger M_0 \psi_L + \psi_R^\dagger M_0 \psi_R + \left(\psi_L^\dagger, 0\right) \begin{pmatrix} i\sigma_j M_j & 0 \\ 0 & -i\sigma_j M_j \end{pmatrix} \begin{pmatrix} \psi_L \\ 0 \end{pmatrix}$$

$$+ \left(0, \psi_R^\dagger\right) \begin{pmatrix} i\sigma_j M_j & 0 \\ 0 & -i\sigma_j M_j \end{pmatrix} \begin{pmatrix} 0 \\ \psi_R \end{pmatrix}$$

$$= \psi_L^\dagger M_0 \psi_L + \psi_R^\dagger M_0 \psi_R + i\psi_L^\dagger \sigma_j M_j \psi_L - i\psi_R^\dagger \sigma_j M_j \psi_R \tag{2.11}$$

Hence we have

$$\bar{\psi}\gamma_\nu M_\nu \psi = i \begin{pmatrix} \psi_L^* \\ \psi_R^* \end{pmatrix}^T \begin{pmatrix} \sigma_\nu M_\nu & 0 \\ 0 & -\sigma_\nu^\dagger M_\nu \end{pmatrix} \begin{pmatrix} \psi_L \\ \psi_R \end{pmatrix}. \tag{2.12}$$

In eq. (2.12), $\sigma_\nu = (-i, \sigma_k)$ where σ_k are the Pauli matrices. This can be rewritten as:

$$\mathcal{L} = \bar{\psi}\gamma_\nu M_\nu \psi = i \begin{pmatrix} \psi_L^* \\ \tilde{\psi}_R^* \end{pmatrix}^T \begin{pmatrix} \sigma_\nu M_\nu & 0 \\ 0 & \sigma_\nu M_\nu \end{pmatrix} \begin{pmatrix} \psi_L \\ \tilde{\psi}_R \end{pmatrix} = i\Psi^\dagger \sigma_\nu M_\nu \Psi. \tag{2.13}$$

In eq. (2.13) $\tilde{\psi}_R = \sigma_2 \tau_2 \psi_R^*$, which transforms in the same representation as ψ_L so that the

Lagrangian of eq. (2.13) has a manifest $U(2N_f)$ symmetry. The corresponding symmetry is reduced to $SU(2N_f)$ in the quantum theory because of the axial anomaly.

In the *chiral limit,* i.e., for massless quarks and at zero chemical potential the Pauli-Gürsey symmetry implies an exact symmetry between the mesons $\bar{\psi}\psi$, and *diquarks*:

$$\psi\psi \equiv \psi^T C\gamma_5\tau_2\psi. \tag{2.14}$$

The latter are baryons of the theory. As a result of this symmetry, it requires zero energy to rotate the ground states with non-zero $\langle\bar{\psi}\psi\rangle$ into the ground states with non-zero $\langle\psi\psi\rangle$. If the quark mass is non-zero this symmetry is spoiled and there is a distinction between the diquark condensate and the chiral condensate. In the continuum the chemical potential is introduced into the Lagrangian through a term:

$$\mu\bar{\psi}\gamma_0\psi = \mu\psi^\dagger\psi, \tag{2.15}$$

and a competition between the diquark condensate and the chiral condensate occurs. As the chemical potential increases, the $\langle\psi\psi\rangle$ becomes dominant which signals *normal to superfluid phase transition.*

There are two paradigms to explain the *diquark condensation.* The first one, the Bose-Einstein condensation (BEC), takes place in the chemical potential limit that approaches the onset transition value from the right, i.e., $\mu \to \mu_{o+}$. In this regime, chiral perturbation theory predicts the following analytic behaviour for the diquark condensate [33]

$$\langle\psi\psi\rangle \propto \sqrt{1-\left(\frac{\mu_0}{\mu}\right)^4}. \tag{2.16}$$

This behaviour has been observed numerically with staggered fermions.

The other paradigm takes over the Bardeen-Cooper-Schrieffer (BCS) pairing mechanism of fermions in the condensed matter physics. At large chemical potential and low temperature, those quarks whose energies are close to the Fermi energy are expected to pair up, giving rise to diquark condensation. In two-colour QCD, this is a superfluid phase. As a result of this, there occurs a superfluid gap. Note that this pairing up is more easily explained compared to condensed matter physics because, unlike the situation there, the interaction between the quarks is already attractive.

To calculate the diquark condensate on the lattice, one introduces a term into the Lagrangian, which involves the diquark source, j:

$$\mathcal{L} = \mathcal{L}_0 + j\psi^T\mathcal{C}\gamma_5\tau_2\psi. \tag{2.17}$$

The diquark source has the effect of lifting low-lying eigenmodes in the superfluid phase. It also prevents the slowing down of the numerical computation which is observed as $j \to 0$. The reason for this slowing down can be understood as follows. The diquark condensate is responsible for the spontaneous breaking of $U(1)_B$ symmetry, and gives rise to an exact, i.e., massless Goldstone boson, which in turn means the fermion matrix becomes singular. HMC and calculation of fermionic observables require inversion of fermion matrix and therefore the calculation of the diquark condensate without diquark source, $j = 0$, in principle needs an

infinitely long time to compute.

The expectation value $\langle \psi^T \mathcal{C}\gamma_5\tau_2\psi \rangle$ is the diquark condensate and in the following we will use the shorthand notation, $\langle \psi\psi \rangle$, for it. At the end of the calculation, the limit is taken as the diquark source goes to zero. This can be expressed analytically as

$$\langle \psi\psi \rangle = - \left. \frac{\partial \ln z}{\partial j} \right|_{j\to 0} . \tag{2.18}$$

Numerically this limit is achieved by computing with several diquark source values and then extrapolating to zero diquark source.

The diquark condensate is not consistent with the global symmetry: The transformations

$$\psi \to \mathrm{e}^{\mathrm{i}\phi}\psi, \qquad \psi^T \to \mathrm{e}^{\mathrm{i}\phi}\psi^T \tag{2.19}$$

imply

$$\langle \psi^T \mathcal{C}\gamma_5\tau_2\psi \rangle \to \mathrm{e}^{2\mathrm{i}\phi} \langle \psi^T \mathcal{C}\gamma_5\tau_2\psi \rangle . \tag{2.20}$$

As a result, such a quantity can not exist in a vacuum with zero chemical potential, because the Lagrangian that describes the vacuum with $\mu = 0$ satisfies the global symmetry, which leads to the conservation of baryon number.

Fig. 2.3 is a plot for the diquark condensate versus temperature at different chemical potentials computed on the finer lattice. The data have been extrapolated to $j = 0$ using a linear functional form: $\langle qq \rangle = A + Bj$. It is seen that the diquark pairs break down as the temperature is increased. As we have few temperature values available at the moment, it is not yet possible to accurately determine the critical temperature, T_c, of the phase transition. However, it is remarkable to observe that T_c is independent of the chemical potential as we see that in Fig. 2.3 the inflection point does not change with respect to μ.

Table 2.2 shows the χ^2/N_{dof} values for the linear fit on the finer $16^3 \times 32$ lattice. We see that at low chemical potentials the fits are not good.

Table 2.2: χ^2/N_{dof} values for the linear fit on the finer $16^3 \times 32$ lattice

μ	0.15	0.20	0.25	0.30	0.35	0.40
χ^2/N_{dof}	111	20.9	2.07	13.8	3.54	9.72

In Fig. 2.4 we give a plot for the diquark condensate versus temperature at different chemical potentials computed on the coarser lattice. Again, we see the breaking down of the diquark pairs with temperature increase. The critical temperature for the phase transition looks similar on both the finer and the coarser lattice, while it is slightly lower on the finer lattice. The fact that the critical temperature is independent of the chemical potential can be observed even more clearly in this figure.

As mentioned above, the BCS pairing of quarks requires the formation of a Fermi surface and the quarks that lie close to this surface from above and below the Fermi level participate in the diquark condensation.

The expectation value $\langle \psi\psi \rangle$ therefore should be proportional to the area of the Fermi surface which suggests the relation:

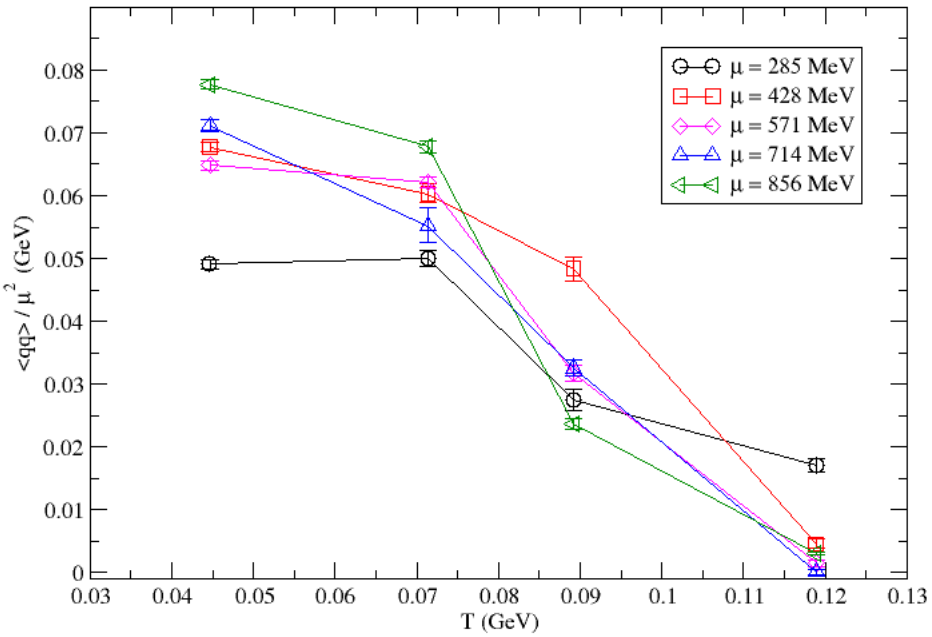

Figure 2.3: Diquark condensate versus temperature on the finer, $16^3 \times 12, 16, 20$ and 32 lattices. Data extrapolated to $j = 0$, using linear fit, at the five chemical potential values shown.

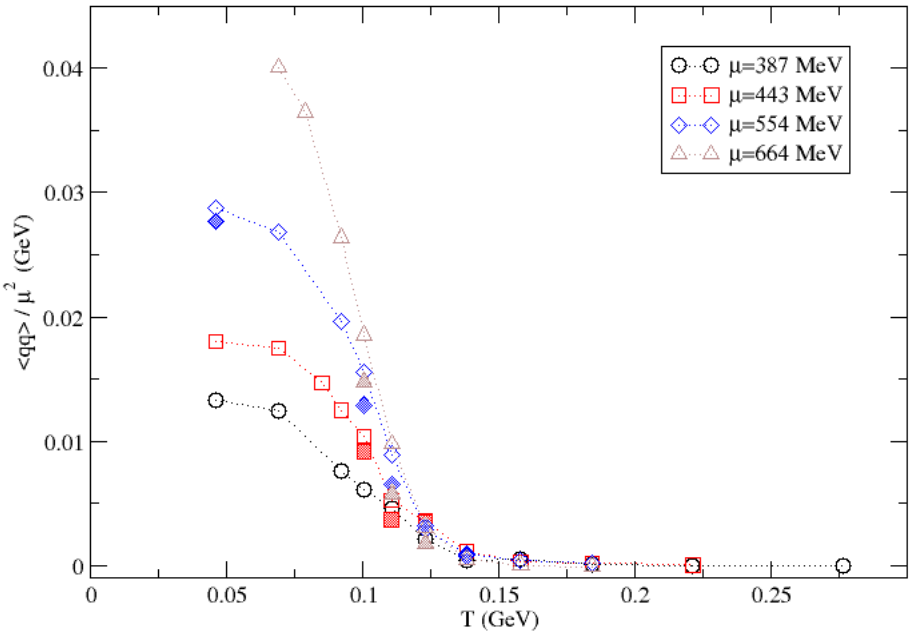

Figure 2.4: Diquark condensate versus temperature on a coarser lattice with $\beta = 1.9$ and $\kappa = 0.1680$. Data extrapolated to $j = 0$, using linear fit, at the four chemical potential values shown. The shaded circles are the results extrapolated from $ja = 0.02$ and $ja = 0.03$ only. The remaining data have been extrapolated from $ja = 0.04, 0.03$ and $ja = 0.02$.

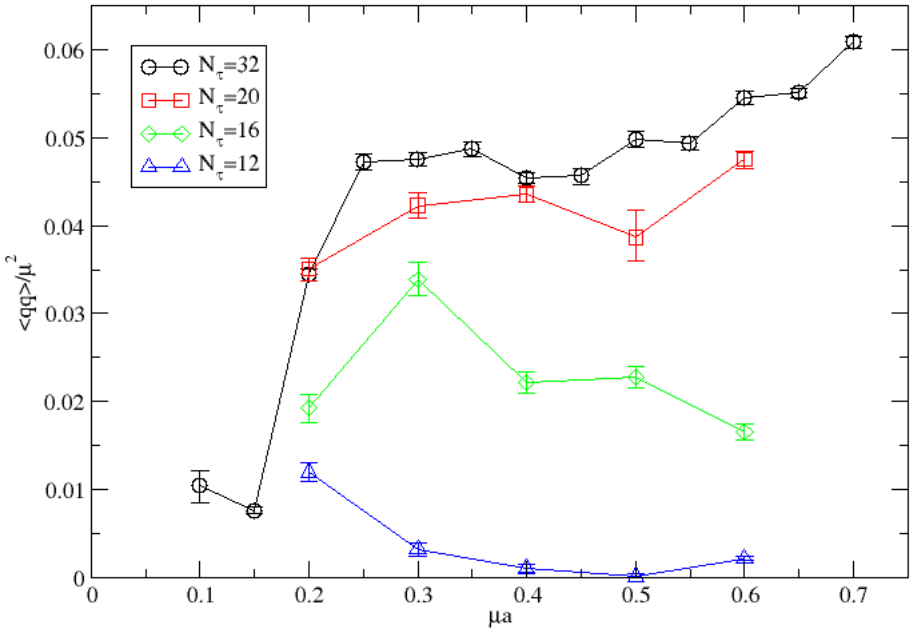

Figure 2.5: Diquark condensate divided by μ^2 versus chemical potential calculated at four different temperatures on the finer $16^3 \times N_\tau$ lattices. Data extrapolated to $j = 0$ from $ja = 0.02$ and $ja = 0.03$ using linear fit.

$$\langle \psi\psi \rangle \propto \mu^2. \tag{2.21}$$

We therefore normalize the diquark condensate values dividing by μ^2. The results are shown in the plots at different temperatures in Fig. 2.5.

The plateaux observed towards high densities support the BCS model explained above. However this behaviour is observed to break down as the temperature is increased due to the breaking of diquark pairs. Also note that below the onset transition chemical potential, i.e., for $\mu a \lesssim 0.2$ we see that the diquark condensate is non-zero, whereas it should be zero below the onset transition. This, we interpret to be an artefact of the linear extrapolation which is used here and is a sign that it is insufficient. We also see that the overall values for $\langle qq \rangle / \mu^2$ decrease as the temperature increases.

2.3.1 Other Extrapolation Methods

In Fig. 2.6, we give diquark condensate extrapolation results obtained using an inverse cubic fit function ($\langle qq \rangle = A + Bj^{1/3}$), which did not work.

The physical motivation to use the inverse cubic fit function was to use the expression for the diquark source in terms of the diquark condensate, given by the chiral perturbation theory:

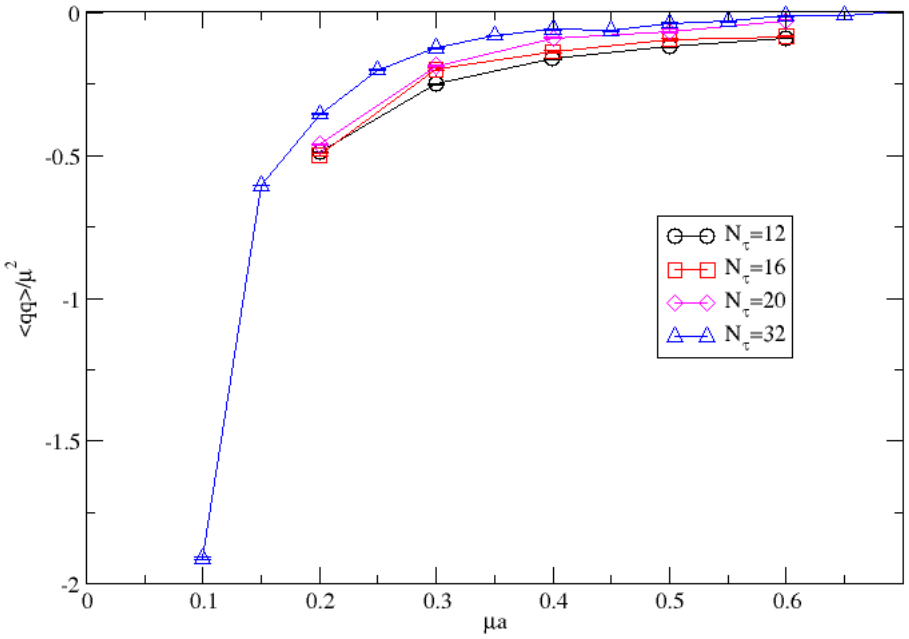

Figure 2.6: Diquark condensate divided by μ^2 versus chemical potential, calculated at four different temperatures on the finer $16^3 \times N_\tau$ lattices, extrapolated using an inverse cubic fit function. For $N_\tau = 32$, the data have been extrapolated to $j = 0$ from $ja = 0.01$, $ja = 0.02$ and $ja = 0.03$ at $\mu a = 0.15, 0.20, 0.30, 0.35$ and 0.40. All the remaining data have been extrapolated from $ja = 0.02$ and $ja = 0.03$.

$$j = \frac{\delta}{\sqrt{1-\delta^2}} - x^2\delta. \tag{2.22}$$

In eq. (2.22), j is the diquark source, δ is the diquark condensate and x is the ratio of the chemical potentials $x = \frac{\mu}{\mu_{\text{onset}}} = \frac{2\mu}{m_\pi}$. Using the binomial expansion we obtain:

$$j = \delta\left[1 + \left(-\frac{1}{2}\right)\left(-\delta^2\right) + ...\right] - x^2\delta$$

$$= \delta + \frac{1}{2}\delta^3 - x^2\delta + \mathcal{O}\left(\delta^5\right)$$

$$\implies j = \left(1 - x^2\right)\delta + \frac{1}{2}\delta^3 + \mathcal{O}\left(\delta^5\right). \tag{2.23}$$

Note that in order for this expansion to make mathematical sense, one must have $\delta < 1$, and to make physical sense, one must have $x \leq 1$ since otherwise the diquark source would be negative. Omitting $\mathcal{O}\left(\delta^5\right)$ terms in eq. (2.23), we are left with a cubic functional form:

$$j = a\delta + b\delta^3. \tag{2.24}$$

We want to write δ in terms of j. However, this involves solving a cubic equation. Instead, we used the following "inverse cubic" approximation in our code (with $\delta \to \langle qq \rangle$):

$$\langle qq \rangle = A + Bj^{1/3}. \tag{2.25}$$

Apart from the inverse cubic functional form, we tried quadratic ($\langle qq \rangle = Bj^2$) and power ($\langle qq \rangle = Bj^\alpha$) functional forms in the extrapolation. However they did not work satisfactorily. The results are plotted in Fig. 2.7.

2.4 Quark Number Density

Another quantity associated with the onset transition is the quark number density. In the BCS mechanism this quantity is proportional to the volume of the Fermi sphere, suggesting the relation:

$$n_q \propto \mu^3. \tag{2.26}$$

A plot of the quark number density versus the chemical potential is given in Fig. 2.8. It is seen that dependence on the diquark source becomes very weak above $\mu a \gtrsim 0.3$.

The quark number densities are normalized by the Stefan Boltzmann ideal gas expression for massles quarks in the continuum, given by:

$$n_{SB} = N_f N_c\left(\frac{\mu T^2}{3} + \frac{\mu^3}{3\pi^2}\right) = 4\left(\frac{\mu T^2}{3} + \frac{\mu^3}{3\pi^2}\right). \tag{2.27}$$

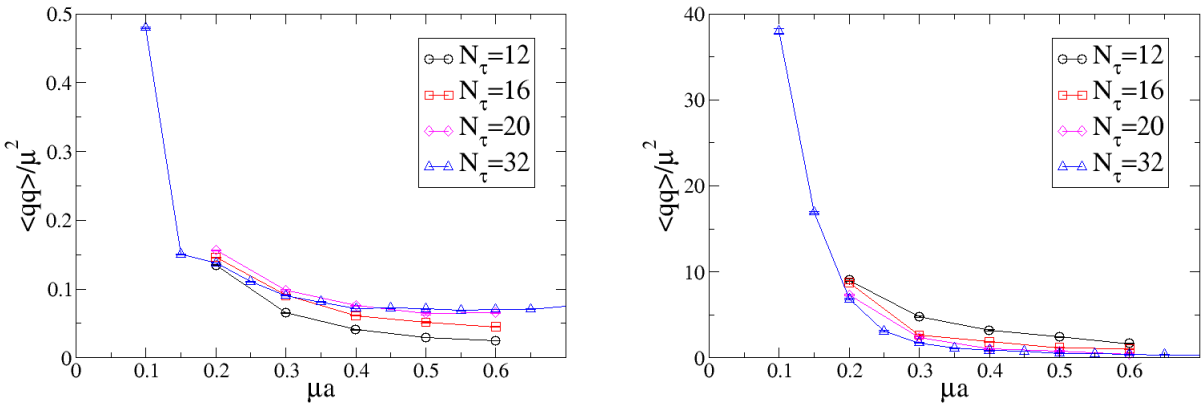

Figure 2.7: Diquark condensate divided by μ^2 versus chemical potential, calculated at four different temperatures on the finer $16^3 \times N_\tau$ lattices, extrapolated using quadratic (left) and power (right) fit functions. For $N_\tau = 32$, the data have been extrapolated to $j = 0$ from $ja = 0.01$, $ja = 0.02$ and $ja = 0.03$ at $\mu a = 0.15, 0.20, 0.30, 0.35$ and 0.40. All the remaining data have been extrapolated from $ja = 0.02$ and $ja = 0.03$.

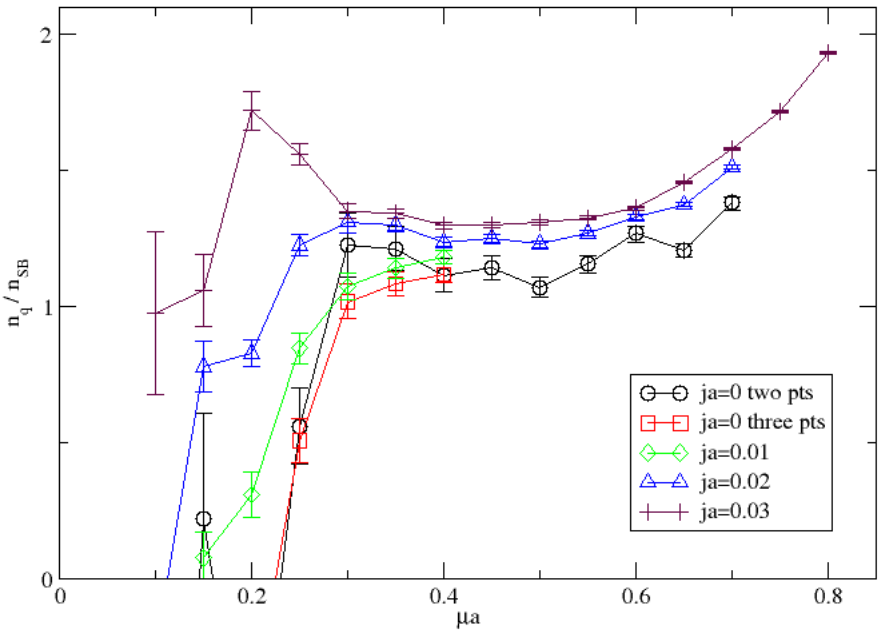

Figure 2.8: Quark number density normalized by the Stefan-Boltzmann number density versus chemical potential calculated on the finer $16^3 \times 32$ lattice. Black circles denote data extrapolated to $j = 0$ using two j values while the red squares denote the same using three j values. Linear extrapolation was used. Also shown are the data corresponding to $ja = 0.01, 0.02$ and 0.03.

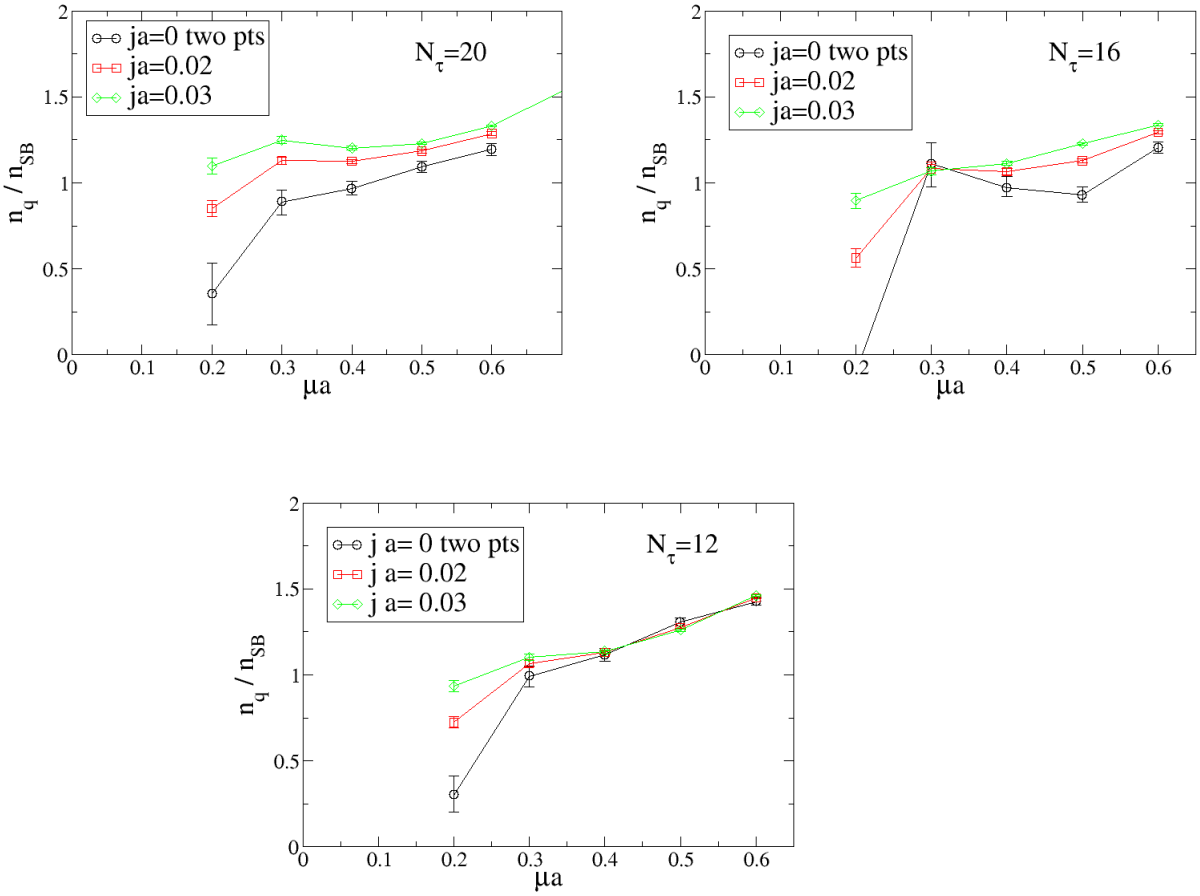

Figure 2.9: Quark number density normalized by the Stefan-Boltzmann number density versus chemical potential calculated on the finer $16^3 \times N_\tau$ lattices corresponding to three different temperatures. $j = 0$ data was extrapolated from two j values using linear fit. Also shown are the data corresponding to $ja = 0.02$ and $ja = 0.03$.

On the lattice, the corresponding expression for the quark number density reads:

$$n_{SB}^{lat} = \frac{4N_f N_c}{N_s^3 N_t} \sum_k \frac{i \sin \tilde{k}_0 \left[\sum_i \cos k_i - \frac{1}{2\kappa}\right]}{\left[\frac{1}{2\kappa} - \sum_\nu \cos \tilde{k}_\nu\right]^2 + \sum_\nu \sin^2 \tilde{k}_\nu}, \tag{2.28}$$

where

$$\tilde{k}_\nu = \begin{cases} k_0 - i\mu = \frac{2\pi}{N_t}\left(n_0 + \frac{1}{2}\right) - i\mu, & \nu = 0, \\ k_\nu = \frac{2\pi n_\nu}{N_s}, & \nu = 1, 2, 3. \end{cases} \tag{2.29}$$

We see a clear plateau around $\frac{n_q}{n_{SB}} = 1$, over the range $\mu a = 0.3 - 0.7$ which indicates that the system behaves like a Stefan-Boltzmann gas. This can be interpreted to be a result of the fact that, at high densities the interaction between the quarks becomes weak due to the asymptotic freedom. However, this chemical potential range shortens as the temperature is increased, which is seen in Fig. 2.9.

In Fig. 2.10 we give a plot for the quark number density versus temperature at different chemical

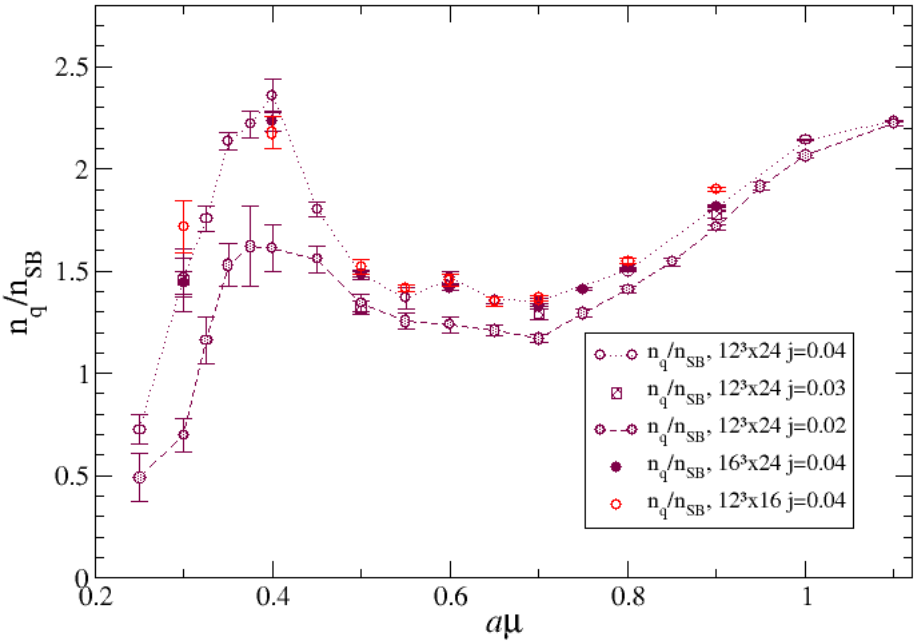

Figure 2.10: Quark number density normalized by the Stefan-Boltzmann number density versus chemical potential calculated on the coarser lattice. Linear extrapolation was used.

potentials computed on the coarser lattice. Like the quark number density on the finer lattice, we observe a plateau, roughly in the domain between $\mu a = 0.5$ and $\mu a = 0.8$. The qualitative behaviours agree on different volumes and the quantitative volume dependence is not big.

2.5 Deconfinement Transition

2.5.1 Polyakov Loop

Before discussing the decofinement phase transition, we introduce the Polyakov loop, whose expectation value is the order parameter for this phase transition. It is defined, on the lattice, as the product of the link variables along the time direction corresponding to a fixed spatial position:

$$L\left(\boldsymbol{n}\right) = \mathrm{tr}\left[\prod_{i} U_4\left(\boldsymbol{n}, i\right)\right]. \tag{2.30}$$

This is a closed loop due to boundary conditions. Being a trace over a closed loop, it is a gauge invariant object. However it is not symmetric under *centre transformations*, which consist of multiplying all the temporal gauge links by the same element, z, of the centre of the $SU\left(N_c\right)$ colour group:

$$L(\boldsymbol{n}) \longrightarrow \mathrm{tr}\left[\prod_i zU_4(\boldsymbol{n}, i)\right] = zL(n). \tag{2.31}$$

In real QCD, where the relevant group is $SU(3)$, the centre elements are $\left\{\mathbf{1}, \mathbf{1}e^{2\pi i/3}, \mathbf{1}e^{-2\pi i/3}\right\}$. In two-colour QCD, the gauge group is $SU(2)$ and the centre elements are $\{\mathbf{1}, -\mathbf{1}\}$.

On the other hand, the action is symmetric under centre transformations, as it consists of loops that wind around the same temporal links twice and in the opposite directions, as a result of which the factors that appear due to the transformation (z and $z^\dagger$) cancel each other.

If we put these together, we have a transformation under which the action of the theory is invariant, and we have an object, the Polyakov loop, that is defined on the lattice, which is not consistent with this symmetry. As a result, a non-zero expectation value of the Polyakov loop indicates spontaneous breaking of the centre symmetry.

Breaking of the centre symmetry indicates a transition from a confined to a deconfined phase, which was first realized by 't Hooft [50]. On the other hand, the expectation value of the Polyakov loop is related to the free energy of a static quark, F:

$$\langle L \rangle \sim \exp(-\beta F). \tag{2.32}$$

In the confined phase the free energy is infinite, which corresponds to a zero expectation value of the Polyakov loop. In the deconfined phase, the Polyakov loop takes a non-zero value which also indicates the spontaneous breaking of the centre symmetry.

2.5.2 Results

As discussed in the last subsection, the order parameter for deconfinement of quarks in LQCD is the expectation value of the Polyakov loop, $\langle L \rangle$. It becomes non-zero in the deconfined phase. In fact with the dynamical fermions studied in this work, it is literally never zero. In this case we decide the occurrence of the transition to a deconfined phase when we observe $\langle L \rangle$ going from very low values to high values. The renormalization of the Polyakov loop depends on the temperature via the relation:

$$L_R(T, \mu) = Z_L^{N_\tau} L_0\left(\frac{1}{aN_\tau}, \mu\right). \tag{2.33}$$

We first studied deconfinement on the coarser lattice. The renormalization has been done according to the following scheme:

$$L_R\left(T = \frac{1}{4a}, \mu = 0\right) = 1. \tag{2.34}$$

Fig. 2.11 (data taken from [11]) shows the Polyakov loop with respect to temperature on the coarser lattice at four non-zero chemical potentials and the vacuum. At all chemical potentials there is no rapid increase in the Polyakov loop, which suggests that it is not a true phase transition but is rather a crossover. An important information that can be inferred from the figure is that the increase in the chemical potential lowers the deconfinement temperature. This is expected since it takes less energy for the baryons to deconfine in a more dense medium.

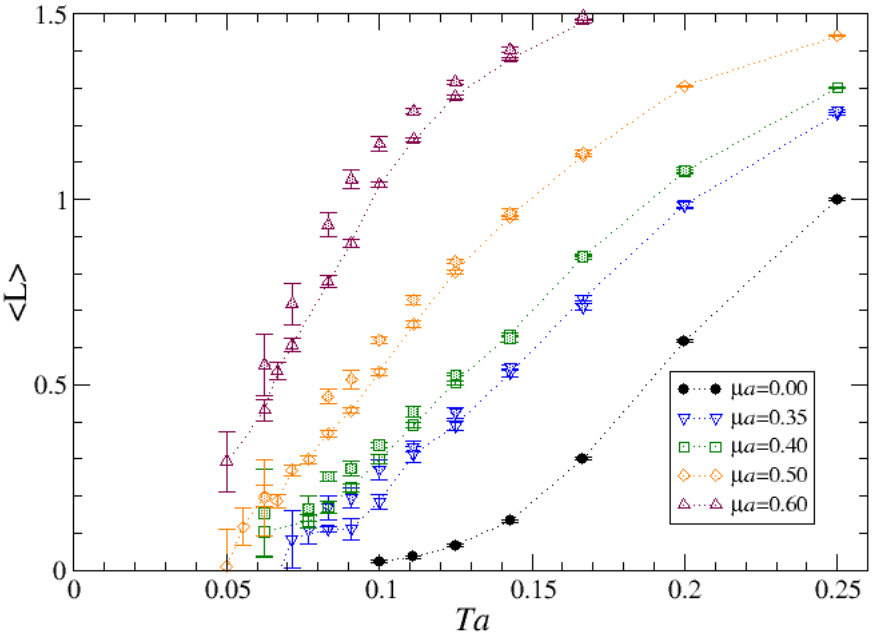

Figure 2.11: Polyakov loop versus temperature at five chemical potential values calculated on the coarser lattice with diquark source $ja = 0.04$ (open symbols) and $ja = 0.02$ (shaded symbols).

Where available we included the Polyakov loop values calculated using diquark source value $ja = 0.02$. We see that the lower diquark source leads to slightly higher Polyakov loop values, while preserving the qualitative behaviour.

We next calculated the Polyakov loop on the finer lattice. This time we did the renormalization according to the following scheme:

$$L_R\left(T = \frac{1}{4a}, \mu = 0\right) = 0.5. \tag{2.35}$$

In Fig. 2.12, we give the Polyakov loop with respect to temperature on the finer lattice. As temperature increases, we see that the Polyakov loop increases, suggesting deconfinement at high temperature. As on the coarser lattice, we observe that the temperature at which deconfinement occurs becomes smaller as the chemical potential increases.

In Fig. 2.13 we plot the Polyakov loop on the finer lattice with respect to chemical potential at fixed temperatures separately, in order to investigate the effect of the chemical potential on deconfinement. At all temperatures except for the lowest one, i.e., $1/N_\tau = 1/32a = 44.6$ MeV deconfinement is observed as the chemical potential increases. At the lowest temperature this observation is obstructed by the errors. At the lowest two temperatures (top plots) we do not observe diquark source dependence, while there seems to be a little diquark source dependence at the highest two temperatures (bottom plots).

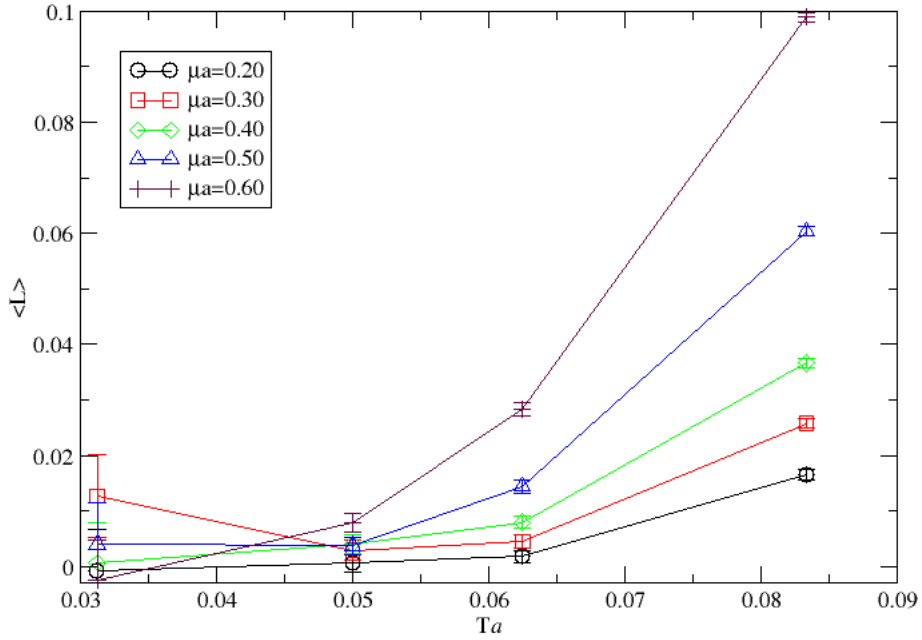

Figure 2.12: Polyakov loop vs temperature at five chemical potential values and with $ja = 0.03$ calculated on the finer $16 \times N_\tau$ lattices.

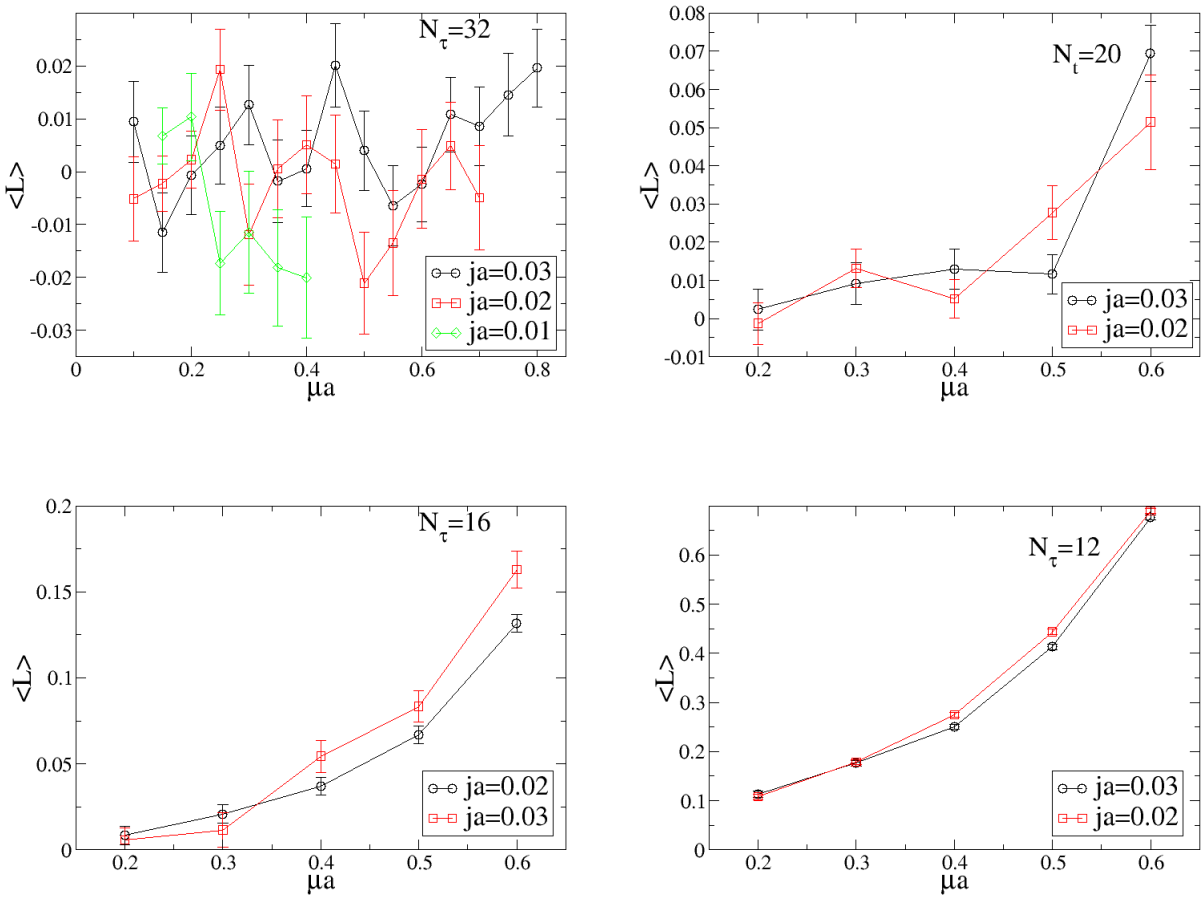

Figure 2.13: Polyakov loop versus chemical potential at four different temperatures calculated on the finer $16^3 \times N_\tau$ lattices.

2.6 Summary

We first investigated the static quark potential on the finer lattice and observed linear behaviour with respect to spatial Wilson loop separation. We set the scale on the finer lattice by means of the Regge trajectory and found the value $0.1380^{+0.0052}_{-0.0072}$ fm for lattice spacing.

We calculated the diquark condensate, which is the order parameter for the normal to superfluid phase transition, using different values for the diquark source both on the coarser and on the finer lattices. We plotted our results with respect to temperature and observed the phase transition as the temperature increases. We found out that the critical temperature, T_c, does not seem to depend on the chemical potential. However we could not determine the value for T_c as we did not have enough data. This is left to a future study.

We also plotted the diquark condensate divided by the squared values of the chemical potential with respect to the chemical potential, to investigate the formation of the Fermi surface, consistent with the BCS mechanism for the normal to superfluid phase transition. Our plots supported this hypothesis as we saw clear plateaux in the region between moderate to high densities.

In all diquark condensate calculations we used two or three different diquark source, j, values and made extrapolations to the $j \to 0$ limit. Our extrapolations were not ideal in that we obtained quite big values for χ^2/N_{dof}. To make better extrapolations we want to include more j values. This will also enable us to draw more precise conclusions about the phase transitions. This is also left to future studies.

Another quantity we studied was the quark number density. Our main finding was that the system behaves like a Stefan-Bolzmann gas at high densities.

Finally we studied deconfinement phase transition, whose order parameter is the expectation value of the Polyakov loop $\langle L \rangle$. On both the finer and the coarser lattice we found a smooth crossover to deconfined phase and we observed that an increase in the chemical potential lowers the critical temperature for deconfinement.

Chapter 3

Gluons

3.1 Gluon Propagator at $\mu = T = 0$

The gauge particles of QCD are the gluons, which mediate the strong interactions. An understanding of the infrared behaviour of the gluon propagator in the vacuum may shed light on the confinement phenomenon in QCD. There has been several claims on this behaviour using model-based studies such as DSE approach mentioned in Sec. 1.4. Starting from the early 1970's, two main hypotheses were proposed. The first one suggests an enhancement of the gluon propagator in the infrared momentum region. What is meant by enhancement is that if one considers one-gluon exchange at tree level, instead of behaving like $\propto 1/q^2$, the gluon propagator is enhanced so as to behave like $\propto 1/q^4$ at infrared momenta. The motivation is that the latter functional form, when Fourier-transformed gives a linear spatial behaviour which is consistent with the string-like binding potential of QCD. The second hypothesis supports a massive boson-like behaviour, which implies that the gluon propagator goes to a finite value at vanishing momentum.

Over the years, LQCD studies ruled out the first hypothesis and showed clearly that the gluon propagator goes to a finite value at vanishing momentum. One of first such studies is [51]. The interior plot of Fig. 3.1 demonstrates this finding. This figure is taken from our previous work [11]. It compares the gluon propagator on two volumes and it is seen that the volume effect is very small. To reduce the lattice artefacts in the ultraviolet momentum region, a weak cylinder cut was applied, which means keeping only momenta close to the diagonal $[1, 1, 1, 1]$.

At tree level and at zero chemical potential, the gluon propagator, $D(p)$, has a simple form:

$$D(p) = 1/p^2, \tag{3.1}$$

which, on the lattice becomes:

$$D(p) = 1/\sum_{\mu} \left(\frac{2}{a} \sin \frac{p_\mu a}{2} \right)^2 . \tag{3.2}$$

We therefore define the lattice momentum as

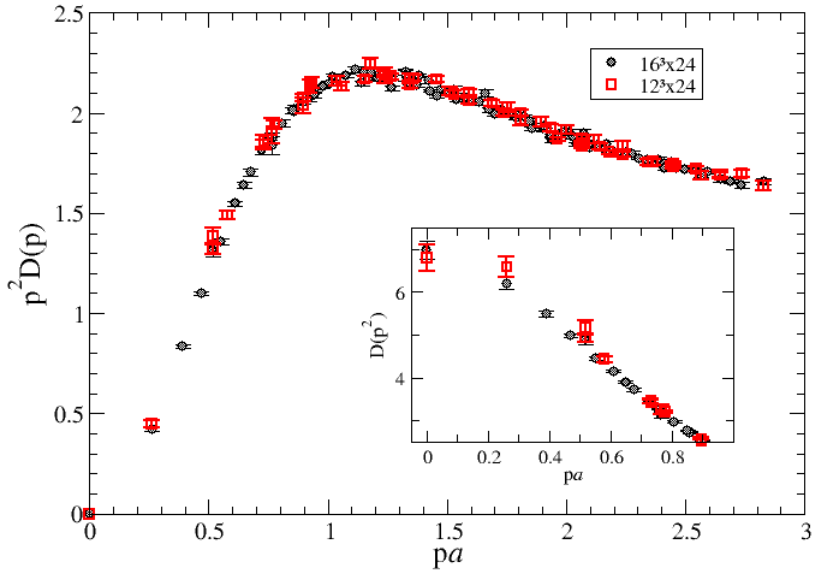

Figure 3.1: $p^2 D(p)$ computed at $\mu = 0$ on the coarser $16^3 \times 24$ and $12^3 \times 24$ lattices. The interior plot shows $D\left(p^2\right)$.

$$p_\mu \equiv \frac{2}{a} \sin \frac{p_\mu a}{2}, \tag{3.3}$$

and expect the numerical results for $p^2 D(p)$ to approach 1 at high momenta.

3.2 Gluon Propagator at Finite μ and T

The chemical potential breaks the manifest Lorentz symmetry. In this case the gluon propagator can be decomposed into chromoelectric and chromomagnetic form factors as follows:

$$D_{\mu\nu}(\mathbf{q}, q_4) = P^M_{\mu\nu} D_M\left(\mathbf{q}^2, q_4^2\right) + P^E_{\mu\nu} D_E\left(\mathbf{q}^2, q_4^2\right). \tag{3.4}$$

In eq. (3.4) $P^M_{\mu\nu}$ and $P^E_{\mu\nu}$ are projectors. The first one is spatially transverse while the second one is spatially longitudinal. Both of them are transverse in 4-dimensions in the Landau gauge which is used in this work. The Landau gauge condition has been imposed with a precision $|\partial_\mu A_\mu| < 10^{-10}$. This was done by maximizing the functional $F[g] = \sum_{\mu,x} \mathcal{R}\mathrm{Tr} U^g_\mu(x)$, where $U^g_\mu(x) = g(x) U_\mu(x) g^\dagger(x + \hat{\mu})$. In fact, this functional has more than one maximum which are referred to as *Gribov copies*. It would have been interesting to investigate the effect of Gribov copies but in this work we ignored them.

In order to compute D_M and D_E we write them in terms of $D_{\mu\nu}$, as shown below:

The gluon propagator can be decomposed as [52]

$$D_{\mu\nu}(p) = P^T_{\mu\nu}(p) D_T\left(\omega_p^2, \overrightarrow{p}^2\right) + P^L_{\mu\nu}(p) D_L\left(\omega_p^2, \overrightarrow{p}^2\right), \tag{3.5}$$

where

$$P^T_{\mu\nu}(p) = (1-\delta_{\mu 0})(1-\delta_{\nu 0})\left(\delta_{\mu\nu} - \frac{p_\mu p_\nu}{\overrightarrow{p}^2}\right), P^L_{\mu\nu}(p) = \Pi^\perp_{\mu\nu} - P^T_{\mu\nu}. \tag{3.6}$$

Here [53]:

$$Tr(D_{\mu\nu}) = \sum_{\mu=0}^{3} D_{\mu\mu} = \sum_{\mu=0}^{3} P^T_{\mu\mu} D_T + \sum_{\mu=0}^{3} P^L_{\mu\mu} D_L$$

$$\sum_{\mu=0}^{3} P^T_{\mu\mu} = (1-\delta_{\mu 0})(1-\delta_{\mu 0})\left(\delta_{\mu\mu} - \frac{p_\mu p_\mu}{\overrightarrow{p}^2}\right)$$

$$= \sum_{i=1}^{3}\left(\delta_{ii} - \frac{p_i p_i}{\overrightarrow{p}^2}\right) = 3 - \frac{\overrightarrow{p}^2}{\overrightarrow{p}^2} = 2$$

$$\sum_{\mu=0}^{3} P^L_{\mu\mu} = \sum_{\mu=0}^{3}\left(\delta_{\mu\mu} - \frac{p_\mu p_\mu}{p^2} - P^T_{\mu\mu}\right)$$

$$= \sum_{\mu=0}^{3}\delta_{\mu\mu} - \sum_{\mu=0}^{3}\frac{p_\mu p_\mu}{p^2} - \sum_{\mu=0}^{3} P^T_{\mu\mu}$$

$$= 4 - 1 - 2 = 1$$

$$\implies Tr(D_{\mu\nu}) = 2D_T + D_L. \tag{3.7}$$

On the other hand, adding the following linearly independent off-diagonal terms gives:

$$D_{12} + D_{13} + D_{23} = -\frac{(p_1p_2 + p_1p_3 + p_2p_3)}{\overrightarrow{p}^2} D_T + \frac{p_0^2(p_1p_2 + p_1p_3 + p_2p_3)}{\overrightarrow{p}^2 p^2} D_L$$

$$= \frac{(p_1p_2 + p_1p_3 + p_2p_3)}{\overrightarrow{p}^2 p^2}\left(-p^2 D_T + p_0^2 D_L\right). \tag{3.8}$$

We then have:

$$-p^2 D_T + p_0^2 D_L = \frac{\overrightarrow{p}^2 p^2 (D_{12} + D_{13} + D_{23})}{p_1p_2 + p_1p_3 + p_2p_3}. \tag{3.9}$$

From eq.(3.7) and eq.(3.9) we obtain the following expressions for the electric and magnetic form factors, in terms of the components of the gluon propagator:

$$D_T = \frac{p_0^2}{2p_0^2 + p^2} Tr(D_{\mu\nu}) - \frac{p^2\overrightarrow{p}^2}{(2p_0^2 + p^2)(p_1p_2 + p_1p_3 + p_2p_3)}(D_{12} + D_{13} + D_{23}), \tag{3.10}$$

$$D_L = \frac{p^2}{2p_0^2 + p^2} Tr(D_{\mu\nu}) + \frac{2p^2\overrightarrow{p}^2}{(2p_0^2 + p^2)(p_1p_2 + p_1p_3 + p_2p_3)}(D_{12} + D_{13} + D_{23}). \tag{3.11}$$

3.2.1 Results

We first present the (unrenormalised) numerical results for magnetic and electric components of the gluon propagator versus spatial momentum calculated on the finer $16^3 \times N_\tau$ lattices corresponding to four temperatures for two chemical potentials that are below ($\mu a = 0.2$) and above ($\mu a = 0.5$) the onset transition, with a diquark source of $ja = 0.03$ (Fig. 3.2). In all of the plots, we see an overall suppression in the propagator values as the momentum increases and they eventually go to zero. There is very little change with temperature for D_M at $\mu a = 0.2$,

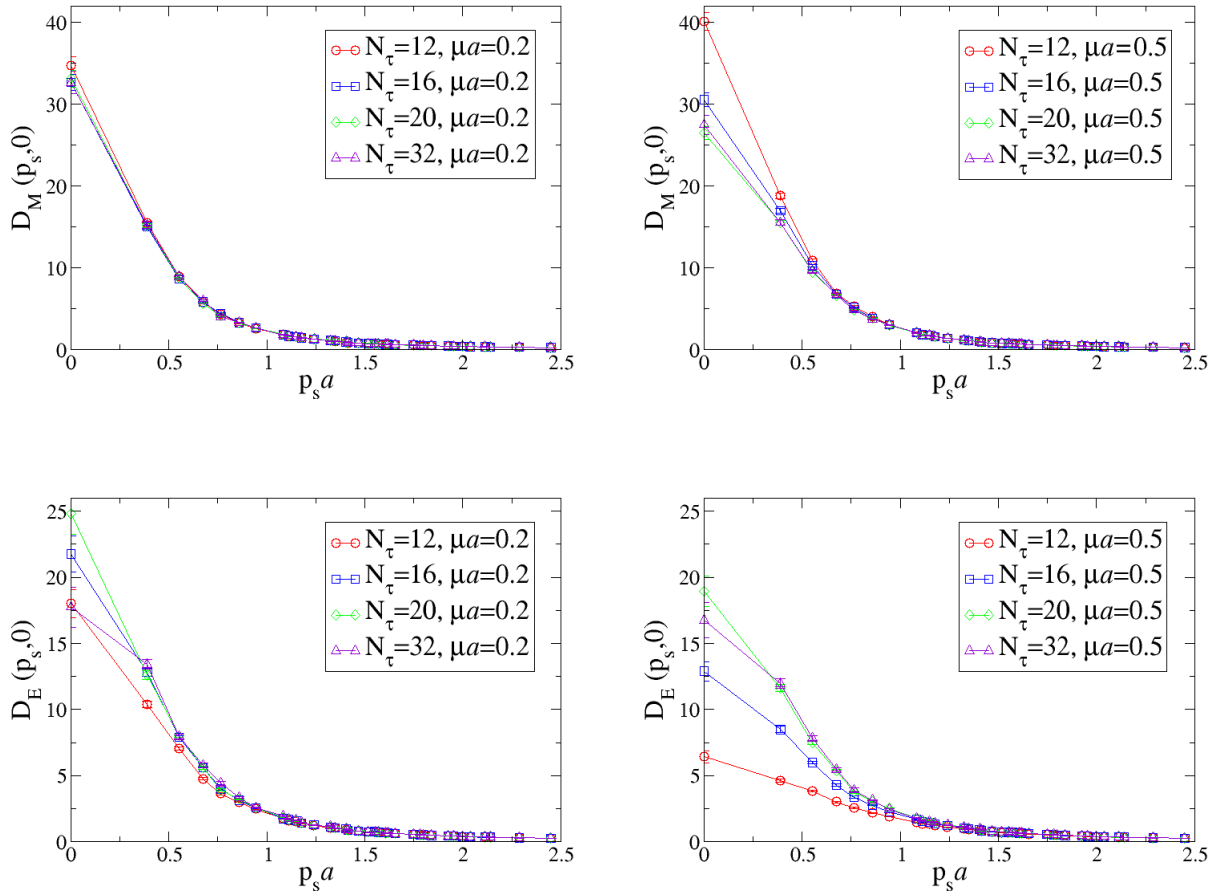

Figure 3.2: Thermal behaviour of the magnetic (top) and electric (bottom) components of the gluon propagator versus spatial momentum on the finer $16^3 \times N_\tau$ lattices, at $\mu a = 0.2$ (left) and $\mu a = 0.5$ (right). Data corresponding to the zeroth Matsubara modes are shown. The diquark source value is $ja = 0.03$.

which is below the onset transition. An increase to $\mu a = 0.5$ in the chemical potential separates the propagator values at different temperatures. For the electric component below the onset transition, the propagator values are not as close to each other as the magnetic component values are and the change with respect to temperature is more apparent. The change with respect to temperature becomes more dramatic as the chemical potential increases to $\mu a = 0.5$, which is above the onset transition. An overall conclusion is that the electric component is more affected by the change in temperature. This result is in agreement with the finding in our previous study on the coarser lattice [11], for $\mu a = 0.5$ and $ja = 0.04$, given in Fig. 3.3.

In Fig. 3.4 we compare the electric and magnetic components of the gluon propagator for two chemical potential values on the coarser and on the finer lattices, which we renormalised in the following way. At each p_s, the propagator values corresponding to the higher μ values are divided by the ones corresponding to the lowest μ. This gives a comparison of the pure medium effects at different p_s, disentangled from the lattice spacing and renormalisation effects. It is seen that the discrepancy is higher at low spatial momenta.

We next investigate the dependence of the gluon propagator on the chemical potential. In Fig.

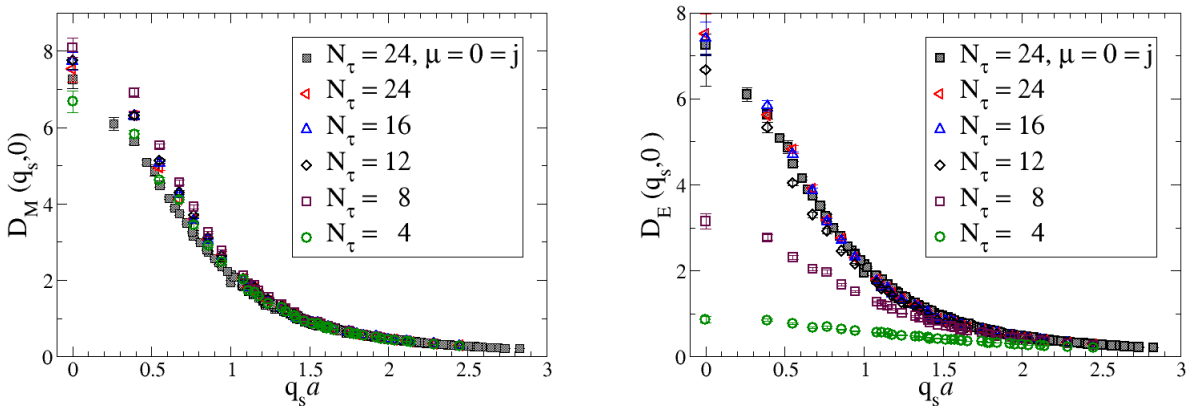

Figure 3.3: Comparison of the thermal behaviour of the magnetic (left) and electric (right) components of the gluon propagator on the coarser $16^3 \times N_\tau$ lattices, for the zeroth Matsubara mode. The chemical potential is $\mu a = 0.5$ and the diquark source is $ja = 0.04$.

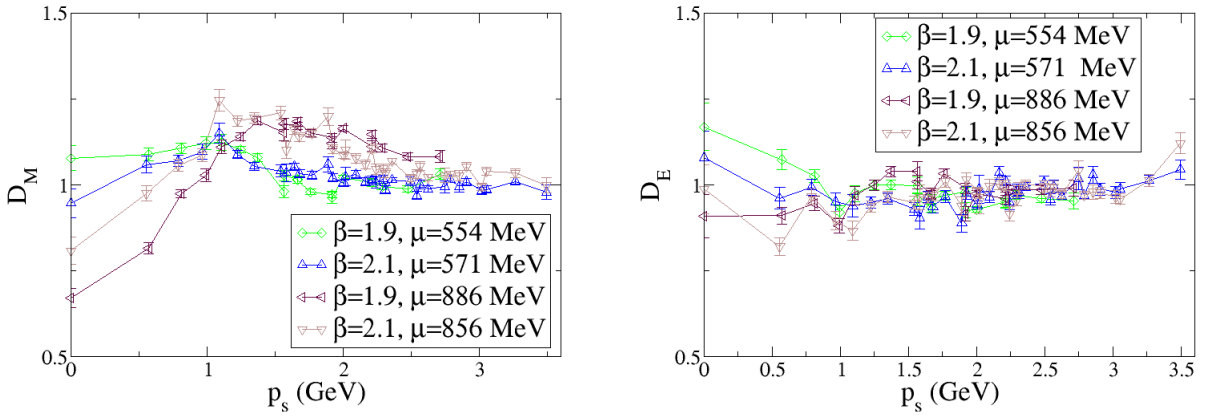

Figure 3.4: Magnetic (left) and electric (right) components of the gluon propagator versus spatial momentum on the finer $16^3 \times 20$ and on the coarser $12^3 \times 24$ lattices, for the zeroth Matsubara mode, divided by the values at $\mu \approx 280$ MeV.

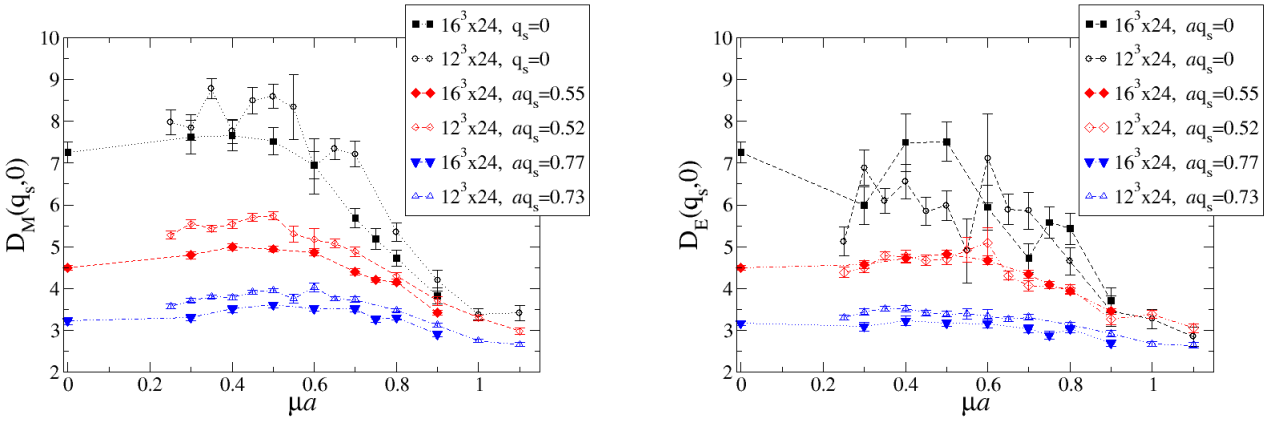

Figure 3.5: Magnetic (left) and electric (right) components of the gluon propagator versus chemical potential on the coarser lattice with two different spatial volumes and $N_\tau = 24$. The zeroth Matsubara modes and three selected spatial momenta are shown.

3.5 we give the numerical results on the coarser lattice with two different spatial volumes. This enables us to investigate the finite volume effects which was mentioned in Sec. 1.2 and we see that the volume dependence is not too large if one also takes into account the fact that part of the discrepancies are due to the fact that the spatial momenta on the different volumes do not match precisely. First, observe that where available, the magnetic and electric components at zero chemical potential have exactly the same values on the same lattice volumes, since there are no separate electric and magnetic components at zero density. There is a suppression on both volumes as the spatial momentum increases, which is consistent with the gluon propagator versus spatial momentum plots of Fig. 3.2 and Fig. 3.3. At every volume and momentum there is an enhancement at intermediary chemical potential, which corresponds to the superfluid and confined phase. They are all suppressed as the chemical potential increases, and at the highest chemical potential, which is in the deconfined phase region, they reach their closest values to each other in the whole chemical potential range.

In Fig. 3.6, we make a similar comparison to Fig. 3.5, this time on a single lattice volume of $16^3 \times 8$ which corresponds to a much higher temperature compared to that in Fig. 3.5. Again, there is an overall suppression in both the magnetic and the electric components as the spatial momentum increases. For the magnetic component at the lowest two momentum values selected, we observe an interesting peak over the intermediary chemical potential region, i.e., in the superfluid, confined phase. On the other hand, at the successive three higher momenta, the magnetic component is mildly enhanced towards high chemical potentials, which might be due to the increase in the temperature. We do not observe such an enhancement in the electric component and we see that the suppression towards high chemical potentials becomes clearer compared to Fig. 3.5. It is remarkable to observe that while in Fig. 3.5 both the electric and the magnetic component becomes suppressed at all selected spatial momenta, in Fig. 3.6 this is observed only for the electric component. This shows that the qualitative behaviour of the magnetic component in the dense, deconfined phase is more sensitive to the temperature increase. This is in contradiction with our previous statement that the electric component is more affected by the change in temperature.

In Fig. 3.7 we compare the behaviour of the two components of the gluon propagator with

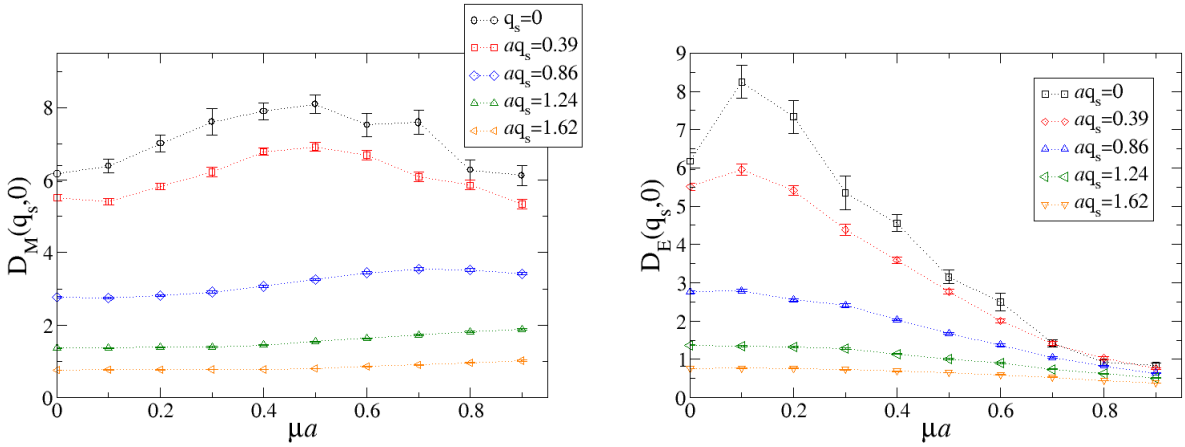

Figure 3.6: Magnetic (left) and electric (right) components of the gluon propagator versus chemical potential on the coarser $16^3 \times 8$ lattice. The zeroth Matsubara modes and three selected spatial momenta are shown.

respect to chemical potential on the finer and on the coarser lattices. To enable the comparison, we expressed all physical quantities in physical units. Note that the selected momenta on the two lattices do not match precisely although they are quite close. Firstly, we observe a general qualitative agreement on both lattices. We see that for both components, the propagator values on the finer lattice are higher with respect to the values on the coarser lattice, i.e., we still have significant lattice spacing effects especially for the magnetic component, but this separation between the curves becomes smaller as the spatial momentum increases.

In order to place the computed results of the gluon propagator on a more quantitative ground and to understand its qualitative behaviour better, one tries to fit the propagator data to some proposed functions. In our work we did this using the model function:

$$D^{\text{fit}}_{M/E}\left(q^2\right) = \frac{\Lambda^2}{\left(q^2+\Lambda^2\right)^2}\left(q^2+\Lambda^2 a_{M/E}\right)^{-b_{M/E}}, \tag{3.12}$$

which was inspired by [52].

The normalization constant Λ in eq. (3.12) has been calculated in the vacuum, i.e., for $\mu = j = 0$. We found $\Lambda a = 0.999(3)$ on the coarser, $16^3 \times 24$ lattice and $\Lambda a = 0.613(1)$ on the finer, $16^3 \times 32$ lattice. It is assumed to be independent of temperature and chemical potential. In Fig. 3.8 we give the μ dependence of the fit parameters a and b of eq. (3.12) both for the magnetic and the electric components on both lattices. Both parameters change as temperature and chemical potential change. On the coarser lattice we observe a tendency in both parameters to decrease as the chemical potential becomes high at all temperatures. However, on the finer lattice, we see a similar behaviour only for the electric-component-parameters at the highest two temperatures.

Fig. 3.9 shows the thermal behaviour of the fit parameters a and b on the finer lattice at $\mu a = 0.4 \approx 570.8\,\text{MeV}$ and $ja = 0.03 \approx 42.8\,\text{MeV}$. Fig. 3.10 shows the same on the coarser lattice at $\mu a = 0.5 \approx 553.5\,\text{MeV}$ and $ja = 0.04 \approx 44.3\,\text{MeV}$. On both lattices the parameters reach to a stable value towards low temperatures, i.e., as the temporal lattice size increases. On both lattices a_E and b_E shows a decrease as the temperature increases. This behaviour is the

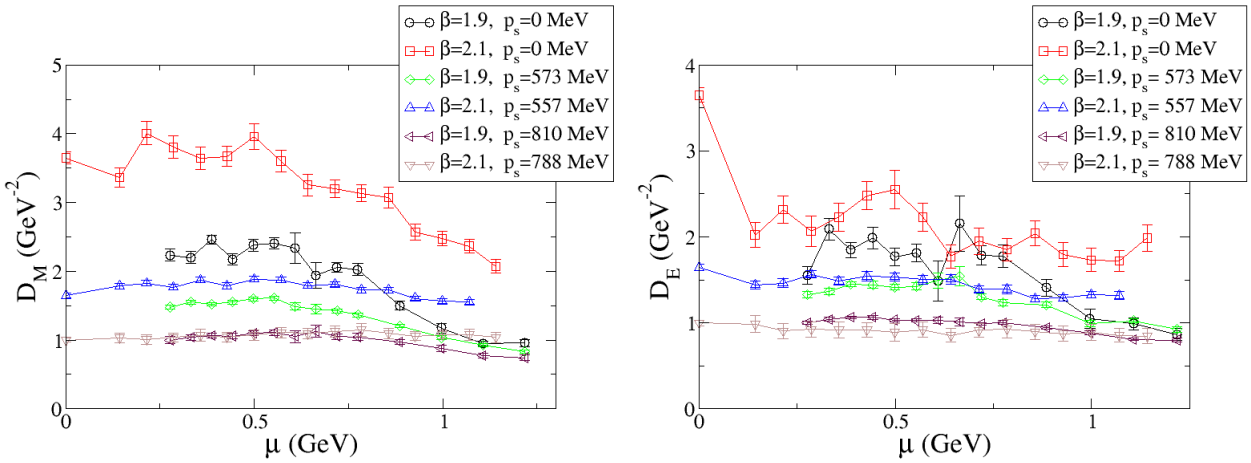

Figure 3.7: Magnetic (left) and electric (right) components of the gluon propagator versus chemical potential on the finer $16^3 \times 20$ ($\beta = 2.1$) and on the coarser $12^3 \times 24$ ($\beta = 1.9$) lattices, for the zeroth Matsubara mode.

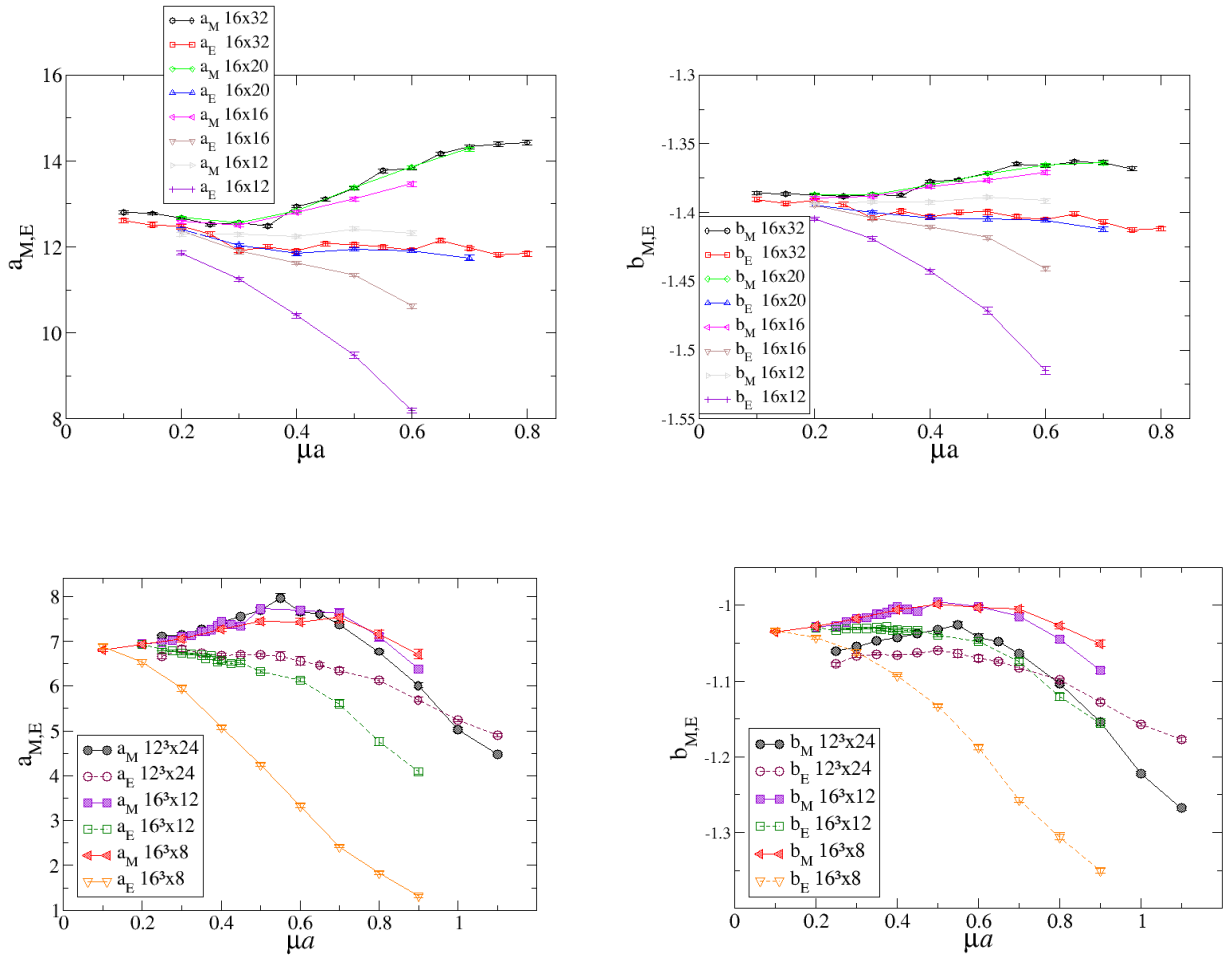

Figure 3.8: Fit parameters a (left) and b (right) of the magnetic and the electric components, with respect to chemical potential on the finer (top) and on the coarser (bottom) lattices.

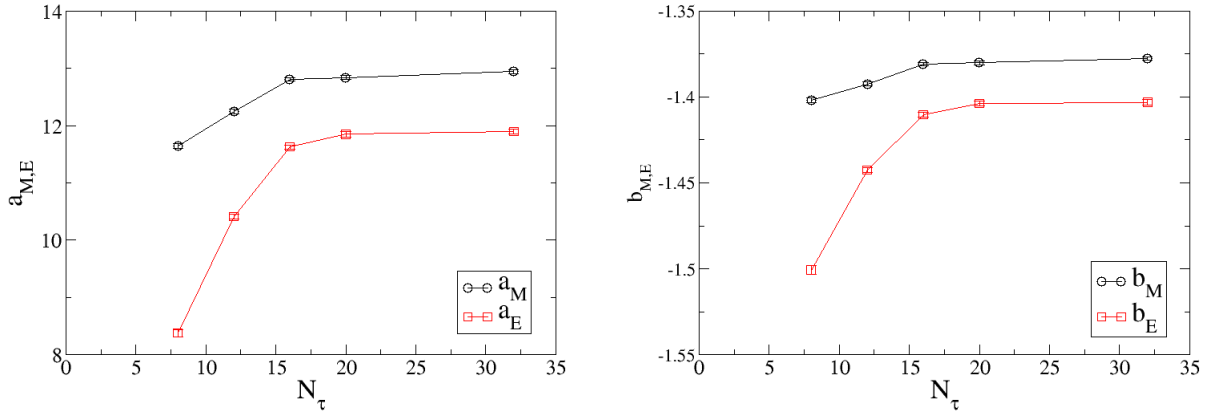

Figure 3.9: Thermal behaviour of the fit parameters a (left) and b (right) on the finer lattice at $\mu a = 0.4 \approx 570.8\,\mathrm{MeV}$ and $ja = 0.03 \approx 42.8\,\mathrm{MeV}$.

same also for a_M and b_M on the finer lattice, whereas it appears to change with temperature on the coarser lattice.

3.3 Summary

We first presented our result for the gluon propagator at zero chemical potential and zero temperature, calculated on the coarser lattice. Our plot supports a massive boson-like behaviour of the propagator, rather than enhancement in the infrared momentum region, in line with other studies.

At finite potential the gluon propagator splits into spatially transverse (chromomagnetic) and spatially longitudinal (chromoelectric) components and we plotted them both with respect to spatial momentum and chemical potential as well as investigating their thermal behaviour.

In general we observed suppression of these components with increasing chemical potential. An exception is the magnetic component on the coarser $16^3 \times 8$ lattice, where we observed an interesting peak around the superfluid confined phase at two lowest spatial momenta, and even a slight increase in the deconfined phase at the highest three spatial momenta (Fig. 3.6).

Where data were available, we compared the gluon propagator on the finer and the coarser lattice. We found that the qualitative behaviour remains the same on different lattices, the quantitative discrepancy getting smaller at higher spatial momenta.

We also investigated the response of the magnetic and the electric components to an increase in the temperature and saw that the electric component shows a dramatic suppression at high temperature, while the magnetic component is not as much sensitive, although it does show a little suppression in the infrared momentum region.

We finally tried to fit our data for the two components of the gluon propagator to a model function given in eq. (3.12), for a better understanding of their functional behaviour. There are three input parameters Λ, $a_{M,E}$, $b_{M,E}$ for the magnetic and the electric components separately. Λ is assumed to be independent of the temperature and the chemical potential and we investigated the effects of the medium and temperature change on the remaining two parameters.

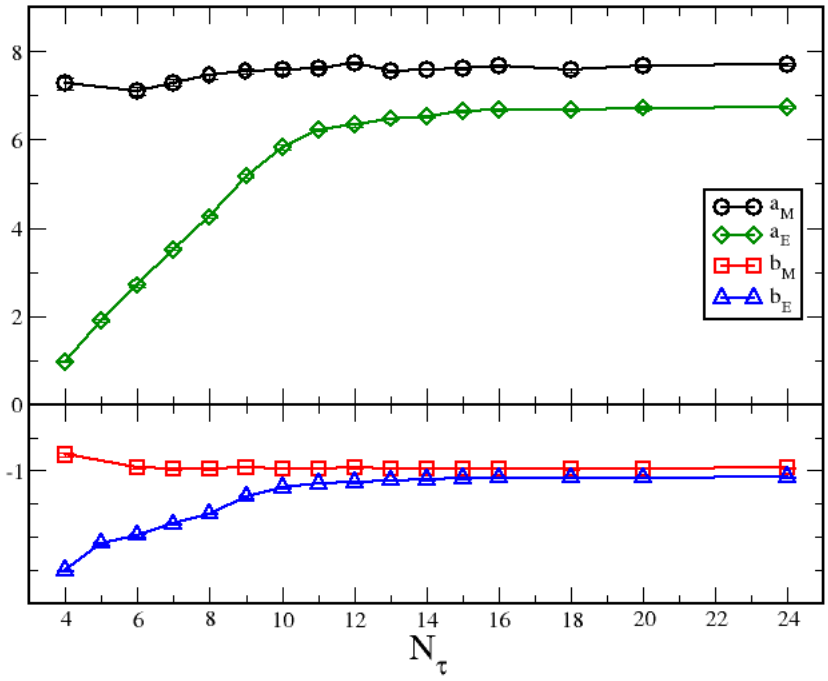

Figure 3.10: Thermal behaviour of the fit parameters a and b on the coarser lattice at $\mu a = 0.5 \approx 553.5\,\mathrm{MeV}$ and $ja = 0.04 \approx 44.3\,\mathrm{MeV}$.

Chapter 4

Propagation of Quarks in the Presence of Chemical Potential

4.1 Introduction

As a correlation function of elementary degrees of freedom in the Lagrangian, the quark propagator is an important fundamental quantity of QCD. It gives information about the behaviour of quarks in dense medium. In particular, the scalar part of the inverse quark propagator possesses information about the dynamical mass of quarks and one needs to study it in order to understand chiral symmetry breaking. In the presence of anomalous propagation, it encodes information about the Fermi gap and formation of diquark pairs that was mentioned in Sec. 2.3. On the other hand it plays an important role in functional methods like Dyson-Schwinger Equations and Functional Renormalization Group methods that were mentioned in Sec. 1.4. One also needs to calculate the quark propagator in hadron spectroscopy.

4.2 Form Factors

As we do not have analytic expressions for the propagators in medium, it is easier to investigate them by writing them in the most general form that the symmetry arguments allow and employing some coefficient functions called *form factors*, which will be denoted by S_a, S_b, S_c and S_d in the following. The main result from Appendix B is that such a form can include terms with at most one gamma matrix factor if the Lagrangian and the ground state are to have Lorentz, parity and time-reversal invariance. This rules out a possible term that would be like $\mathbf{p}\!\!\!/\gamma_4 S_d(p)$. We then have:

$$S(p) = S_b(p) + \mathrm{i}p^\nu S_{a,c}(p)\gamma_\nu, \tag{4.1}$$

which can be rewritten as:

$$S(p) = S_b(p) + \mathrm{i}p^k S_a(p)\gamma_k + \mathrm{i}p_4 S_c(p)\gamma_4. \tag{4.2}$$

The reason to separate the second term in eq. (4.1) will become clear when we introduce finite

chemical potential in our theory. The chemical potential would affect the temporal component of the momentum, that is, the energy. We write:

$$S(p) = S_b(p) + \mathrm{i}p^k S_a(p)\gamma_k + \mathrm{i}(p_4 - \mathrm{i}\mu)S_c(p)\gamma_4. \tag{4.3}$$

With the definition, $\omega = p_4 - \mathrm{i}\mu$ this becomes:

$$S(p) = S_b(p) + \mathrm{i}p^k S_a(p)\gamma_k + \mathrm{i}\omega S_c(p)\gamma_4. \tag{4.4}$$

This is the form of the propagator we will use for the normal propagation and we will be interested in computing the three form factors $S_a(p)$, $S_b(p)$ and $S_c(p)$, and extracting information about the quark propagator in dense medium by interpreting the results.

4.3 Anomalous Quark Propagation

Apart from the normal propagation of quarks, the presence of the chemical potential leads to the phenomenon that is called *anomalous quark propagation*, in which a quark at some point in the space-time propagates into an antiquark at another point in space-time. (More adequately, rather than a quark turning into an antiquark, a diquark turns into an anti-diquark.)

The anomalous quark propagator is given by the expression:

$$\langle \psi(x)\psi(x') \rangle . \tag{4.5}$$

If it was the normal propagator given by $\langle \psi(x)\bar{\psi}(x') \rangle$, we would interpret it as the probability density of finding a quark created at space-time point x', at space-time point x. In contrast, the anomalous propagator is to be interpreted as the probability density of finding a quark at point x' as an *antiquark* at point x. This is clearly inconsistent with the conservation of baryon number and therefore can not be observed in a vacuum with zero chemical potential.

If, however, there is a non-zero chemical potential, diquark condensation may occur as described in Sec. 2.3 and the baryon number is no longer conserved. This is because, a non-zero expectation value of the diquark condensate breaks the global $U(1)$ symmetry spontaneously. This opens the door for anomalous quark propagation which is believed to occur inside the compact stars mentioned in Sec. 1.1.

Anomalous propagation indeed occurs in real superconductors. The relevant particles and antiparticles are then electrons and holes. Analogues of diquark condensate are Cooper pairs.

4.4 Quark Propagator and Form Factors on the Lattice

The Wilson fermion matrix, M, in the presence of a chemical potential, $\mu \neq 0$, and in the absence of diquark source, $j = 0$, in position space is given by:

$$M(\mu) = \delta_{xy} - \kappa \sum_{\nu} \left[(\mathbf{1} - \gamma_\nu)\, \mathrm{e}^{\mu\delta_{\nu 0}} U_\nu(x)\, \delta_{y,x+\hat{\nu}} + (\mathbf{1} + \gamma_\nu)\, \mathrm{e}^{-\mu\delta_{\nu 0}} U_\nu^\dagger(y)\, \delta_{y,x-\hat{\nu}} \right]. \tag{4.6}$$

Here $U(x)$ is the gauge field, and $U(x) \neq \mathbf{1}$ means that the fermion matrix expression is for

the interacting case. For free fermions ($U(x) = \mathbf{1}$), the Fourier transform of $M(\mu)$ gives the Wilson fermion matrix in momentum space:

$$M(p) = \frac{\mathrm{i}}{a}\sum_{j=1}^{3}\gamma_j \sin(ap_j) + \frac{\mathrm{i}}{a}\gamma_4 \sin(a\omega) + m_0 + \frac{1}{a}\sum_{j=1}^{3}\left[\mathbf{1} - \cos(p_j a)\right] + \frac{1}{a}\left[\mathbf{1} - \cos(\omega a)\right], \quad (4.7)$$

where $\omega = p_4 - \mathrm{i}\mu$ (see Appendix A). Note that μ is absorbed into ω.

In the continuum, the inverse quark propagator can be written in terms of the form factors A, B, C and D:

$$M(p) = \mathrm{i}\not{p}A(p) + B(p) + \mathrm{i}\omega\gamma_4 C(p) + \not{p}\gamma_4 D(p). \quad (4.8)$$

Similarly, the quark propagator, which is the inverse of the Wilson fermion matrix, can be written in terms of form factors:

$$S(p) = M^{-1}(p) = \mathrm{i}\not{p}S_a(p) + S_b(p) + \mathrm{i}\omega\gamma_4 S_c(p) + \not{p}\gamma_4 S_d(p). \quad (4.9)$$

These form factors can be written in terms of the traces of the propagator or its multiplication with various terms:

$$S_a = \frac{\mathrm{i}}{4K^2}\mathrm{Tr}\left[\not{K}S(p)\right], \quad S_b = \frac{1}{4}\mathrm{Tr}\left[S(p)\right], \quad S_c = \frac{\mathrm{i}}{4K_4}\mathrm{Tr}\left[\gamma_4 S(p)\right]. \quad (4.10)$$

In eq. (4.10) K is the momentum on the lattice:

$$K = \frac{1}{a}\sum_{\mu=1}^{4}\sin(ap_\mu). \quad (4.11)$$

We also have:

$$A = C = -\frac{S_a}{\mathbf{p}^2 S_a^2 + S_b^2 + \omega^2 S_c^2}, \quad (4.12)$$

$$B = \frac{S_b}{\mathbf{p}^2 S_a^2 + S_b^2 + \omega^2 S_c}. \quad (4.13)$$

4.5 The Gor'kov Propagator

If a non-zero diquark source is introduced, the Wilson fermion matrix becomes:

$$\mathcal{M} = \begin{pmatrix} M(\mu) & -\frac{j}{2}C\gamma_5\tau_2 \\ \frac{j}{2}C\gamma_5\tau_2 & C\tau_2 M(-\mu)C\tau_2 \end{pmatrix}. \quad (4.14)$$

This expression is known as the *Gor'kov matrix* and is in the position space, and $M(\mu)$ is the fermion matrix when there is no diquark source term. Inverse of this matrix is the *Gor'kov propagator*:

$$G = \mathcal{M}^{-1} \equiv \begin{pmatrix} S & A \\ \bar{A} & \bar{S} \end{pmatrix}. \tag{4.15}$$

The diagonal block components, S and $\bar{S}$, govern the normal propagation of quarks while the off-diagonal block components, A and $\bar{A}$, are responsible for the anomalous propagation of quarks.

The Gor'kov propagator has the following symmetries

$$K\mathcal{G}K^{-1} = \begin{pmatrix} S^* & -A^* \\ -\bar{A}^* & \bar{S}^* \end{pmatrix}, \tag{4.16}$$

where

$$K = C\gamma_5\tau_2. \tag{4.17}$$

In eq. (4.17) C is the charge conjugation operator and τ_2 is the Pauli matrix that acts in the colour space. One has the following relations for the block components:

$$\bar{S}(x,y) = -S(y,x)^T, \quad A(x,y) = A(y,x)^T, \quad \bar{A}(x,y) = \bar{A}(y,x)^T. \tag{4.18}$$

The block components of the Gor'kov propagator are themselves quark propagators. Equation (4.4) was written based on the parity and rotational symmetries of the theory. Introduction of a diquark source breaks time reversal and charge conjugation symmetries but leaves the parity and rotational symmetries unchanged (introduction of a chemical potential breaks the Lorentz symmetry in addition to above). Therefore the block components of the Gor'kov propagator can be written in the same way as in equation (4.4):

$$S(p) = \mathrm{i}\not{\mathbf{p}} S_a(p) + S_b(p) + \mathrm{i}\omega\gamma_4 S_c(p), \tag{4.19}$$

for the normal propagation and,

$$A(p) = \mathrm{i}\not{\mathbf{p}} A_a(p) + A_b(p) + \mathrm{i}\omega\gamma_4 A_c(p) + \not{\mathbf{p}}\gamma_4 A_d(p), \tag{4.20}$$

for the anomalous propagation. Note that in eq. (4.20) we preserved the term $\not{\mathbf{p}}\gamma_4 A_d(p)$ as we could not show that the proof that $S_d = 0$ for the normal part carries through for the corresponding anomalous part (see Appendix B).

4.6 Form Factors of the Normal Propagation

We first present the numerical results for the form factors of the normal propagation.

- Form factor S_b : It is the scalar part of the normal propagator and is related to the dynamical mass. The real part of S_b is shown for the zeroth Matsubara mode at four different temperatures in Fig. 4.1. The imaginary parts have been found to vanish.

The change in the behaviour of the form factor due to the increase in the chemical potential and the temperature occurs at low spatial momenta. This should be interpreted to be due to

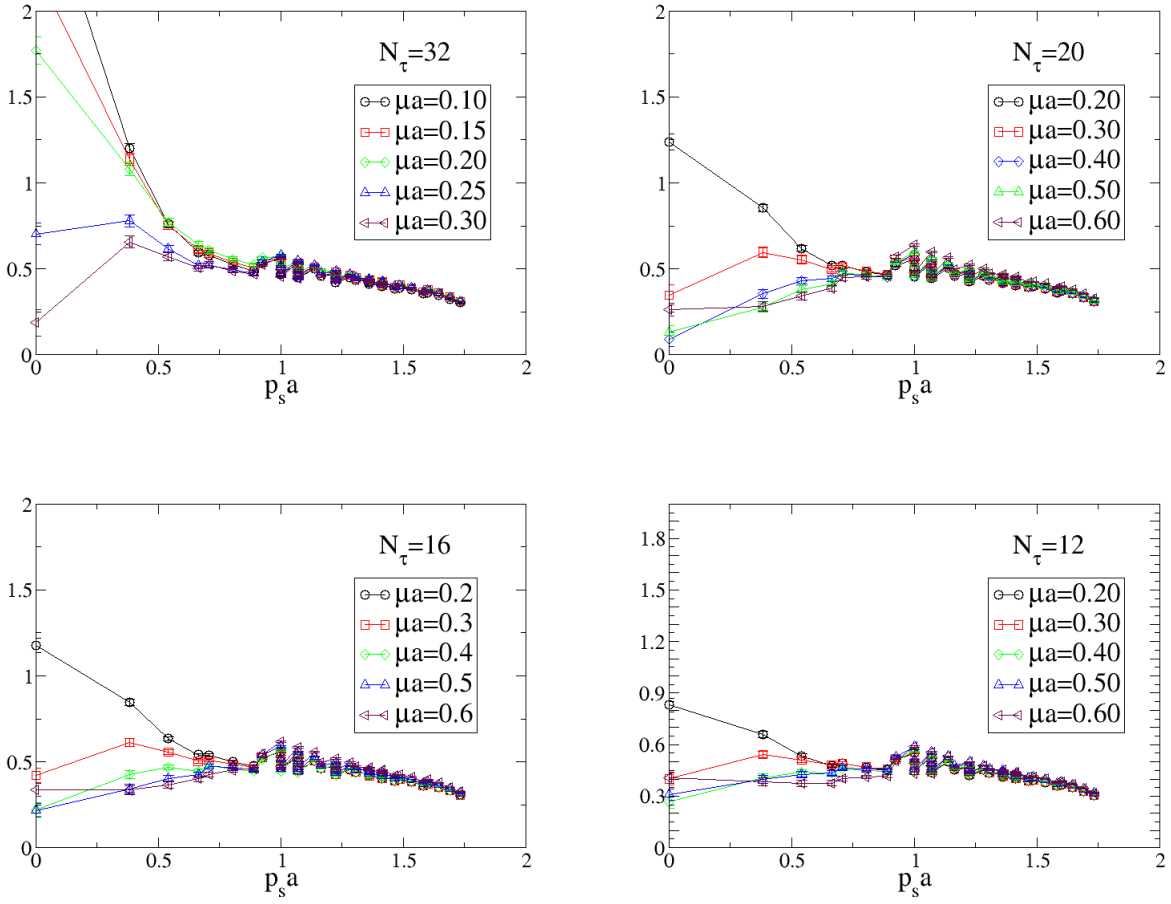

Figure 4.1: Real parts of the S_b form factors versus spatial momentum on the finer $16^3 \times N_\tau$ lattices for the lowest Matsubara mode.

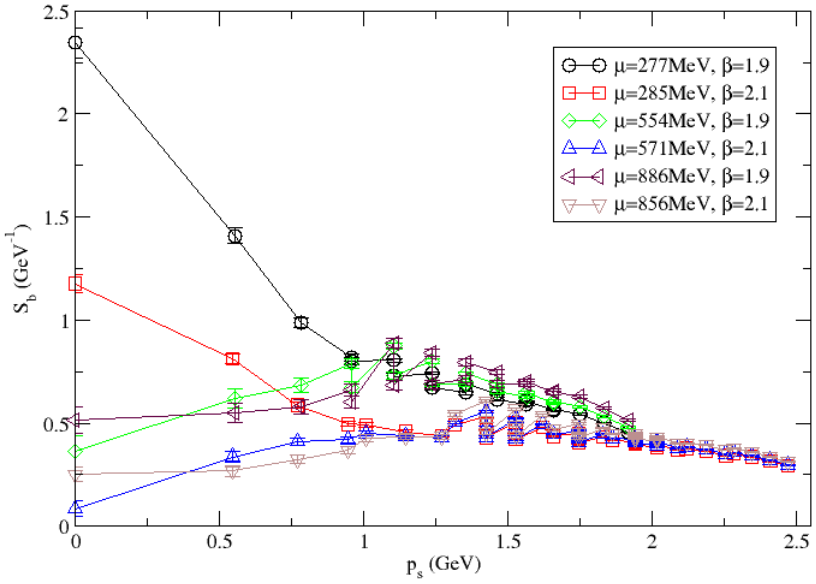

Figure 4.2: Real parts of the S_b form factors versus spatial momentum on the finer $16^3 \times 20$ ($ja = 0.03 \equiv 42.8$ MeV) and on the coarser $12^3 \times 24$ ($ja = 0.04 \equiv 44.3$ MeV) lattices. The lowest Matsubara mode shown. This is equivalent to 224 MeV on the finer and to 145 MeV on the coarser lattice.

asymptotic freedom at high spatial momenta. The suppression of the real part of the form factor S_b towards high chemical potentials can be interpreted as a rotation of the chiral condensate to diquark condensate, i.e., superfluid phase transition. It is further observed that up to $\mu = 0.20$, i.e., below the onset transition, this suppression increases with the temperature. Quark mass, which is related to S_b, can be thought as a measure of the breaking of chiral symmetry. Therefore this suppression signals chiral symmetry restoration. Note the multi-valuedness at some momenta, which we interpret to be due to lattice artefacts: we are working on a hypercubic lattice and therefore the $O(3)$ symmetry is violated.

In Fig. 4.2 we compare the S_b form factors on the coarser lattice, with those given in Fig. 4.1. Below the onset transition (319 MeV for β=2.1 and 359 MeV for β=1.9) and at zero momentum, the form factor value is much larger on the coarser lattice. Above the onset transition, the form factor values are still higher on the coarser lattice, while the discrepancy becomes smaller as the chemical potential increases. At all chemical potentials the discrepancies between the finer and the coarser lattices get smaller as the spatial momentum increases, which we interpret to be due to the asymptotic freedom. In all comparisons, it should be kept in mind that the physical values of the Matsubara mode used are different on the fine and the coarse lattices (224 MeV on the finer and 145 MeV on the coarser lattice), which is a source for discrepancies by itself. Like in Fig. 4.1, suppression due to normal to superfluid phase transition is observed as the chemical potential increases.

- Form factor S_a : This is the spatial vector-type form factor of the normal propagator, related to wave function renormalization. In the simulations, its imaginary parts have

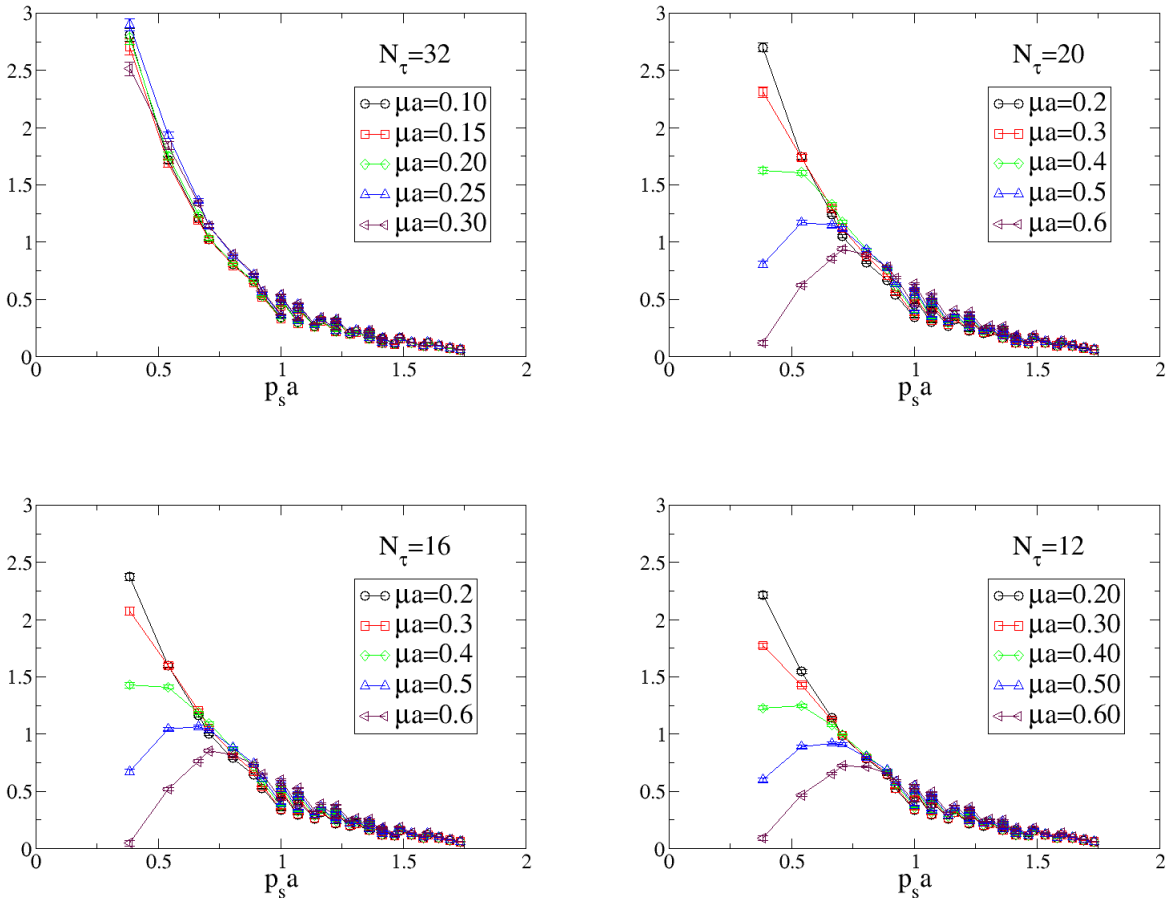

Figure 4.3: Real parts of the S_a form factors versus spatial momentum on the finer $16^3 \times N_\tau$ lattices for the lowest Matsubara mode.

been found to be consistent with zero. Plots for the real parts for different temperatures and chemical potentials are given in Fig. 4.3.

As the temperature increases at fixed chemical potential, it is seen that the form factor is only slightly suppressed and neither the shape of the plots, nor the spatial momenta at which the peaks occur change. However, at every temperature, as the chemical potential increases, the form factor is dramatically suppressed and the peak values are shifted towards higher spatial momenta. These observations suggest that this form factor, while being substantially affected by the onset transition and normal to superfluid transition, is not too much affected by the chiral symmetry restoration which is signalled by the behaviour of the S_b form factor with respect to increasing temperature.

In Fig. 4.4 we compare the S_a form factors for two chemical potential values on the coarser lattice with those given in Fig. 4.3. We see that while the shape of the form factors are similar, there are discrepancies in the magnitudes. This must be mainly due to the difference in the physical temporal momenta, which reads 145 MeV on the coarser and 224 MeV on the finer lattice. Note also that although the physical μ values are quite close, they are not exactly the same on both lattices. Another contribution to the differences in the magnitudes may be large

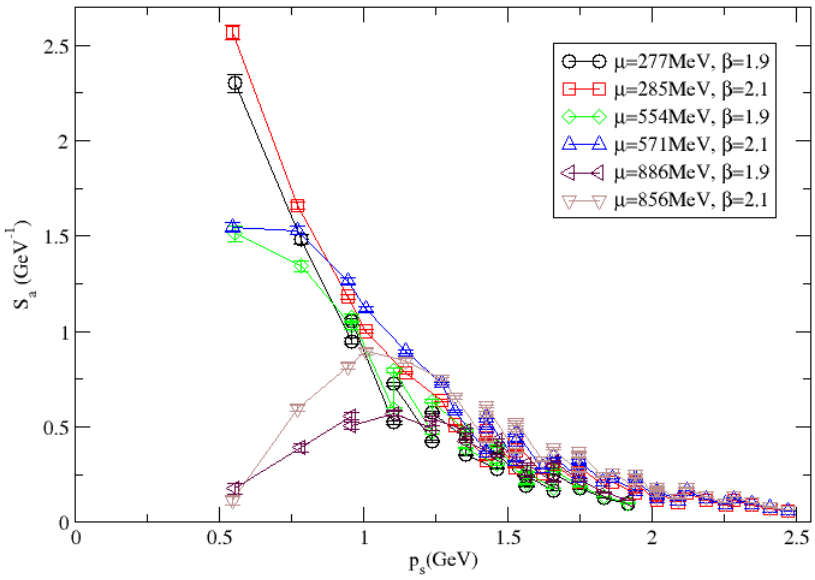

Figure 4.4: Real parts of the S_a form factors versus spatial momentum on the finer $16^3 \times 20$ ($ja = 0.03 \equiv 42.8$ MeV) and on the coarser $12^3 \times 24$ ($ja = 0.04 \equiv 44.3$ MeV) lattices. The lowest Matsubara mode shown. This is equivalent to 224 MeV on the finer and to 145 MeV on the coarser lattice.

cutoff effects.

- Form factor S_c : This the temporal vector part of the normal propagator. The real part of S_c is shown at various chemical potentials and at four different temperatures in Fig. 4.5. The imaginary parts have been found to vanish.

The behaviour of the zeroth Matsubara mode is especially interesting in that it goes to negative values at intermediary spatial momenta and asymptoticaly approaches to zero from below at higher spatial momenta. This is an indicator of a Fermi gap and the low momentum value at which it crosses zero can be used to determine the Fermi energy.

In Fig. 4.6 we compare the S_c form factors for two chemical potential values on the coarser lattice with those given in Fig. 4.5. We observe a clear consistency at high spatial momenta. At low momenta the form factor values are higher on the coarser lattice.

- Form factor S_d : This is the tensoral form factor of normal propagation. In [48] it is shown analytically that this form factor vanishes and this is confirmed in our simulations. In Appendix B, we reproduce the results of [48] and show that the normal form factor can have at most one gamma matrix factor so that the form factor S_d vanishes.

4.7 Form Factors of the Anomalous Propagation

We now present the numerical results for the form factors of the anomalous propagation.

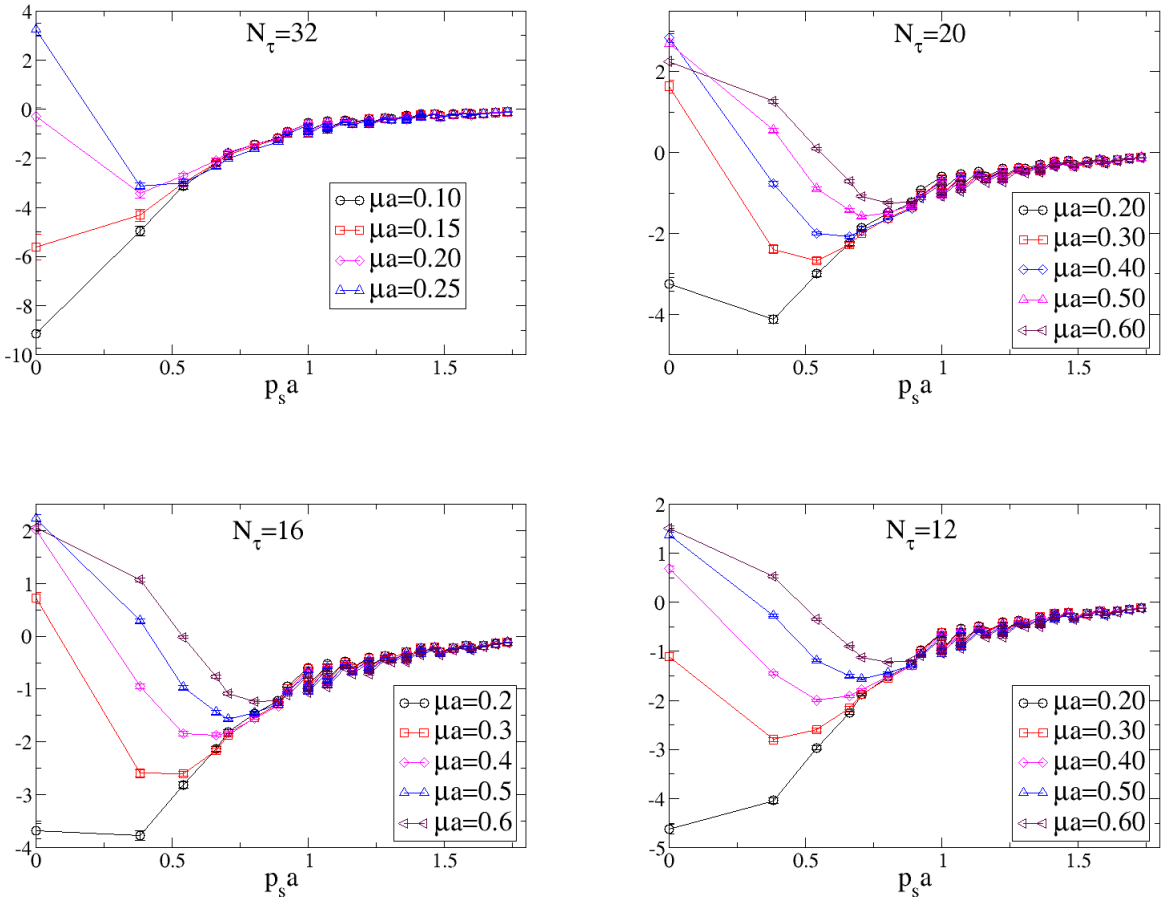

Figure 4.5: Real parts of the S_c form factors versus spatial momentum on the finer $16^3 \times N_\tau$ lattices for the lowest Matsubara mode.

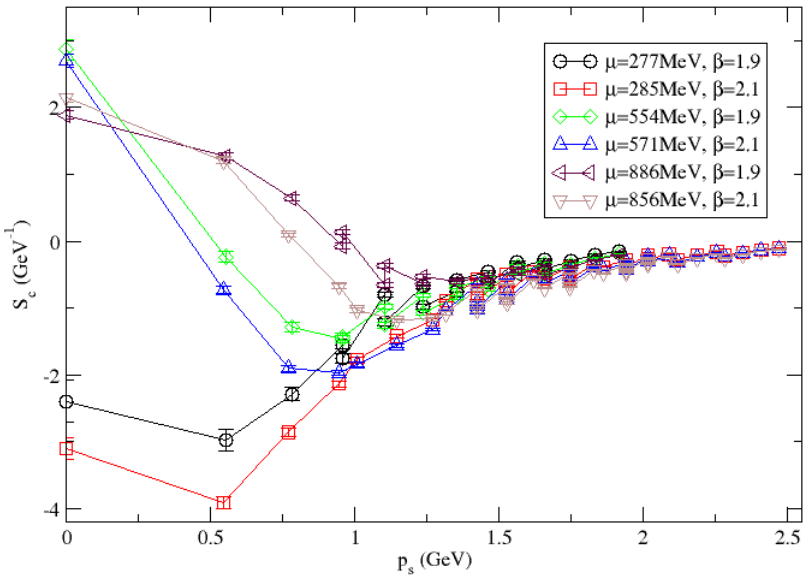

Figure 4.6: Real parts of the S_c form factors versus spatial momentum on the finer $16^3 \times 20$ ($ja = 0.03 \equiv 42.8$ MeV) and on the coarser $12^3 \times 24$ ($ja = 0.04 \equiv 44.3$ MeV) lattices. The lowest Matsubara mode shown. This is equivalent to 224 MeV on the finer and to 145 MeV on the coarser lattice.

- Form Factor A_a : This is the spatial vector-type form factor of the anomalous propagator. It has been found to vanish in our simulations.
- Form Factor A_b : This is the scalar form factor of the anomalous propagation. The imaginary parts have been found to vanish. The real parts are shown at various chemical potentials and at four different temperatures in Fig. 4.7.

We see a general enhancement in the negative direction with increasing chemical potential. This should account for the suppression of the amplitude in the normal propagation as the chemical potential increases, which is due to the rotation of the chiral condensate to the diquark condensate.

In Fig. 4.8 we compare the A_b form factors for two chemical potential values on the coarser lattice with those given in Fig. 4.7. We observe that while the behaviour of the form factor on the two lattices are consistent, the values on the coarser lattice are higher in the negative direction. The discrepancies between the two lattices become smaller as the chemical potential increases as well as towards higher spatial momenta.

- Form Factor A_c : This is the temporal vector-type form factor of the anomalous propagation. The imaginary parts have been found to vanish. The real parts are shown at various chemical potentials and at four different temperatures in Fig. 4.9. We see that at all chemical potentials and temperatures, the form factor converges to zero towards high spatial momenta. This convergence occurs from negative values at low chemical potentials and from positive values at high chemical potentials. We observe an overall suppression

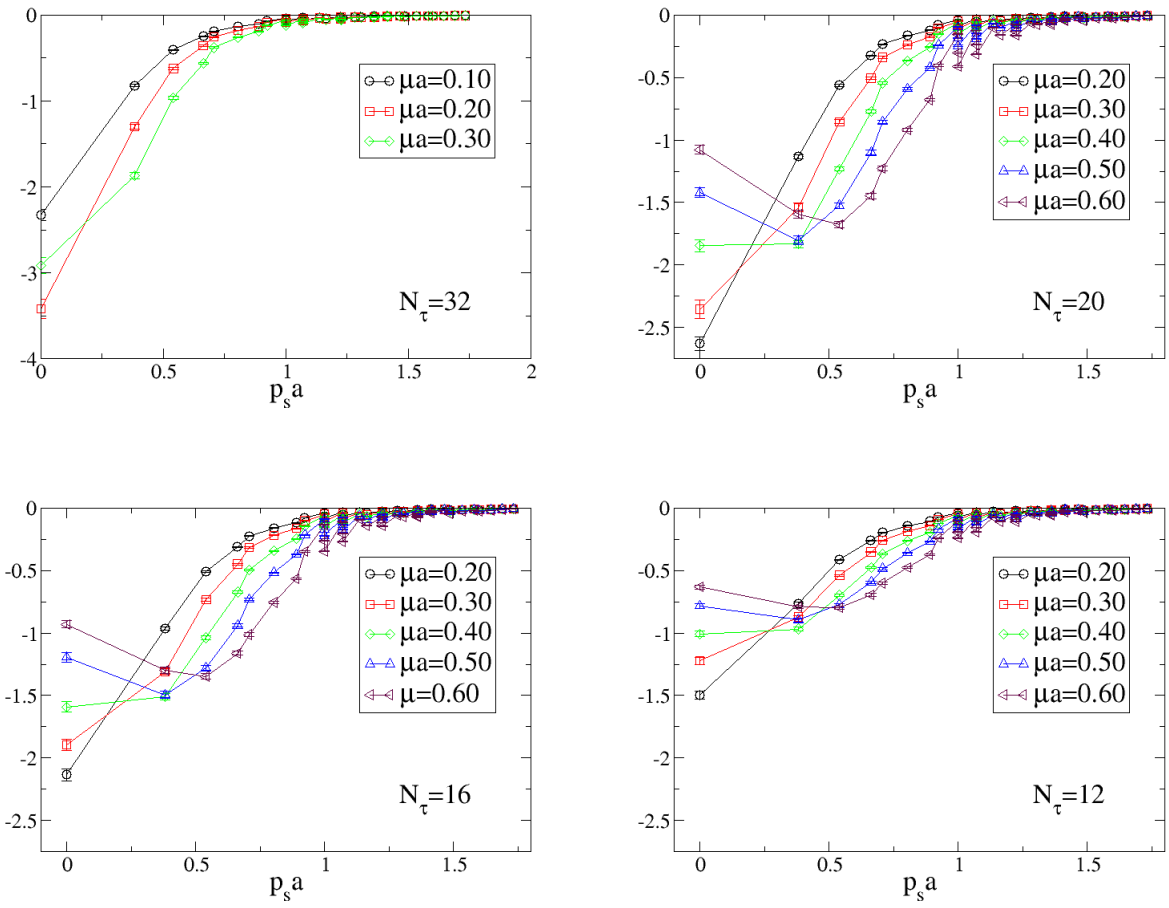

Figure 4.7: Real parts of the A_b form factors versus spatial momentum on the finer $16^3 \times N_\tau$ lattices at various chemical potentials for the lowest Matsubara mode. The diquark source value is $ja = 0.03$.

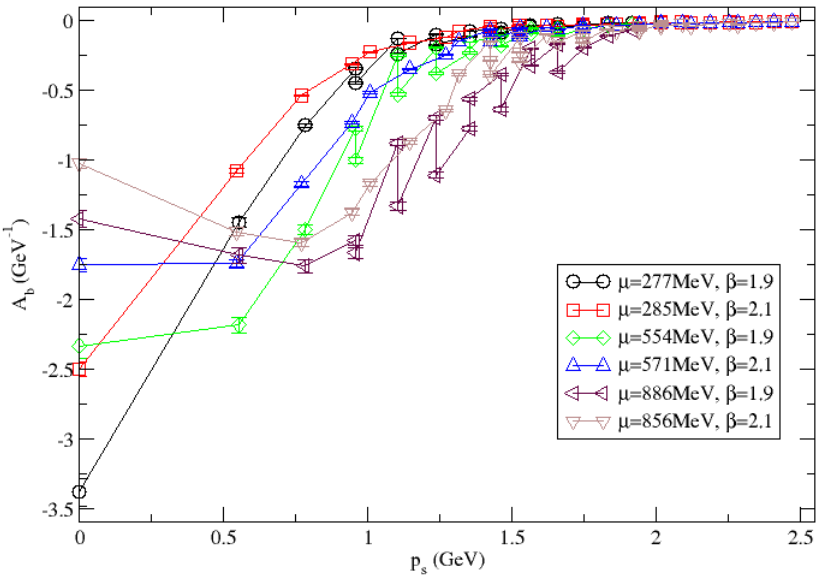

Figure 4.8: Real parts of the A_b form factors versus spatial momentum on the finer $16^3 \times 20$ ($ja = 0.03 \equiv 42.8$ MeV) and on the coarser $12^3 \times 24$ ($ja = 0.04 \equiv 44.3$ MeV) lattices. The lowest Matsubara mode shown. This is equivalent to 224 MeV on the finer and to 145 MeV on the coarser lattice.

of the form factor at low spatial momenta, as the temperature increases.

In Fig. 4.10 we compare the A_c form factors for two chemical potential values on the coarser lattice with those given in Fig. 4.9. Again, we see that on both lattices the form factor converges to zero as the spatial momentum increases. Its values at low spatial momenta are consistent at high chemical potential, where it is also positive. At low chemical potentials, while its behaviour is similar on the two lattices, its absolute value is bigger on the coarser lattice.

- Form Factor A_d : This is the tensor-type form factor of the anomalous propagation. As opposed to the normal propagator form factor S_d, its real parts have been found to vanish while the imaginary parts turned out to be non-zero. They are shown at various chemical potentials and at four different temperatures in Fig. 4.11.

At every temperature, the maximum value is enhanced as the chemical potential increases except for the last chemical potential value, $\mu = 0.60$, where it occurs slightly below the previous maximum value. A clear suppression is observed as the temperature increases at all chemical potentials. These observations suggest that this form factor is affected both by the normal to superfluid phase transition and by the chiral symmetry restoration.

In Fig. 4.12 we compare the A_d form factors for three chemical potential values on the coarser lattice $12^3 \times 24$ with those given in Fig. 4.11. At the two lower chemical potentials, the form factor values are quite close on the two lattices. At the highest chemical potential and at low spatial momenta, the form factor has bigger values on the finer lattice.

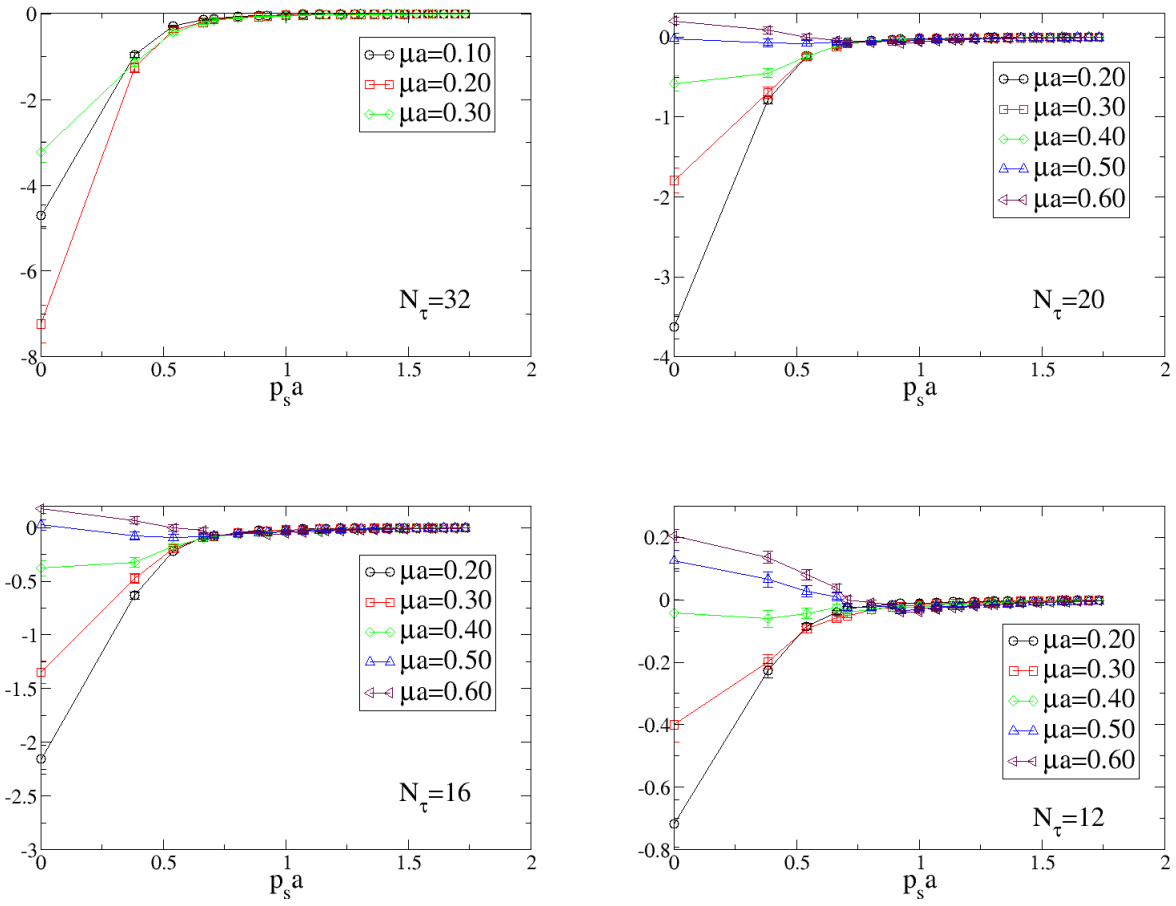

Figure 4.9: Real parts of the A_c form factors versus spatial momentum on the finer $16^3 \times N_\tau$ lattices at various chemical potentials, for the lowest Matsubara mode. The diquark source value is $ja = 0.03$.

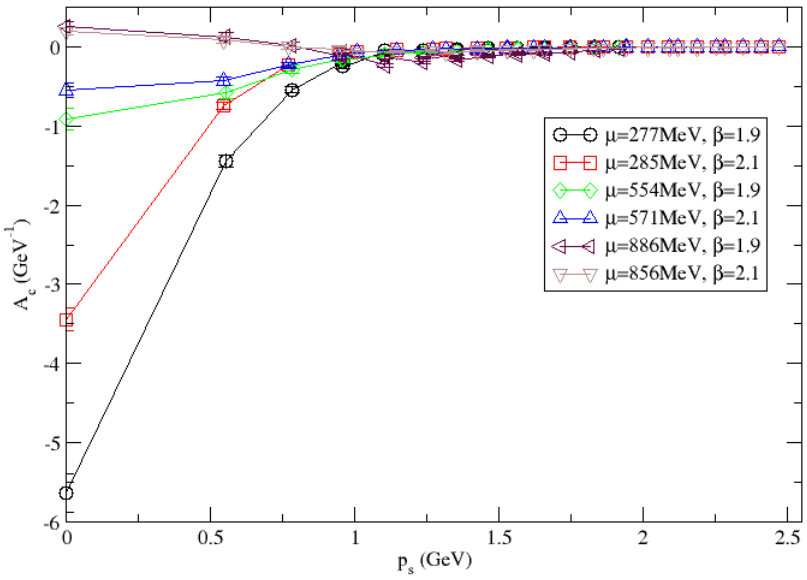

Figure 4.10: Real parts of the A_c form factors versus spatial momentum on the finer $16^3 \times 20$ ($ja = 0.03 \equiv 42.8$ MeV) and on the coarser $12^3 \times 24$ ($ja = 0.04 \equiv 44.3$ MeV) lattices. The lowest Matsubara mode shown. This is equivalent to 224 MeV on the finer and to 145 MeV on the coarser lattice.

4.8 Diquark Source Dependence

We finally investigate the effect of the diquark source value used in the calculations on the form factors. We did the comparison on the coarser lattice with diquark sources $j = 0.02$ and $j = 0.04$. We first present comparisons of the the normal form factors corresponding to different diquark sources in Fig. 4.13.

For the S_b form factor, for the chemical potentials above the onset transition, we observe that the form factor is suppressed. Because S_b is related to the dynamical mass, this signals dominance of diquark condensate, and hence, the anomalous propagation at chemical potentials above the onset transition. However, below the onset transition, dynamical mass and the form factor have much bigger values. Nevertheless, in this region, we still observe that S_b has a smaller value for the higher diquark source. This is a kind of "artificial" suppression of the dynamical mass by the externally introduced diquark source, which confirms the effect of the diquark source of promoting the diquark condensate.

Form factor S_a seems to extrapolate to zero above the onset transition, as the decrease in the values with decreasing diquark source suggests. However below the onset transition, the behaviour is the opposite: its values increase with decreasing diquark source. The normal propagation is strongly affected by the diquark source above the onset transition.

For the form factor S_c there was a problem with the data above the onset transition chemical potential which we left out. Below the onset transition we see that the absolute value of the propagator becomes smaller with an increase in the diquark source. This again shows

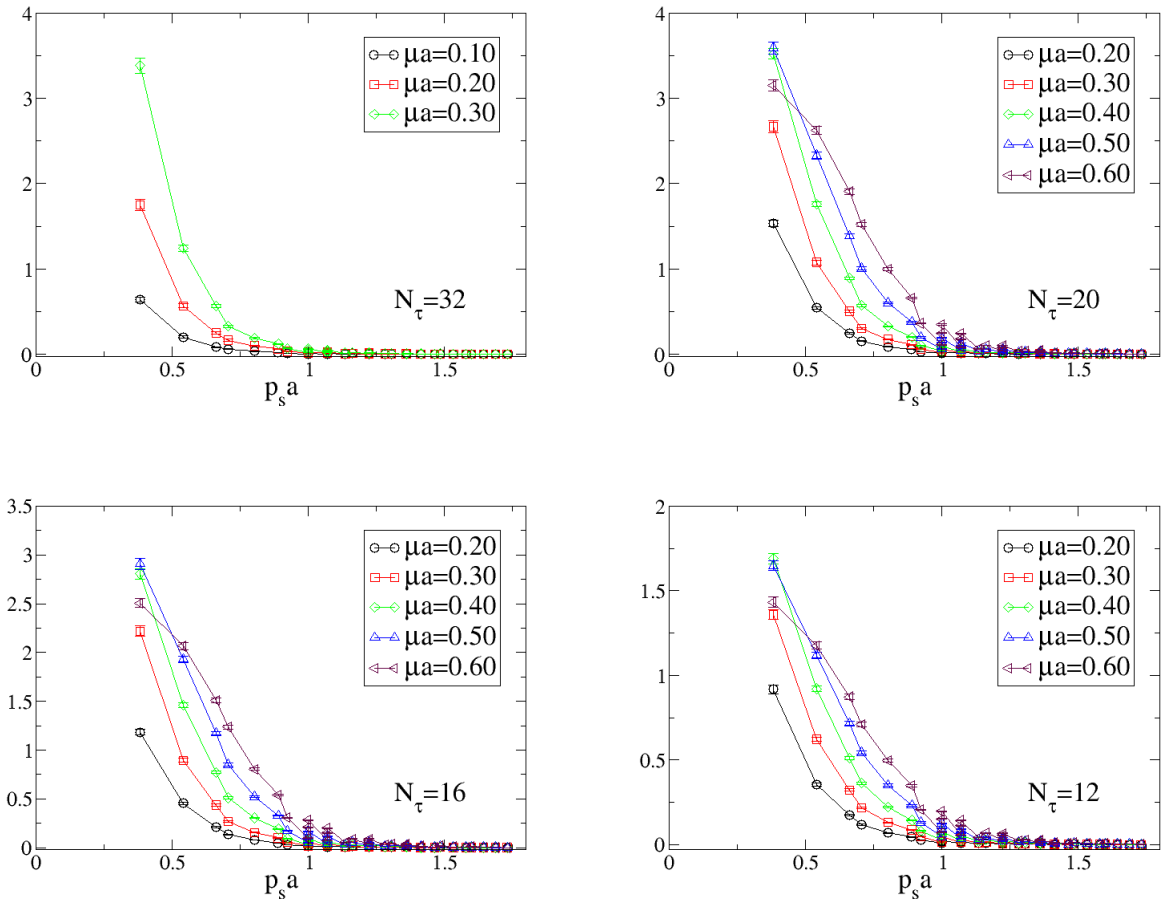

Figure 4.11: Imaginary parts of the A_d form factors versus spatial momentum on the finer $16^3 \times N_\tau$ lattices at various chemical potentials for the lowest Matsubara mode. The diquark source value is $ja = 0.03$.

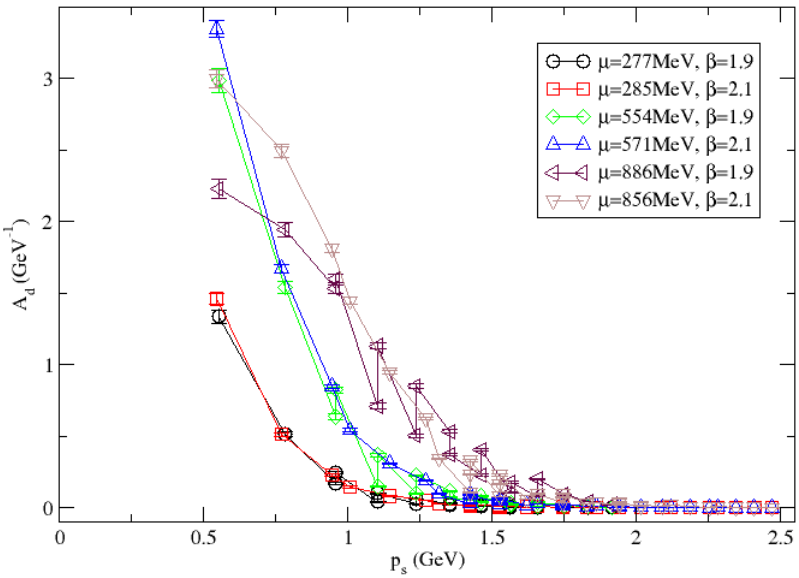

Figure 4.12: Imaginary parts of the A_d form factors versus spatial momentum on the finer $16^3 \times 20$ ($ja = 0.03 \equiv 42.8$ MeV) and on the coarser $12^3 \times 24$ ($ja = 0.04 \equiv 44.3$ MeV) lattices. The lowest Matsubara mode shown. This is equivalent to 224 MeV on the finer and to 145 MeV on the coarser lattice.

suppression of normal propagation by the diquark source.

Next, we present comparisons of the anomalous form factors corresponding to different diquark sources in Fig. 4.14.

The form factor A_b, which is associated with the diquark condensate, seems to extrapolate to zero above the onset transition, whereas it has finite value below the onset transition. This is puzzling because we expect the anomalous propagation to occur above the onset transition, which would have been signalled by a finite value of this form factor in this region. This needs further investigation with more diquark source values and a careful extrapolation to the physical limit.

The form factor A_c goes to zero towards high spatial momenta for all diquark sources and all chemical potentials. At zero spatial momentum, below the onset transition its absolute value grows bigger with increasing diquark source. We do not have a physical interpretation of this.

For A_d, we have the same puzzling situation as we had for A_b, i.e., the form factor seems to extrapolate to zero above the onset transition but has a finite value below the onset transition. This is opposite to what we expect since the anomalous propagation should occur above the onset transition, which needs further investigation.

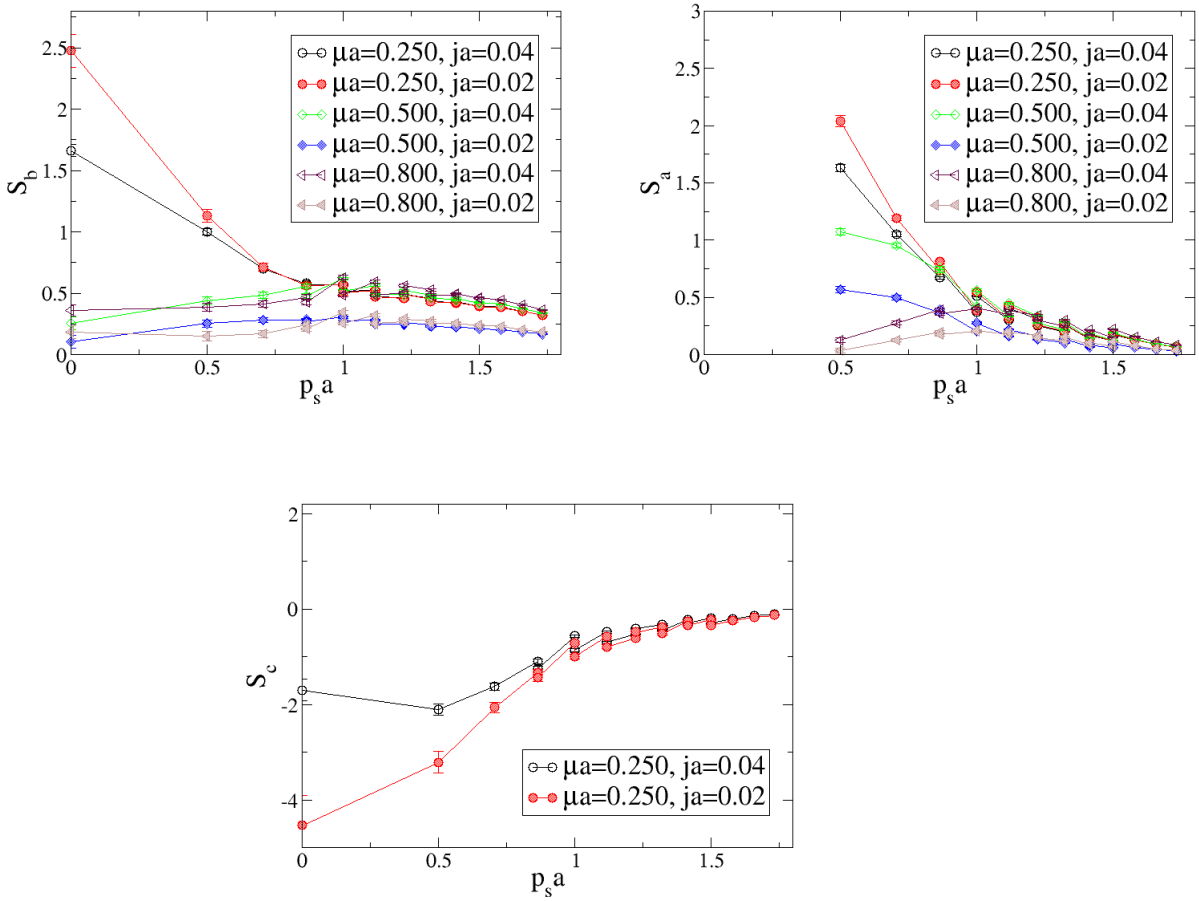

Figure 4.13: Form factors for the normal propagation on the coarser lattice with diquark sources $j = 0.02$ and $j = 0.04$.

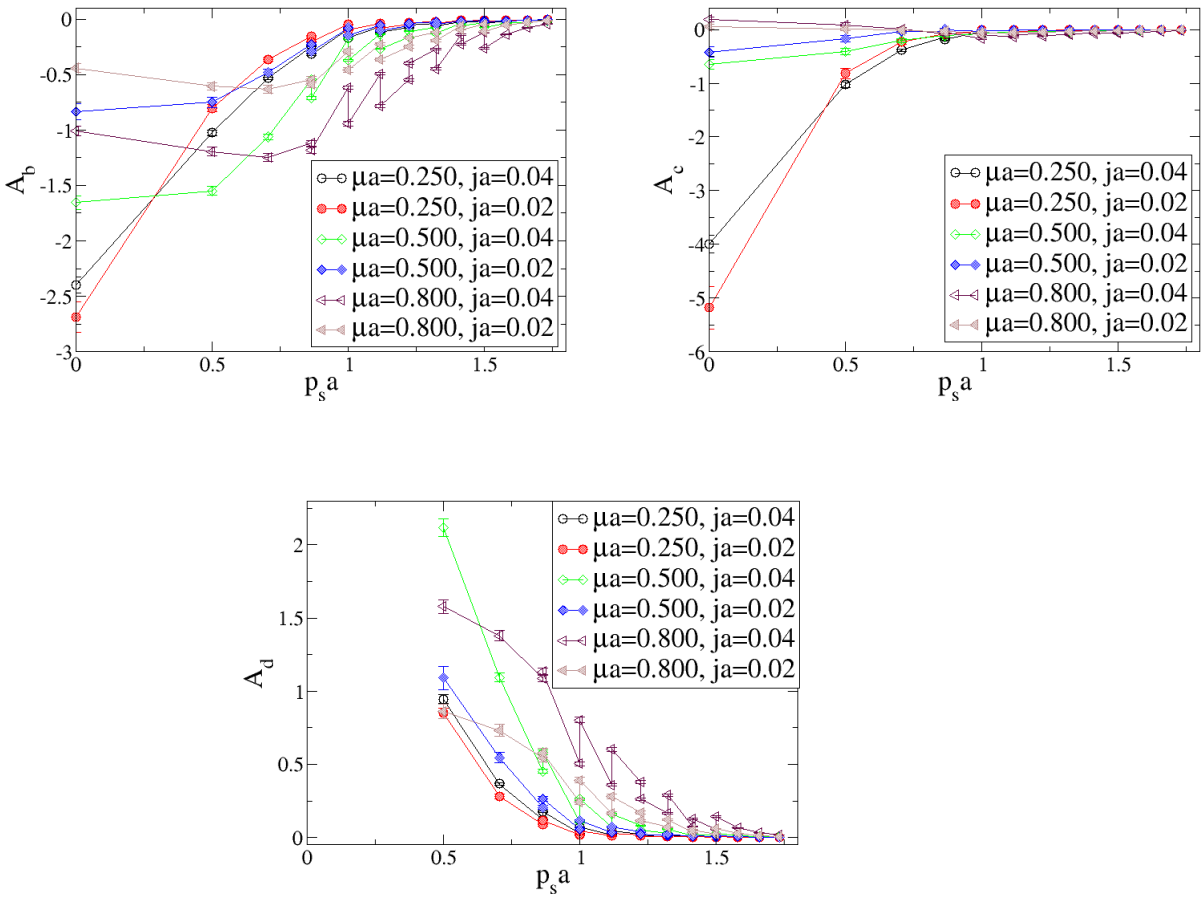

Figure 4.14: Form factors for the anomalous propagation on the coarser lattice with diquark sources $j = 0.02$ and $j = 0.04$.

4.9 Summary

In this part of the work, we investigated the form factors of normal and anomalous quark propagation. D-type (tensoral type) form factor of normal propagation and A-type (temporal vector type) form factor of the anomalous propagation have been found to vanish.

We first presented our results for the form factors S_b, S_c and S_d for normal propagation on the finer lattice and compared them with the results on the coarser lattice. Our results for S_b was consistent with the dominance of the chiral condensate below the onset transition, and that of the diquark condensate above the onset transition, which is physically in line with normal to superfluid phase transition as the chemical potential increases. On comparison with the coarser lattice we saw that the behaviour of the form factor was similar on both lattices whereas it has bigger values on the coarser.

Form factor S_a showed suppression towards high chemical potentials, confirming the anomalous quark propagation in this region. Its behaviour on the finer lattice was consistent with that on the coarser lattice, while this time the finer lattice values were bigger.

Form factor S_c signalled the presence of a Fermi surface. At zero spatial momentum, its values were negative for low chemical potentials, which increased to positive values as the chemical potential increases. Its values approached zero towards high spatial momenta. Its behaviour was similar on the coarser lattice.

Next we presented our results for the form factors A_b, A_c and A_d for anomalous propagation on the finer lattice and compared them with the results on the coarser lattice.

Our results for A_b was again consistent with rotation of the chiral condensate to the diquark condensate as the chemical potential increases. The form factor had bigger values in the negative direction on the coarser lattice.

We saw that the values for A_c converges to zero from negative values at low chemical potentials and from positive values at high chemical potentials. We observe an overall suppression of the form factor at low spatial momenta, as the temperature increases. However we do not have a direct physical interpretation of this form factor.

The non-zero value of A_d at low spatial momenta confirmed the presence of the anomalous propagation. As expected, its values are suppressed at low chemical potential values.

We finally investigated the diquark source dependence of the form factors. Except for the anomalous factors A_b and A_d their dependence on the diquark source were in line with our physical expectations. For A_b and A_c we need more data with different diquark source values for a more careful analysis, which is left to a future study.

Chapter 5

Summary and Outlook

Two-colour QCD is one of the methods that allows numerical simulations at finite densities, where interesting and new physical phenomena are expected to occur.

Both QCD and two-colour QCD have a rich phase structure with respect to the variation of the chemical potential and temperature. The low density and the low temperature region falls into the regime that we are familiar with in our daily observations, in which quarks are confined. More interesting phases emerge as one or both of the control parameters increase.

As the chemical potential increases at low temperatures in two-colour QCD, there occurs a phase transition, where quarks pair up giving rise to a superfluid phase. An analogous phenomenon is the BCS pairing of electrons in condensed matter physics, which gives rise to a superconducting phase.

At high temperature quarks get deconfined, giving rise to a phase that is referred to as the quark-gluon plasma. This can be thought as a "soup" in which quarks and gluons can move freely. The order parameter for this transition is the Polyakov loop in lattice QCD. There is also the possibility for the quarks to get deconfined at low temperature but extremely high chemical potential. This phase is expected to occur in the cores of compact stars.

In a dense medium, i.e., in the presence of a chemical potential, in addition to the normal propagation of quarks, there occurs a phenomenon that is called the anomalous quark propagation, in which a quark at some point in space-time propagates into an antiquark (more adequately, a diquark turns into an anti-diquark).

The quark propagator in a dense medium can not be written analytically. We therefore write it in terms of some coefficient functions and compute them numerically to extract information about the behaviour of the propagator, and hence, that of the quarks. This is done both for the normal and the anomalous quark propagation.

Below is a more descriptive summary of the results obtained in the thesis.

In this work we presented our numerical simulation results on a coarse lattice with $\beta = 1.9$ and $a = 0.178 \pm 0.006$ fm, and on a finer lattice with $\beta = 2.1$ and $a = 0.1380^{+0.0052}_{-0.0072}$ fm. Where possible, we compared the results from the two lattices. As far as we know, the fine lattice is the finest one studied in the literature for two-colour QCD with two fermion flavours at finite density. The form factors of Chapter 4, for the normal and the anomalous quark propagation in a dense medium is presented for the first time in the literature.

Throughout the study, we found out that there are still significant lattice spacing effects on some quantities. Therefore, our future aim is to make simulations on a yet finer lattice to draw more precise conclusions about both the behaviour of the quark and the gluon propagators and about the phase transitions, hence, about the phase diagram of two-colour QCD. For the phase transitions it is apparent to us that we need data obtained using more diquark source values to make better extrapolations to the physical limit. We also need data corresponding to more temperature values for a better understanding of the nature of phase transitions.

In Chapter 2, we first investigated the static quark potential on the finer lattice and observed linear behaviour with respect to spatial Wilson loop separation. We set the scale on the finer lattice by means of the Regge trajectory and found the value $0.1380^{+0.0052}_{-0.0072}$ fm for lattice spacing.

We calculated the diquark condensate, which is the order parameter for the normal to superfluid phase transition, using different values for the diquark source both on the coarser and on the finer lattices. We plotted our results with respect to temperature and observed the phase transition as the temperature increases. We found out that the critical temperature, T_c, does not seem to depend on the chemical potential. However we could not determine the value for T_c as we did not have enough data. This is left to a future study.

Our investigation for the diquark condensate supported the formation of a Fermi surface, consistent with the BCS mechanism for the normal to superfluid phase transition. Our plots were consistent with this hypothesis as we saw clear plateaux in the region between moderate to high densities.

In the diquark condensate calculations our extrapolations to the physical limit were not ideal in that we obtained quite big values for χ^2/N_{dof}. To make better extrapolations we want to include more diquark source values. This will also enable us to draw more precise conclusions about the phase transitions. This is also left to future studies.

Our main finding from the study of the quark number density was that the system behaves like a Stefan-Bolzmann gas at high densities.

Another phenomenon we studied was deconfinement phase transition. Both on the finer and on the coarser lattice we found a smooth crossover to deconfined phase and we observed that an increase in the chemical potential lowers the critical temperature for deconfinement.

In Chapter 3, we first presented our result for the gluon propagator at zero chemical potential and zero temperature, calculated on the coarser lattice. Our plot supports a massive boson-like behaviour of the propagator, rather than enhancement in the infrared momentum region.

At finite potential the gluon propagator splits into spatially transverse (chromomagnetic) and spatially longitudinal (chromoelectric) components and we plotted them both with respect to spatial momentum and chemical potential as well as investigating their thermal behaviour. In this work we ignored the effects of the Gribov copies. This is, again, left to a future study.

In general we observed suppression of the electric and the magnetic components with increasing chemical potential. An exception is the magnetic component on the coarser $16^3 \times 8$ lattice, where we observed an interesting peak around the superfluid confined phase at two lowest spatial momenta, and even a slight increase in the deconfined phase at the highest three spatial momenta. Our finding that the static magnetic component is suppressed at high density is in contradiction to perturbation theory, where, to all orders, it is not suppressed. This might have an impact on functional studies like DSE and FRG methods.

Where data were available, we compared the gluon propagator on the finer and on the coarser lattice. We found that the qualitative behaviour remains the same on different lattices, the quantitative discrepancy getting smaller at higher spatial momenta.

We also investigated the response of the magnetic and the electric components to an increase in the temperature and saw that the electric component shows a dramatic suppression at high temperature, while the magnetic component is not as much sensitive, although it does show a little suppression in the infrared momentum region.

We tried to fit our data for the two components of the gluon propagator to a model function, for a better understanding of their functional behaviour. There are three input parameters Λ, $a_{M,E}$, $b_{M,E}$ for the magnetic and the electric components separately. Λ is assumed to be independent of the temperature and the chemical potential and we investigated the effects of the medium and temperature change on the remaining two parameters.

In Chapter 4, we investigated the form factors of normal and anomalous quark propagation. D-type (tensoral type) form factor of normal propagation and A-type (temporal vector type) form factor of anomalous propagation have been found to vanish.

We first presented our results for the form factors S_b, S_c and S_d for normal propagation on the finer lattice and compared them with the results on the coarser lattice. Our results were consistent with the dominance of the chiral condensate below the onset transition, and that of the diquark condensate above the onset transition, which is physically in line with normal to superfluid phase transition as the chemical potential increases. On comparison with the coarser lattice we saw that the behaviour of the form factor was similar on both lattices whereas it has bigger values on the coarser.

Next we presented our results for the form factors A_b, A_c and A_d for anomalous propagation on the finer lattice and compared them with the results on the coarser lattice. Our results were consistent with the rotation of the chiral condensate to the diquark condensate and the occurrence of the anomalous propagation as the chemical potential increases.

We finally investigated the diquark source dependence of the form factors. Except for the anomalous factors A_b and A_d, their dependence on the diquark source were in line with our physical expectations. For A_b and A_c we need more data with different diquark source values for a more careful analysis, which is left to a future study.

Among the open questions after this study are the nature of deconfinement transition, obtaining the form factors of the inverse propagation, and analytically proving that the tensoral type anomalous form factor is non-zero. It might also be interesting to study the effect of the Gribov copies on the gluon propagator as well as trying other possible functional forms to fit the data.

Appendix A

Free Propagator at Finite Chemical Potential

We will show that the Fourier transform of the expression

$$M(\mu) = \delta_{xy} - \kappa \sum_{\nu} \left[(\mathbf{1} - \gamma_\nu) \, \mathrm{e}^{\mu \delta_{\nu 0}} U_\nu(x) \, \delta_{y,x+\hat{\nu}} + (\mathbf{1} + \gamma_\nu) \, \mathrm{e}^{-\mu \delta_{\nu 0}} U_\nu^\dagger(y) \, \delta_{y,x-\hat{\nu}} \right] \tag{A.1}$$

is

$$M(p) = \frac{\mathrm{i}}{a} \sum_{j=1}^{3} \gamma_j \sin(a p_j) + \frac{\mathrm{i}}{a} \gamma_4 \sin(a\omega) + m_0 + \frac{1}{a} \sum_{j=1}^{3} [\mathbf{1} - \cos(p_j a)]$$

$$+ \frac{1}{a} [\mathbf{1} - \cos(\omega a)], \tag{A.2}$$

where μ is the chemical potential and $\omega = p_4 - i\mu$. We are interested in the non-interacting case, so we will set $U = \mathbf{1}$ below.

We will perform a Fourier transform on the lattice, so it will be helpful to keep in mind that

$$\delta_{pq} = \sum_{x} e^{ix(p-q)} \tag{A.3}$$

on the lattice. We will omit the lattice spacing a throughout the calculations.

$$\mathcal{F}\{M(\mu)\} = \sum_{x,y} e^{i(qx+py)} M_{xy} \tag{A.4}$$

$$= \sum_{x} e^{iqx} \sum_{y} e^{ipy} \left[\delta_{xy} - \kappa \sum_{\nu} (\mathbf{1} - \gamma_\nu) \, \mathrm{e}^{\mu \delta_{\nu 0}} \delta_{y,x+\hat{\nu}} - \kappa \sum_{\nu} (\mathbf{1} + \gamma_\nu) \, \mathrm{e}^{-\mu \delta_{\nu 0}} \delta_{y,x-\hat{\nu}} \right]$$

$$= \sum_{x} e^{iqx} \left[e^{ipx} - \kappa \sum_{\nu} (\mathbf{1} - \gamma_\nu) \, \mathrm{e}^{\mu \delta_{\nu 0}} e^{ip(x+\hat{\nu})} - \kappa \sum_{\nu} (\mathbf{1} + \gamma_\nu) \, \mathrm{e}^{-\mu \delta_{\nu 0}} e^{ip(x-\hat{\nu})} \right]$$

$$= \sum_x e^{i(p+q)x} - \kappa \sum_\nu (\mathbf{1} - \gamma_\nu)\, \mathrm{e}^{\mu\delta_{\nu 0}} \sum_x e^{iqx} e^{ip(x+\hat{\nu})}$$

$$-\kappa \sum_\nu (\mathbf{1} + \gamma_\nu)\, \mathrm{e}^{-\mu\delta_{\nu 0}} \sum_x e^{iqx} e^{ip(x-\hat{\nu})} \tag{A.5}$$

Here:

$$\sum_x e^{i(p+q)x} = \delta_{p,-q}, \quad \sum_x e^{iqx} e^{ip(x+\hat{\nu})} = e^{ip\hat{\nu}} \sum_x e^{i(p+q)x} = e^{ip_\nu} \delta_{p,-q}, \tag{A.6}$$

and

$$\sum_x e^{iqx} e^{ip(x-\hat{\nu})} = e^{-ip_\nu} \delta_{p,-q}. \tag{A.7}$$

$$\Longrightarrow \mathcal{F}\{M(\mu)\} = \delta_{p,-q} - \kappa \sum_\nu (\mathbf{1} - \gamma_\nu)\, \mathrm{e}^{\mu\delta_{\nu 0}} e^{ip_\nu} \delta_{p,-q}$$

$$-\kappa \sum_\nu (\mathbf{1} + \gamma_\nu)\, \mathrm{e}^{-\mu\delta_{\nu 0}} e^{-ip_\nu} \delta_{p,-q} \tag{A.8}$$

Below we will omit the common factor $\delta_{p,-q}$ in the expressions. This only has the effect of imposing momentum conservation.

$$\mathcal{F}\{M(\mu)\} = \mathbf{1} - \kappa \sum_j (\mathbf{1} - \gamma_j)\, e^{ip_j} - \kappa\, (\mathbf{1} - \gamma_4)\, e^{\mu} e^{ip_4}$$

$$-\kappa \sum_j (\mathbf{1} + \gamma_j)\, e^{-ip_j} - \kappa\, (\mathbf{1} + \gamma_4)\, e^{-\mu} e^{-ip_4}$$

$$= \mathbf{1} - \kappa \sum_j e^{ip_j} + \kappa \sum_j \gamma_j e^{ip_j} - \kappa \sum_j e^{-ip_j} - \kappa \sum_j \gamma_j e^{-ip_j}$$

$$-\kappa e^{\mu} e^{ip_4} + \kappa \gamma_4 e^{\mu} e^{ip_4} - \kappa e^{-\mu} e^{-ip_4} - \kappa \gamma_4 e^{-\mu} e^{-ip_4}$$

$$= \mathbf{1} - \kappa \sum_j \left(e^{ip_j} + e^{-ip_j}\right) + \kappa \sum_j \gamma_j \left(e^{ip_j} - e^{-ip_j}\right) - \kappa e^{i(p_4 - i\mu)}$$

$$-\kappa e^{-i(p_4 - i\mu)} + \kappa \gamma_4 e^{i(p_4 - i\mu)} - \kappa \gamma_4 e^{-i(p_4 - i\mu)}$$

$$= \mathbf{1} - 2\kappa \sum_j \cos(p_j a) + 2\kappa i \sum_j \gamma_j \sin(p_j a) - 2\kappa \cos[(p_4 - i\mu)\, a]$$

$$+2i\kappa\gamma_4 \sin[(p_4 - i\mu)\, a] \tag{A.9}$$

Here $\kappa = \frac{1}{2(am_0+4)}$ is the hopping parameter.

$$\Longrightarrow \mathcal{F}\{M(\mu)\} = \mathbf{1} - \frac{1}{(am_0+4)} \sum_j \cos(p_j a) + \frac{i}{(am_0+4)} \sum_j \gamma_j \sin(p_j a)$$

$$-\frac{1}{(am_0+4)} \cos(\omega a) + \frac{i\gamma_4}{(am_0+4)} \sin(\omega a) \tag{A.10}$$

$$= \frac{1}{(am_0+4)} \Bigg\{ am_0 + 4 - \sum_j \cos(p_j a) + i \sum_j \gamma_j \sin(p_j a)$$

$$- \cos(\omega a) + i\gamma_4 \sin(\omega a) \Bigg\} \tag{A.11}$$

Note that $4 = \sum_\nu \mathbf{1}_{4\times 4} = 1 + \sum_j \mathbf{1}_{3\times 3}$.

$$\Longrightarrow \mathcal{F}\{M(\mu)\} = \frac{1}{(am_0+4)} \Bigg\{ am_0 + i \sum_j \gamma_j \sin(p_j a) + i\gamma_4 \sin(\omega a)$$

$$+ \sum_j [\mathbf{1} - \cos(p_j a)] + 1 - \cos(\omega a) \Bigg\} \tag{A.12}$$

$$= \frac{a}{(am_0+4)} \Bigg\{ m_0 + \frac{i}{a} \sum_j \gamma_j \sin(p_j a) + \frac{i}{a}\gamma_4 \sin(\omega a)$$

$$+ \frac{1}{a} \sum_j [\mathbf{1} - \cos(p_j a)] + \frac{1}{a} [1 - \cos(\omega a)] \Bigg\}. \tag{A.13}$$

The factor $\frac{a}{(am_0+4)}$ can be embedded into a redefinition of the fermion field, which leaves the expression with the desired result.

Appendix B

General Form of Fermion Propagator in Dense Medium

This appendix gives a reproduction of the reference [48], which will lead us to the most general form of the spectral function of the normal propagation in terms of the form factors. After that, we give a summary of our attempts to apply this argument to the anomalous quark propagation.

B.1 Spectral Function

We want to derive the most general form that the normal part of the quark propagator in a dense medium can assume in terms of the form factors S_a, S_b S_c and S_d , i.e., the expression:

$$S(p) = S_b(p) + \mathrm{i}p^k S_a(p)\gamma_k + \mathrm{i}\omega S_c(p)\gamma_4 + \not{p}\gamma_4 S_d(p). \tag{B.1}$$

In eq. (B.1) $\omega = p_4 - \mathrm{i}\mu$, and the form factor S_d will turn out to be zero.

We will make use of the spectral function,

$$\rho_{\alpha\beta}(q,u) = \int d^4x e^{iq\cdot x} \langle \psi_0(u) | \eta_\alpha(x) \bar{\eta}_\beta(0) | \psi_0(u) \rangle, \tag{B.2}$$

in terms of which the quark propagator can be written. Here $\eta(x)$ is the quark field and q is the quark momentum. The effect of the medium that provides the finite density enters the expression through the medium four-velocity u^μ.

It will be convenient in the following to remove the x dependence of the spectral functions by inserting the identity operator written in terms of the energy-momentum eigenstates:

$$\rho_{\alpha\beta}(q,u) = \sum_n \int d^4x e^{iq\cdot x} \langle \psi_0(u) | \eta_\alpha(x) | n \rangle \langle n | \bar{\eta}_\beta(0) | \psi_0(u) \rangle$$

$$= \sum_n \int d^4x e^{iq\cdot x} \left\langle \psi_0(u) | e^{i\hat{P}\cdot x} \eta_\alpha(0) e^{-i\hat{P}\cdot x} | n \right\rangle \langle n | \bar{\eta}_\beta(0) | \psi_0(u) \right\rangle$$

$$= \sum_n \int d^4x e^{i(q\cdot x + P_0\cdot x - P_n\cdot x)} \left\langle \psi_0(u) \left| \eta_\alpha(0) \right| n \right\rangle \left\langle n \left| \bar{\eta}_\beta(0) \right| \psi_0(u) \right\rangle$$

$$= (2\pi)^4 \sum_n \delta(q + P_0 - P_n) \left\langle \psi_0(u) \left| \eta_\alpha(0) \right| n \right\rangle \left\langle n \left| \bar{\eta}_\beta(0) \right| \psi_0(u) \right\rangle . \tag{B.3}$$

In eq. (B.3) P_0^μ is the ground state four momentum which is the product of the ground state mass with the four velocity, u^μ, of the medium and P_n^μ is the four momentum of the state $|n\rangle$. We will expand the spectral function in a standard way, using the complete set of basis matrices,

$$\{\Gamma_i\} = \{1, i\gamma_5, \gamma_\mu, \gamma_\mu\gamma_5, \sigma_{\mu\nu}\}, \tag{B.4}$$

where $\sigma_{\mu\nu} = \frac{i}{2}[\gamma_\mu, \gamma_\nu]$:

$$\rho_{\alpha\beta}(q,u) = \pi_s(q,u)\,\delta_{\alpha\beta} + \pi_5(q,u)\{i\gamma_5\}_{\alpha\beta} + \pi^\mu(q,u)\{\gamma_\mu\}_{\alpha\beta}$$

$$+\pi_5^\mu(q,u)\{\gamma_\mu\gamma_5\}_{\alpha\beta} + \pi^{\mu\nu}(q,u)\{\sigma_{\mu\nu}\}_{\alpha\beta} . \tag{B.5}$$

We have the following orthogonality condition among the elements of the basis set (B.4):

$$\mathrm{Tr}\Gamma_i\Gamma_j \propto \delta_{ij}, \tag{B.6}$$

which we will make use of to show that the coefficient functions, π, of (B.5) are all real. To this end let us take the adjoint of (B.3) :

$$\rho^\dagger_{\alpha\beta}(q,u)$$

$$= (2\pi)^4 \sum_n \delta(q + P_0 - P_n) \left\langle \psi_0(u) \left| \eta_\beta(0) \right| n \right\rangle^* \left\langle n \left| \bar{\eta}_\alpha(0) \right| \psi_0(u) \right\rangle^*$$

$$= (2\pi)^4 \sum_n \delta(q + P_0 - P_n) \left\langle n \left| \eta^\dagger_\beta(0) \right| \psi_0(u) \right\rangle \left\langle \psi_0(u) \left| (\gamma_0)_{\alpha\kappa} \eta_\kappa(0) \right| n \right\rangle$$

$$= (\gamma_0)_{\alpha\kappa} (2\pi)^4 \sum_n \delta(q + P_0 - P_n) \left\langle \psi_0(u) \left| \eta_\kappa(0) \right| n \right\rangle \left\langle n \left| \eta^\dagger_\lambda(0) (\gamma_0\gamma_0)_{\lambda\beta} \right| \psi_0(u) \right\rangle$$

$$= (\gamma_0)_{\alpha\kappa} (2\pi)^4 \sum_n \delta(q + P_0 - P_n) \left\langle \psi_0(u) \left| \eta_\kappa(0) \right| n \right\rangle \left\langle n \left| \eta^\dagger_\lambda(0) (\gamma_0)_{\lambda\sigma} \right| \psi_0(u) \right\rangle (\gamma_0)_{\sigma\beta}$$

$$= (\gamma_0)_{\alpha\kappa} (2\pi)^4 \sum_n \delta (q + P_0 - P_n) \langle \psi_0 (u) | \eta_\kappa (0) | n \rangle \langle n | \bar{\eta}_\sigma (0) | \psi_0 (u) \rangle (\gamma_0)_{\sigma\beta}$$

$$\Longrightarrow \rho^\dagger_{\alpha\beta} (q, u) = \{\gamma_0 \rho (q, u) \gamma_0\}_{\alpha\beta}$$

$$\Longrightarrow \rho (q, u) = \gamma_0 \rho (q, u)^\dagger \gamma_0. \tag{B.7}$$

In terms of the coefficient functions, eq. (B.7) reads:

$$\pi_s (q, u) + i\pi_5 (q, u) \gamma_5 + \pi^\mu (q, u) \gamma_\mu + \pi^\mu_5 (q, u) \gamma_\mu \gamma_5 + \pi^{\mu\nu} (q, u) \sigma_{\mu\nu}$$

$$= \pi^*_s (q, u) + i\pi^*_5 (q, u) \gamma_5 + \pi^{\mu *} (q, u) \gamma_\mu + \pi^{\mu *}_5 (q, u) \gamma_\mu \gamma_5 + \pi^{\mu\nu *} (q, u) \sigma_{\mu\nu}, \tag{B.8}$$

where we used the relation,

$$\gamma_0 \Gamma^\dagger_i \gamma_0 = \Gamma_i, \tag{B.9}$$

that each element in the set (B.4) satisfies. We see from eq. (B.8) that all coefficient functions in the expansion (B.5) of the spectral function are real.

B.2 Lorentz Transformations

Under proper Lorentz transfomations the nuclear ground state transforms as

$$U (\lambda) | \psi_0 (u) \rangle \propto | \psi_0 (\lambda u) \rangle , \tag{B.10}$$

where $U (\lambda)$ is unitary. In order that $\eta (x)$ transforms like a spin-1/2 field the following must be satisfied:

$$U (\lambda) \eta (x) U^\dagger (\lambda) = S^{-1} (\lambda) \eta (\lambda x) . \tag{B.11}$$

In eq. (B.11) $S (\lambda)$ is a non-unitary matrix. It acts on the gamma matrices as follows:

$$S^{-1} (\lambda) \gamma_\mu S (\lambda) = \lambda^\nu_\mu \gamma_\nu, \tag{B.12}$$

and it satisfies

$$S^\dagger (\lambda) \gamma_0 = \gamma_0 S^{-1} (\lambda) . \tag{B.13}$$

Let us now write eq. (B.2) as

$$\rho(q,u)=\int d^4x e^{iq\cdot x}\left\langle \psi_0(u)\left|U^\dagger(\lambda)U(\lambda)\eta(x)\times\right.\right.$$

$$\left.\left.U^\dagger(\lambda)U(\lambda)\bar{\eta}(0)U^\dagger(\lambda)U(\lambda)\left|\psi_0(u)\right\rangle\right.\right. \tag{B.14}$$

where we inserted the identity to the left and to the right of $\eta(x)$, and to the right of $\bar{\eta}(x)$. Using eq. (B.11) in eq. (B.14) we obtain

$$\rho(q,u)=\int d^4x e^{iq\cdot x}\left\langle \psi_0(u)\left|U^\dagger(\lambda)S^{-1}\eta(\lambda x)\times\right.\right.$$

$$\left.\left.U(\lambda)\bar{\eta}(0)U^\dagger(\lambda)U(\lambda)\left|\psi_0(u)\right\rangle\right.\right. . \tag{B.15}$$

We need an expression for $U(\lambda)\bar{\eta}(0)$ to substitute in eq. (B.15) which we derive below:

$$U(\lambda)\eta(x)U^\dagger(\lambda)=S^{-1}(\lambda)\eta(\lambda x) \qquad (B.11)$$

$$\Longrightarrow U(\lambda)\eta^\dagger(x)U^\dagger(\lambda)=\eta^\dagger(\lambda x)\left(S^{-1}\right)^\dagger$$

$$\Longrightarrow U(\lambda)\eta^\dagger(0)=\eta^\dagger(0)\left(S^{-1}\right)^\dagger U(\lambda)$$

$$\Longrightarrow U(\lambda)\bar{\eta}(0)=\eta^\dagger(0)\left(S^{-1}\right)^\dagger U(\lambda)\gamma_0. \tag{B.16}$$

Using eq. (B.16) in eq. (B.17) we get

$$\rho(q,u)=\int d^4x e^{iq\cdot x}\left\langle \psi_0(u)\left|U^\dagger(\lambda)S^{-1}\eta_\alpha(\lambda x)\times\right.\right.$$

$$\left.\left.\eta^\dagger(0)\left(S^{-1}\right)^\dagger U(\lambda)\gamma_0 U^\dagger(\lambda)U(\lambda)\left|\psi_0(u)\right\rangle\right.\right. . \tag{B.17}$$

Recalling the action of U on the ground state, eq. (B.10), we can rewrite eq. (B.17) as:

$$\rho(q,u)=\int d^4x e^{iq\cdot x}\left\langle \psi_0(\lambda u)\left|S^{-1}(\lambda)\eta(\lambda x)\eta^\dagger(0)\left(S^{-1}(\lambda)\right)^\dagger\gamma_0\right|\psi_0(\lambda u)\right\rangle, \tag{B.18}$$

and using eq. (B.13) we obtain

$$\rho(q,u)=S^{-1}(\lambda)\int d^4x e^{iq\cdot x}\left\langle \psi_0(\lambda u)\left|\eta(\lambda x)\bar{\eta}(0)\right|\psi_0(\lambda u)\right\rangle S(\lambda). \tag{B.19}$$

As $q\cdot x$ is s Lorentz scalar, we have $q\cdot x=\lambda q\cdot\lambda x$, and we can write

$$\rho(q,u) = S^{-1}(\lambda) \int d^4x e^{i(\lambda q)\cdot(\lambda x)} \langle \psi_0(\lambda u) | \eta(\lambda x) \bar{\eta}(0) | \psi_0(\lambda u) \rangle S(\lambda). \tag{B.20}$$

By changing to the variable $y = \lambda x$ in eq. (B.20) we get

$$\rho(q,u) = S^{-1}(\lambda) \int d^4x e^{i\lambda q\cdot x} \langle \psi_0(\lambda u) | \eta(x) \bar{\eta}(0) | \psi_0(\lambda u) \rangle S(\lambda), \tag{B.21}$$

and by virtue of eq. (B.2) we obtain

$$\rho(q,u) = S^{-1}(\lambda) \rho(\lambda q, \lambda u) S(\lambda). \tag{B.22}$$

We can now use the expansion in eq. (B.5) to write

$$\pi_s(q,u) + i\pi_5(q,u)\gamma_5 + \pi^\mu(q,u)\gamma_\mu + \pi_5^\mu(q,u)\gamma_\mu\gamma_5 + \pi^{\mu\nu}(q,u)\sigma_{\mu\nu}$$

$$= S^{-1}(\lambda)\pi_s(\lambda q, \lambda u) S(\lambda) + i\pi_5(\lambda q, \lambda u) S^{-1}(\lambda)\gamma_5 S(\lambda)$$

$$+\pi^\mu(\lambda q, \lambda u) S^{-1}(\lambda)\gamma_\mu S(\lambda) + \pi_5^\mu(\lambda q, \lambda u) S^{-1}(\lambda)\gamma_\mu\gamma_5 S(\lambda)$$

$$+\pi^{\mu\nu}(\lambda q, \lambda u) S^{-1}(\lambda)\sigma_{\mu\nu} S(\lambda). \tag{B.23}$$

From eq. (B.23) we see that

$$\pi_s(q,u) = \pi_s(\lambda q, \lambda u), \tag{B.24}$$

$$\pi_5(q,u) = \pi_5(\lambda q, \lambda u), \tag{B.25}$$

which means that these coefficients are Lorentz scalars. We therefore conclude that these coefficients must be functions of $q \cdot u$ and q^2:

$$\pi_s(q,u) = \pi_s\left(q^2, q\cdot u\right), \tag{B.26}$$

$$\pi_5(q,u) = \pi_5\left(q^2, q\cdot u\right). \tag{B.27}$$

Similarly by looking at eq. (B.23) one infers that π^μ and π_5^μ behave as four-vectors which therefore can be written as:

$$\pi^\mu(q,u) = \pi_q\left(q^2, q\cdot u\right) q^\mu + \pi_u\left(q^2, q\cdot u\right) u^\mu, \tag{B.28}$$

$$\pi_5^\mu(q,u) = \pi_{5_q}\left(q^2, q\cdot u\right) q^\mu + \pi_{5_u}\left(q^2, q\cdot u\right) u^\mu. \tag{B.29}$$

Finally the coefficient function with two indices can be seen to transform as a Lorentz tensor and hence can be written as:

$$\pi^{\mu\nu}(q,u) = \pi_T\left(q^2, q\cdot u\right)\left(q^\mu u^\nu - u^\mu q^\nu\right) + \pi_T^{'}\left(q^2, q\cdot u\right)\epsilon^{\mu\nu\kappa\lambda}q_\kappa u_\lambda. \tag{B.30}$$

Gathering all the forms obtained for the coefficient functions we arrive at the following expansion for the spectral function:

$$\rho(q,u) = \pi_s + i\pi_5\gamma_5 + \pi_q q^\mu\gamma_\mu + \pi_u u^\mu\gamma_\mu + \pi_{5_q} q^\mu\gamma_\mu\gamma_5$$

$$+\pi_{5_u} u^\mu\gamma_\mu\gamma_5 + \pi_T\left(q^\mu u^\nu - u^\mu q^\nu\right)\sigma_{\mu\nu} + \pi_T^{'}\epsilon^{\mu\nu\kappa\lambda}q_\kappa u_\lambda\sigma_{\mu\nu}. \tag{B.31}$$

B.3 Parity Transformation

We now have the expansion eq. (B.31) and we know that the coefficents π are all real. In order to obtain more information about these coefficents we first investigate the parity transformation properties of the spectral function.

The parity transformation on our spin-1/2 field is

$$P^\dagger\eta(x)P = \gamma_0\eta(x_0, -\boldsymbol{x}), \tag{B.32}$$

where the operator P is unitary.

Let us insert the identity, $PP^\dagger$, to the right and to the left of $\eta(x)$ and to the right of $\bar{\eta}(x)$ in eq. (B.2):

$$\rho(q,u) = \int d^4x e^{iq\cdot x}\left\langle\psi_0(u)\right|PP^\dagger\eta(x)\times$$

$$PP^\dagger\bar{\eta}(0)PP^\dagger\left|\psi_0(u)\right\rangle. \tag{B.33}$$

From eq. (B.32) it follows that:

$$P^\dagger\eta(0)P = \eta^\dagger(0)\gamma_0\bar{\eta}(0),$$

$$\Longrightarrow P^\dagger\bar{\eta}(0)P = P^\dagger P^\dagger\eta^\dagger(0)PP,$$

and using the idempotence of P we obtain:

$$P^\dagger\bar{\eta}(0)P = \bar{\eta}(0)\gamma_0. \tag{B.34}$$

Substituting eq. (B.32) and eq. (B.34) in eq. (B.33) yields

$$\rho\left(q,u\right)=\int d^{4}xe^{iq\cdot x}\left\langle \psi_{0}\left(u\right)\left|P\gamma_{0}\eta\left(x_{0},-\boldsymbol{x}\right)\bar{\eta}\left(0\right)\gamma_{0}P^{\dagger}\right|\psi\left(u\right)\right\rangle ,\tag{B.35}$$

and acting with P and $P^{\dagger}$ on the ground state bra and ket respectively, we obtain

$$\rho\left(q,u\right)=\int d^{4}xe^{iq\cdot x}\left\langle \psi_{0}\left(u_{0},-\boldsymbol{u}\right)\left|\gamma_{0}\eta\left(x_{0},-\boldsymbol{x}\right)\bar{\eta}\left(0\right)\gamma_{0}\right|\psi\left(u_{0},-\boldsymbol{u}\right)\right\rangle .\tag{B.36}$$

Next we change to a new variable $y=\left(x_{0},-\boldsymbol{x}\right)$ in eq. (B.36):

$$\rho\left(q,u\right)=\gamma_{0}\int d^{4}ye^{iq_{0}\cdot y_{0}+i\boldsymbol{q}\cdot\boldsymbol{y}}\left\langle \psi_{0}\left(u_{0},-\boldsymbol{u}\right)\left|\eta\left(y\right)\bar{\eta}\left(0\right)\right|\psi\left(u_{0},-\boldsymbol{u}\right)\right\rangle \gamma_{0}.\tag{B.37}$$

We define

$$\tilde{k}\equiv\left(k_{0},-\boldsymbol{k}\right),\tag{B.38}$$

and with this definition we write eq. (B.37) as

$$\rho\left(q,u\right)=\gamma_{0}\rho\left(\tilde{q},\tilde{u}\right)\gamma_{0}.\tag{B.39}$$

We will now use eq. (B.39) in the expansion eq. (B.31) of the spectral function.

$$\gamma_{0}\rho\left(\tilde{q},\tilde{u}\right)\gamma_{0}=\pi_{s}-i\pi_{5}\gamma_{5}+\pi_{q}\tilde{q}^{\mu}\tilde{\gamma}_{\mu}+\pi_{u}\tilde{u}^{\mu}\tilde{\gamma}_{\mu}-\pi_{5_{q}}\tilde{q}^{\mu}\tilde{\gamma}_{\mu}\gamma_{5}$$

$$-\pi_{5_{u}}\tilde{u}^{\mu}\tilde{\gamma}_{\mu}\gamma_{5}+\pi_{T}\left(\tilde{q}^{\mu}\tilde{u}^{\nu}-\tilde{u}^{\mu}\tilde{q}^{\nu}\right)\tilde{\sigma}_{\mu\nu}+\pi_{T}^{\prime}\epsilon^{\mu\nu\kappa\lambda}\tilde{q}_{\kappa}\tilde{u}_{\lambda}\tilde{\sigma}_{\mu\nu}\tag{B.40}$$

We need the following relations which can easily be shown to hold:

$$\tilde{k}^{\mu}\tilde{\gamma}_{\mu}=k^{\mu}\gamma_{\mu},\quad\tilde{k}^{\mu}\tilde{p}^{\nu}\tilde{\sigma}_{\mu\nu}=k^{\mu}p^{\nu}\sigma_{\mu\nu},\quad\gamma_{5}\sigma^{\mu\nu}=\frac{i}{2}\epsilon^{\mu\nu\kappa\lambda}\sigma_{\kappa\lambda},$$

$$\epsilon^{\mu\nu\kappa\lambda}\tilde{k}_{\mu}\tilde{p}_{\nu}\tilde{\sigma}_{\kappa\lambda}=-\epsilon^{\mu\nu\kappa\lambda}k_{\mu}p_{\nu}\sigma_{\mu\nu}.\tag{B.41}$$

Using eq. (B.41) in eq. (B.40) we obtain,

$$\gamma_{0}\rho\left(\tilde{q},\tilde{u}\right)\gamma_{0}=\pi_{s}-i\pi_{5}\gamma_{5}+\pi_{q}q^{\mu}\gamma_{\mu}+\pi_{u}u^{\mu}\gamma_{\mu}-\pi_{5_{q}}q^{\mu}\gamma_{\mu}\gamma_{5}$$

$$-\pi_{5_{u}}u^{\mu}\gamma_{\mu}\gamma_{5}+\pi_{T}\left(q^{\mu}u^{\nu}-u^{\mu}q^{\nu}\right)\sigma_{\mu\nu}+\pi_{T}^{\prime}\epsilon^{\mu\nu\kappa\lambda}q_{\mu}u_{\nu}\sigma_{\kappa\lambda}.\tag{B.42}$$

Comparing this result with eq. (B.31) we infer:

$$\pi_{5}=\pi_{5_{q}}=\pi_{5_{u}}=\pi_{T}^{\prime}=0.\tag{B.43}$$

B.4 Time Reversal

Under the time reversal operation, the fermion fields transform as

$$\mathcal{T}\eta(x)\mathcal{T}^{-1} = T\eta(-x_0,\boldsymbol{x}), \qquad \mathcal{T}\bar{\eta}(x)\mathcal{T}^{-1} = \eta^\dagger(-x_0,\boldsymbol{x})T^\dagger\gamma_0^*. \tag{B.44}$$

In eq. (B.44), T is a unitary matrix that acts on spinor indices and satisfies

$$T^\dagger\gamma_\mu^* T = \gamma_\mu^\dagger. \tag{B.45}$$

We can write

$$\langle\psi_0(u)|\eta(x)\bar{\eta}(0)|\psi_0(u)\rangle = \left\langle\mathcal{T}\psi_0(u)\left|\mathcal{T}[\eta(x)\bar{\eta}(0)]^\dagger\mathcal{T}^{-1}\right|\mathcal{T}\psi_0(u)\right\rangle$$

$$= \left\langle\mathcal{T}\psi_0(u)\left|\left\{\mathcal{T}[\eta(x)\bar{\eta}(0)]^\dagger\mathcal{T}^{-1}\right\}^\dagger\right|\mathcal{T}\psi_0(u)\right\rangle^*. \tag{B.46}$$

Using eq. (B.44) and eq. (B.45) it is straightforward to show that

$$\mathcal{T}[\eta(x)\bar{\eta}(0)]^\dagger\mathcal{T}^{-1} = T\eta(-x_0,\boldsymbol{x})\eta^\dagger(0)T^\dagger\gamma_0^*. \tag{B.47}$$

Substituting eq. (B.47) in eq. (B.46) one obtains

$$\langle\psi_0(u)|\eta(x)\bar{\eta}(0)|\psi_0(u)\rangle = \left\langle\mathcal{T}\psi_0(u)\left|T\eta(-x_0,\boldsymbol{x})\eta^\dagger(0)T^\dagger\gamma_0^*\right|\mathcal{T}\psi_0(u)\right\rangle^*, \tag{B.48}$$

and the spectral function becomes

$$\rho(q,u) = \int d^4x e^{iq\cdot x}\left\langle\mathcal{T}\psi_0(u)\left|T\eta(-x_0,\boldsymbol{x})\eta^\dagger(0)T^{-1}\gamma_0^*\right|\mathcal{T}\psi_0(u)\right\rangle^*. \tag{B.49}$$

Making the change of the variable $(x_0,-\boldsymbol{x})\to x$ and letting the operator $\mathcal{T}$ act on the bra and the ket, eq. (B.49) becomes

$$\rho(q,u) = \left\{T\int d^4x e^{i\tilde{q}\cdot x}\langle\psi_0(\tilde{u})|\eta(x)\bar{\eta}(0)|\psi_0(\tilde{u})\rangle T^\dagger\right\}^*. \tag{B.50}$$

Hence we have

$$\rho(q,u) = \left\{T\rho(\tilde{q},\tilde{u})T^\dagger\right\}^*. \tag{B.51}$$

We can now use eq. (B.51) to learn more about the coefficient functions in our expansion of the spectral function, with the relations

$$T\gamma_\mu T^\dagger = \gamma_\mu^T, \quad T\sigma_{\mu\nu}T^\dagger = -\sigma_{\mu\nu}^T, \quad T\gamma_5 T^\dagger = \gamma_5^T. \tag{B.52}$$

One obtains

$$\rho(q,u) = \pi_s - i\pi_5\gamma_5 + \pi_5\tilde{q}^\mu\tilde{\gamma}_\mu + \pi_u\tilde{u}^\mu\tilde{\gamma}_\mu + \pi_{5_q}\tilde{q}^\mu\tilde{\gamma}_\mu\gamma_5 + \pi_{5_u}\tilde{u}^\mu\tilde{\gamma}_\mu\gamma_5$$

$$-\pi_T\left(\tilde{q}^\mu\tilde{u}^\nu - \tilde{u}^\mu\tilde{q}^\nu\right)\tilde{\sigma}_{\mu\nu} - \pi_T'\epsilon^{\mu\nu\kappa\lambda}\tilde{q}_\kappa\tilde{u}_\lambda\tilde{\sigma}_{\mu\nu}. \tag{B.53}$$

In eq. (B.53) we have

$$\tilde{q}^\mu\tilde{\gamma}_\mu = q^\mu\gamma_\mu, \quad \tilde{q}^\mu\tilde{u}^\nu\tilde{\sigma}_{\mu\nu} = q^\mu u^\nu\sigma_{\mu\nu}, \quad \epsilon^{\mu\nu\kappa\lambda}\tilde{q}_\kappa\tilde{u}_\lambda\tilde{\sigma}_{\mu\nu} = -\epsilon^{\mu\nu\kappa\lambda}q_\kappa u_\lambda\sigma_{\mu\nu}, \tag{B.54}$$

and we end up with the following expression

$$\rho(q,u) = \pi_s - i\pi_5\gamma_5 + \pi_5 q^\mu\gamma_\mu + \pi_u u^\mu\gamma_\mu + \pi_{5_q}q^\mu\gamma_\mu\gamma_5 + \pi_{5_u}u^\mu\gamma_\mu\gamma_5$$

$$-\pi_T\left(q^\mu u^\nu - u^\mu q^\nu\right)\sigma_{\mu\nu} + \pi_T'\epsilon^{\mu\nu\kappa\lambda}q_\kappa u_\lambda\sigma_{\mu\nu}. \tag{B.55}$$

Comparing with eq. (B.31) we see that the coefficient functions π_5 and π_T vanish. Together with eq. (B.43) our expansion for the spectral function reduces to

$$\rho(q,u) = \pi_s(q,u) + \pi^\mu(q,u)\gamma_\mu. \tag{B.56}$$

This is the most general form possible for the spectral function for the normal propagation and states that its expansion can contain at most one Lorentz index. This result equivalently applies to the form factors of the normal quark propagator which can be written in terms of the spectral function. Therefore only scalar- and vector-type form factors are possible

$$S(p) = S_b(p) + ip^k S_a(p)\gamma_k + ip_4 S_c(p)\gamma_4. \tag{B.57}$$

In the presence of chemical potential, μ, eq. (B.57) generalizes to

$$S(p) = S_b(p) + ip^k S_a(p)\gamma_k + i(p_4 - i\mu)S_c(p)\gamma_4. \tag{B.58}$$

B.5 The Anomalous Propagator

We tried to apply the analytic argument for the normal propagator to the anomalous propagator. If achieved, this would have enabled us to check our numerical results for the anomalous propagation but our attempts have failed.

We began with the spectral function for the anomalous propagation which is similar to eq. (B.2):

$$\rho_{\alpha\beta}(q,u) = \int d^4x e^{iq\cdot x}\left\langle\psi_0(u)\left|K\bar{\eta}_\alpha^T(x)\,\bar{\eta}_\beta(0)\right|\psi_0(u)\right\rangle, \tag{B.59}$$

where

$$K = C\gamma_5\tau_2. \tag{B.60}$$

In eq. (B.60) C is the charge conjugation operator and τ_2 is the Pauli matrix that acts in the colour space.

We then expanded the form factors in terms of coefficient functions similar to eq. (B.5). However we could not make any conclusion about the realness of these coefficient functions as in Sec. B.1 due not being able to derive a relation like eq. (B.7). This prevented us from proceeding our investigation following the same steps as in [48].

We tried to find alternative ways to proceed, one of which was to split the fermion fields into real and imaginary parts and investigate them separately. However we soon realized that this is a very strong assumption which does not fit our aim.

Another idea was to investigate the symmetry properties without having the information that the coefficient functions are real. But this attempt failed because we were not able to derive relations similar to eq.s (B.22), (B.39) and (B.51).

We finally tried to assume a particular representation for the Dirac gamma matrices and the corresponding representations of the various operators we deal with but –apart from losing the generality of the argument– these attempts failed because of the presence of the operator K and the transpose of the conjugate fermion field in eq. (B.59), which prevented us from making manipulations similar to the ones for the normal propagation.

Bibliography

[1] Johannes Blumlein. The Theory of Deeply Inelastic Scattering. *Prog. Part. Nucl. Phys.*, 69:28–84, 2013.

[2] J.I. Skullerud. Gluons, quarks and deconfinement at high density. *Proceedings of Science*, 2009.

[3] Andreas Schmitt. Dense matter in compact stars: A pedagogical introduction. *Lect. Notes Phys.*, 811:1–111, 2010.

[4] J. Wambach D. Nickel and R. Alkofer. Color-superconductivity in the strong-coupling regime of Landau gauge QCD. *Phys. Rev.*, D73, 2006.

[5] Itzhak Tserruya. The Strongly Interacting Quark Gluon Plasma at RHIC and LHC. *EPJ Web Conf.*, 70:00022, 2014.

[6] Victor Braguta, Ernst-Michael Ilgenfritz, Andrey Yuryevich Kotov, Alexander Molochkov, and Alexander Nikolaev. Study of the phase diagram of dense QC_2D with $N_f = 2$ within lattice simulation. *PoS*, LATTICE2016:042, 2016.

[7] Christof Gattringer and Christian B. Lang. Quantum chromodynamics on the lattice. *Lect. Notes Phys.*, 788:1–343, 2010.

[8] Alexei Bazavov. Lattice QCD at Non-Zero Temperature. *PoS*, LATTICE2014:392, 2015.

[9] A. Nakamura. Behavior of quarks and gluons at finite temperature and density in SU(2) QCD. *Phys. Lett.*, B149:391, 1984.

[10] Ouraman Hajizadeh, Tamer Boz, Axel Maas, and Jon-Ivar Skullerud. Gluon and ghost correlation functions of 2-color QCD at finite density. *EPJ Web Conf.*, 175:07012, 2018.

[11] Tamer Boz, Seamus Cotter, Leonard Fister, Dhagash Mehta, and Jon-Ivar Skullerud. Phase transitions and gluodynamics in 2-colour matter at high density. *Eur. Phys. J.*, A49:87, 2013.

[12] Simon Hands, Seamus Cotter, Pietro Giudice, and Jon-Ivar Skullerud. The Phase Diagram of Two Color QCD. 2012. [J. Phys. Conf. Ser.432,012020(2013)].

[13] Seamus Cotter, Pietro Giudice, Simon Hands, and Jon-Ivar Skullerud. Towards the phase diagram of dense two-color matter. *Phys. Rev.*, D87(3):034507, 2013.

[14] Simon Hands, Seyong Kim, and Jon-Ivar Skullerud. Non-relativistic spectrum of two-color QCD at non-zero baryon density. *Phys. Lett.*, B711:199–204, 2012.

[15] Simon Hands, Philip Kenny, Seyong Kim, and Jon-Ivar Skullerud. Lattice Study of Dense Matter with Two Colors and Four Flavors. *Eur. Phys. J.*, A47:60, 2011.

[16] Simon Hands, Seyong Kim, and Jon-Ivar Skullerud. A Quarkyonic Phase in Dense Two Color Matter? *Phys. Rev.*, D81:091502, 2010.

[17] Simon Hands, Peter Sitch, and Jon-Ivar Skullerud. Hadron Spectrum in a Two-Colour Baryon-Rich Medium. *Phys. Lett.*, B662:405–412, 2008.

[18] Simon Hands, Seyong Kim, and Jon-Ivar Skullerud. Quark matter in QC(2)D. *Eur. Phys. J.*, A31:787–789, 2007.

[19] Simon Hands, Seyong Kim, and Jon-Ivar Skullerud. Deconfinement in dense 2-color QCD. *Eur. Phys. J.*, C48:193, 2006.

[20] Simon Hands, John B. Kogut, Maria-Paola Lombardo, and Susan E. Morrison. Symmetries and spectrum of SU(2) lattice gauge theory at finite chemical potential. *Nucl. Phys.*, B558:327–346, 1999.

[21] Howard D. Trottier. String breaking by dynamical fermions in three-dimensional lattice QCD. *Phys. Rev.*, D60:034506, 1999.

[22] Shailesh Chandrasekharan and Fu-Jiun Jiang. Chiral limit of 2-color QCD at strong couplings. *PoS*, LAT2005:198, 2006.

[23] Shailesh Chandrasekharan and Fu-Jiun Jiang. Phase-diagram of two-color lattice QCD in the chiral limit. *Phys. Rev.*, D74:014506, 2006.

[24] E. M. Ilgenfritz, M. Kalinowski, M. Muller-Preussker, B. Petersson, and A. Schreiber. Two-color QCD with staggered fermions at finite temperature under the influence of a magnetic field. *Phys. Rev.*, D85:114504, 2012.

[25] V. V. Braguta, V. A. Goy, E. M. Ilgenfritz, A. Yu. Kotov, A. V. Molochkov, M. Muller-Preussker, and B. Petersson. Two-Color QCD with Non-zero Chiral Chemical Potential. *JHEP*, 06:094, 2015.

[26] V. V. Braguta, E. M. Ilgenfritz, A. Yu. Kotov, A. V. Molochkov, and A. A. Nikolaev. Study of the phase diagram of dense two-color QCD within lattice simulation. *Phys. Rev.*, D94(11):114510, 2016.

[27] Lukas Holicki, Jonas Wilhelm, Dominik Smith, Bjorn Wellegehausen, and Lorenz von Smekal. Two-colour QCD at finite density with two flavours of staggered quarks. *PoS*, LATTICE2016:052, 2017.

[28] Simon Hands, Istvan Montvay, Luigi Scorzato, and Jonivar Skullerud. Diquark condensation in dense SU(2) matter. *Nucl. Phys. Proc. Suppl.*, 106:450–452, 2002.

[29] Simon Hands, Istvan Montvay, Luigi Scorzato, and Jonivar Skullerud. Diquark condensation in dense adjoint matter. *Eur. Phys. J.*, C22:451–461, 2001.

[30] Simon Hands, Istvan Montvay, Manfred Oevers, Luigi Scorzato, and Jonivar Skullerud. Numerical study of dense adjoint 2 color matter. *Nucl. Phys. Proc. Suppl.*, 94:461–468, 2001. [,461(2000)].

[31] Simon Hands, Istvan Montvay, Susan Morrison, Manfred Oevers, Luigi Scorzato, and Jonivar Skullerud. Numerical study of dense adjoint matter in two color QCD. *Eur. Phys. J.*, C17:285–302, 2000.

[32] Jacobus J. M. Verbaarschot. The Spectrum of the QCD Dirac operator and chiral random matrix theory: The Threefold way. *Phys. Rev. Lett.*, 72:2531–2533, 1994.

[33] J. B. Kogut, Misha A. Stephanov, D. Toublan, J. J. M. Verbaarschot, and A. Zhitnitsky. QCD - like theories at finite baryon density. *Nucl. Phys.*, B582:477–513, 2000.

[34] Jens O. Andersen, Tomas Brauner, and William Naylor. Confronting effective models for deconfinement in dense quark matter with lattice data. *Phys. Rev.*, D92(11):114504, 2015.

[35] Deog Ki Hong, V. A. Miransky, I. A. Shovkovy, and L. C. R. Wijewardhana. Schwinger-Dyson approach to color superconductivity in dense QCD. *Phys. Rev.*, D61:056001, 2000. [Erratum: Phys. Rev.D62,059903(2000)].

[36] Craig D. Roberts and Sebastian M. Schmidt. Dyson-Schwinger equations: Density, temperature and continuum strong QCD. *Prog. Part. Nucl. Phys.*, 45:S1–S103, 2000.

[37] Nils Strodthoff and Lorenz von Smekal. Polyakov-Quark-Meson-Diquark Model for two-color QCD. *Phys. Lett.*, B731:350–357, 2014.

[38] Larry McLerran and Robert D. Pisarski. Phases of cold, dense quarks at large N(c). *Nucl. Phys.*, A796:83–100, 2007.

[39] D. T. Son and Misha A. Stephanov. QCD at finite isospin density. *Phys. Rev. Lett.*, 86:592–595, 2001.

[40] J. B. Kogut and D. K. Sinclair. Lattice QCD at finite isospin density at zero and finite temperature. *Phys. Rev.*, D66:034505, 2002.

[41] J. B. Kogut and D. K. Sinclair. The Finite temperature transition for 2-flavor lattice QCD at finite isospin density. *Phys. Rev.*, D70:094501, 2004.

[42] Keitaro Nagata and Atsushi Nakamura. QCD Phase Diagram with Imaginary Chemical Potential. *EPJ Web Conf.*, 20:03006, 2012.

[43] Anyi Li, Andrei Alexandru, and Keh-Fei Liu. Reweighting method in finite density lattice QCD. *PoS*, LAT2006:030, 2006.

[44] Kurt Langfeld. Density-of-states. *PoS*, LATTICE2016:010, 2017.

[45] Erhard Seiler. Status of Complex Langevin. *EPJ Web Conf.*, 175:01019, 2018.

[46] S. Duane, A. D. Kennedy, B. J. Pendleton, and D. Roweth. Hybrid Monte Carlo. *Phys. Lett.*, B195:216–222, 1987.

[47] An informal but useful and interactive web page to learn about HMC by Alex Rogozhnikov. `http://arogozhnikov.github.io/2016/12/19/markov_chain_monte_carlo.html`.

[48] J. J. Rusnak and R. J. Furnstahl. Two point fermion correlation functions at finite density. *Z. Phys.*, A352:345–350, 1995.

[49] Tamer Boz, Pietro Giudice, Simon Hands, Jon-Ivar Skullerud, and Anthony G. Williams. Two-color QCD at high density. *AIP Conf. Proc.*, 1701:060019, 2016.

[50] Gerard 't Hooft. On the Phase Transition Towards Permanent Quark Confinement. *Nucl. Phys.*, B138:1–25, 1978.

[51] Derek B. Leinweber, Jon Ivar Skullerud, Anthony G. Williams, and Claudio Parrinello. Gluon propagator in the infrared region. *Phys. Rev.*, D58:031501, 1998.

[52] Christian S. Fischer, Axel Maas, and Jens A. Muller. Chiral and deconfinement transition from correlation functions: SU(2) vs. SU(3). *Eur. Phys. J.*, C68:165–181, 2010.

[53] Leonard Fister and Jan M. Pawlowski. Confinement from Correlation Functions. *Phys. Rev.*, D88:045010, 2013.